AMIL2DA

Advanced MIPAS level 2 data analysis [amil'tu:da]

Contract No. EVG1-CT-1999-00015
An EC research project co-funded by the Energy, Environment and Sustainable Development Program within the topic 'Development of Generic Earth Observation Technologies'

Midterm Report

July 1, 2000 - Feb 28, 2002

co-ordinated by Thomas von Clarmann

DLR

CLRC

UNIVERSITÄT BREMEN

http://www.fzk.de/imk/imk2/ame/amil2da

Advanced MIPAS Level 2 Data Analysis (AMIL2DA)

Midterm Report

March 2002

Project EVG1-CT-1999-00015

Study Team: T.v. Clarmann (IMK)(coordinator)
H. Bovensmann (UB)
S. Ceccherini (IROE)
A. Doicu (DLR)
A. Dudhia (OU)
H. Fischer(IMK)
J.-M. Flaud (LPM)
B. Funke (IAA)
M. García-Comas(IAA)
S. Hilgers (DLR)
M. Höpfner (IMK)
V. Jay (OU/RAL)
S. Kellmann (IMK)
B.J. Kerridge (RAL)
E. Kyrölä(FMI)
A. Linden (IMK)
M. López-Puertas (IAA)
M.Á. López-Valverde (IAA)
F.J. Martín-Torres (IMK)
J. Reburn (RAL)
M. Ridolfi (UBOL)
C.D. Rodgers (OU)
F. Schreier (DLR)
G. Schwarz (DLR)
T. Steck (IMK)
G.P. Stiller (IMK)
J. Tamminen(FMI)

Chapter 1

Detailed Report

1.1 Background

Global change with its two inter-linked major subproblems ozone destruction and global warming is a substantial threat to life on Earth. Any political actions against global change require detail information on the driving mechanisms. Quantitative knowledge of atmospheric compostion plays a key role in this context. The Michelson Interferometer for Passive Atmospheric Sounding (MIPAS) has been designed to measure the Earth's atmospheric composition with respect to a large number of trace species. MIPAS is part of the core payload of ESA's Environmental Satellite (Envisat) which was launched sucessfully into its sun-synchronous polar orbit on 1 March.

The MIPAS instrument on ESA's Envisat provides information on atmospheric species relevant to ozone chemistry and global change. Species to be measured by MIPAS are the nitrogen family (N_2O, HNO_3, NO, NO_2, $ClONO_2$, N_2O_5 and others), chlorine reservoirs ($ClONO_2$, $HOCl$), chlorine source species (CFC-11, CFC-12, CFC-22, CCl_4; possibly also CFC-113, HCFC-123, HCFC-141b, and HCFC-142b), chlorine radicals (ClO), dynamic tracers (H_2O, N_2O, CH_4, CF_4, SF_6) and many more, e.g., CO, OCS, NH_3, HCN, C_2H_2, or C_2H_6. While only six species (H_2O, O_3, HNO_3, CH_4, N_2O, NO_2, along with temperature and pressure) are analyzed under ESA responsibility in an operational mode, analysis of many more scientifically interesting species is left to research groups. In order to fill this gap in the list of data products, and to ensure quality and intercomparability of these independently generated value-added data products, innovative data analysis and retrieval approaches were developed by participating groups. New spectroscopic data as well as a set of vibrational temperatures were provided. Radiative transfer codes were sucessfully cross-checked. Furthermore, retrieval codes were cross-checked by means of blind test retrievals based on synthetic data. Further steps will be intercomparison of results for a common set of real MIPAS-measurements, analysis of best-fit residuals and their potential explanation by breakdown of thermodynamic equilibrium, inaccurate spectroscopic data, instrumental artefacts or inadequate radiative transfer modelling, a plausibility check of results by comparison to a chemistry transport model, and comparison against measurements from external sources.

1.2 Scientific/technological and socio-economic objectives

1.2.1 Scientific/technological objectives

The first major goal is to have data analysis tools available which are suited for a profound scientific exploitation of MIPAS spectra. Different innovative level-2 algorithms, strategies and processors of participating groups must be adapted for at least semi-operational analysis of MIPAS data. In particular those algorithms which are appropriate for retrieval of data products beyond the official ESA key-species H_2O, O_3, HNO_3, N_2O, CH_4, and NO_2 are emphasized in order to allow better exploitation of MIPAS data. Also limitations in the ESA data product originating from their operational requirements, such as limited resolution, precision, accuracy, and altitude coverage are reduced by dedicated retrieval procedures developed within this project. This assessment of retrieval strategies creates a solid basis for scientific work in the research areas of ozone depletion, global change and change of atmospheric composition, including related detail problems. Since several groups participating in this proposal have developed their strategies based on their own experience and with certain scientific goals in mind, the diversity of approaches shall be maintained in order to increase flexibility of the European scientific community to respond to various scientific problems. Requirements to algorithms and retrieval strategies developed and assessed in this project are:

- Extension of the list of data products, in particular with respect to species relevant to global change and stratospheric ozone depletion. Besides analysis of O_3, H_2O, HNO_3, N_2O, CH_4, and NO_2, retrieval of vertical profiles of NO, NO_2, $ClONO_2$, N_2O_5, HOCl, CFC-11, CFC-12, CFC-22, CCl_4, CFC-113, HCFC-123, HCFC-141b, HCFC-142b, ClO (if enhanced), CF_4, CO, SF_6, OCS, NH_3, HCN, C_2H_2, and C_2H_6 shall be attempted to be made possible.

- Improvement of data quality, with respect to precision, accuracy, and vertical resolution. The latter is in particular important for assessment of stratospheric-tropospheric exchange processes.

- Extension of altitude coverage of data products in the troposphere and upper atmosphere. While the first is of major importance for assessment of stratospheric-tropospheric exchange processes, the latter is useful for better understanding of radiative processes. This issue also includes dedicated processing of MIPAS spectra recorded at non-standard observation scenarios, e.g., finer tangent-altitude spacing, wider altitude-coverage of the tangent altitudes, or side-viewing observations.

The second major goal is to gain confidence in the strategies and involved computer codes and to give proof to the international scientific community of the reliability and appropriateness of the approaches as well as the quality of data products. This includes:

- Cross-validation of radiative transfer models used by the different groups, detection of deficiencies in the codes by means of cross-comparison, and upgrading in order to remove the discrepancies.

- Cross-comparison of employed retrieval strategies and algorithms, and upgrading by removal of detected deficiencies.

- Standardization of results in terms of data quality and characterization with respect to vertical resolution and retrieval error estimates.

- Understanding of differences in results achieved by the various involved strategies applied to real measurement data, and detection, understanding, and tentative removal of systematic residuals in the best-fit spectra. This objective includes also the understanding of unexpected MIPAS instrument behaviour (possible unpredicted instrumental errors) and understanding of unexpected signals in the atmospheric spectra (e.g., due to non-local thermodynamic equilibrium (NLTE)emissions or missing or erroneous spectroscopic reference data)

- Final data product validation by cross-comparison to external measurement data (GOMOS, SCIAMACHY, and others).

The improved understanding of radiative transfer modelling and retrieval approaches will be shared with the scientific community by publication of the results in reports and tentatively in easily accessible scientific journals. New spectroscopic data and vibrational temperature data will be forwarded to interested and qualified users on request. Characterization and validation of data products will be extensively reported and made public for the scientific community by appropriate media to be agreed by the consortium. Candidate media are, among others, printed reports and internet web pages.

1.2.2 Socio-Economic Objectives

In an indirect and logterm manner, nevertheless with this purpose clearly in view, AMIL2DA aims at preventing life on Earth of the threat of global change. Along with this longterm goal, there are several economic objectives:

In a short term, through private-public sector partnerships, the study contributes to maintain a sound economic structure in the countries involved, since involved research institutions are typical employers of small companies in the branches software development and computer technology.

In an intermediate term, after successful scientific exploitation of MIPAS data, industry involved in the development of European spaceflight, Envisat, and MIPAS will gain reputation and can refer to their involvement in the MIPAS project in order to promote themselves and to prove competence. This will strengthen their position in the worldwide market.

In a slightly longer term, successful earth observation science from space will politically justify also further development in space technology. This will lead to further purchase and development orders space industry depends on. In turn, if, due to unsuccessful or unjustifiable space experiments the development of European Earth observation technologies should be stopped, a lot of skill and know-how already developed in industry could no longer be exploited.

In a long term, global change research helps to better understand atmospheric processes. In future, this knowledge may help to avoid or at least better predict and thus manage possible environmental disasters which possibly are linked to global change. Avalanche and flood disasters in the Alpine region in spring 1999 demonstrate in a very impressive manner that such disasters have a dramatic economic impact in regions involved.

1.3 Applied methodology, scientific achievements and main deliverables

1.3.1 Processor Set Up (WP 2000)

Introduction

The first step of AMIL2DA was to put the participants in a position such that they can analyze MIPAS satellite data. This includes upgrading existing radiative transfer models and retrieval processors such that they can be applied to MIPAS data, tuning of processing parameters, provision of data interfaces.

The basic functionality of a retrieval code is as follows: For initial guess atmospheric state parameters, measurements are simulated by means of a radiative transfer forward model for the given measurement geometry. The difference between simulated and real measurements is minimized in a least squares sense by adjusting the atmospheric state parameters. This step, which often involves constraints, is performed by an inversion algorithm, which besides the differences between measured and simulated radiances also needs the sensitivities of the signal with respect to the atmospheric state parameters. The set of atmospheric state parameters, which minimizes the difference between real and simulated measurements, plus a contribution of the constraining term, if applicable, is the solution of the so-called inverse problem. Since radiative transfer is non-linear, the inversion is put into a framework of Newtonean iteration. The whole procedure of determination of state parameters from radiance measurements is called "retrieval".

The radiative transfer forward model performs the forward solution of the radiative transfer equation, which can be written for a single wavenumber gridpoint as:

$$L_\nu = L_{0,\nu}\tau_\nu(l_{obs},0) + \int_{l=0}^{l_{obs}} J_\nu(T(l))\frac{\partial\tau_\nu(l_{obs},l)}{\partial l}dl \tag{1.1}$$

where L_ν is spectral radiance at wavenumber ν at the location of the observer l_{obs}, L_0 is background radiance (assumed zero in this intercomparison experiment), l is the path coordinate, $\tau_\nu(l_1,l_2)$ is the spectral transmittance between two locations l_1 and l_2, and J is the source function, which under conditions of local thermodynamic equilibrium (LTE) depends on kinetic temperature T and frequency, while in non–LTE it depends on state distributions of all involved emitters. The spectral transmittance $\tau_\nu(l,l-dl)$ along a path element dl is calculated according to Beer's law as

$$\tau_\nu(l,l-dl) = \exp(-\sigma(l,l-dl)) = \exp(-\sum_g \kappa_{g,\nu}(l)\rho_g(l)dl) \tag{1.2}$$

where $\sigma(l,l-dl)$ is optical depth of path element dl, $\kappa_{g,\nu}$ is the absorption cross section of species g at the spectral position ν, which is composed of the contribution of each transition and ρ_g is the number density of species g.

The path l along which Eq. (1.1) is integrated is determined by the observer position, the viewing angle, and atmospheric refraction. Equation (1.1) is either integrated directly by application of a quadrature scheme, or it is solved following the Curtis–Godson [1, 2, 3, 4] approach, where layer–related slant path column amounts $u_{g,l}$

$$u_{g,l} = \int_l \rho_g(l)dl \tag{1.3}$$

and mass–weighted layer mean values p_{CG} and T_{CG} of pressure and temperature

$$p_{CG,g} = \frac{\int_l \rho_g(l)p(l)dl}{u_{g,l}} \tag{1.4}$$

and

$$T_{CG,g} = \frac{\int_l \rho_g(l)T(l)dl}{u_{g,l}} \tag{1.5}$$

are used. Each layer l is characterized by its slant path column amounts $u_{g,l}$ and representative state parameters $p_{CG,g}$ and $T_{CG,g}$ which are assumed to be constant within the layers. The intention of this approach is to save computation time because the numerically fine integration needs not be performed for each internal frequency grid point but only for $u_{g,l}$, $p_{CG,g}$ and $T_{CG,g}$. The numerical radiative transfer integration then can be done with sufficient accuracy on a quite coarse spatial grid.

Resulting spectrally high–resolved radiances (so–called "monochromatic" spectra) then are convolved with the instrument line shape (ILS). The radiance field is convolved with the instrument field of view (FOV). Both these steps are necessary to make simulated spectra comparable to real measurements recorded by a non–ideal spectrometer of finite spectral resolution and non–infinitesimal field of view. In theory, the non–infinitesimal inhomogeneously illuminated field of view of an interferometer leads to a dependence of the ILS from the actual radiance field, which implies that ILS and FOV should be treated in one single step. For practical applications, however, ILS and FOV convolution are often regarded as independent from each other and thus are performed sequentially in an arbitrary order, depending on the architecture of the particular radiative transfer code.

The inversion code controls the solution of the following iterative retrieval equation:

$$x_{i+1} = x_i + (K^T S_y^{-1} K + R)^{-1} (K^T S_y^{-1} (y_{measurement} - y(x_i) - R(x_i - x_0))) \tag{1.6}$$

where x_i is the vector of atmospheric state parameters as resulting from ith iteration; x_0 is the vector of atmospheric state parameters as known a priori; $y_{measurement}$ is the vector of real measurements, while $y(x_i)$ is the vector of measurements simulated by solution of the radiative transfer forward model using x_i as input. K is the Jacobian matrix, containing the partial derivatives $\frac{\partial y}{\partial x}$; superscript T denotes transposed matrices, S_y is the covariance matrix of the measurement, and R a user-defined regularization operator.

Five institutions contribute to AMIL2DA with their MIPAS level 2 data analysis processors. These are IMK, Oxford University, DLR, IROE, and RAL. DLR and IROE operate two processors each. Descriptions of each processor w.r.t. detail implementation choices of the forward model and inversion control code follow below. A more technical description is found in a dedicated report [5]. Furthermore, complementary spectroscopic data have been generated. Also these have been reported in detail in a dedicated paper [6].

The IMK Processor (WP 2100)

The IMK Radiative Transfer Code KOPRA: The Karlsruhe Optimized and Precise Radiative Transfer Model (KOPRA) is a line–by–line, layer–by–layer model for forward calculation of infrared atmospheric transmittance and radiance spectra for various geometries [7]. Three–dimensional ray tracing for a non–spherical Earth is supported by means of the tangential displacement method [8]. Horizontal inhomogeneities of atmospheric state parameters are linearly approximated by their horizontal gradients. The full three–dimensional treatment of the atmosphere is supported. The hydrostatical constraint can optionally be applied to the input atmospheric data.

The line–by–line calculation of absorption cross sections relies on an optimized implementation [9] of the Humlicek Voigt line algorithm [10]. Whenever justified with respect to the user–defined accuracy parameter, pure Doppler or Lorentzian lines are used in order to minimize computational effort. The correction of the theoretical line shapes by so–called chi–factors is supported for CO_2. For this species, line–coupling effects can be considered [11] either by the Rosenkranz approximation [12] or by direct diagonalization, not only for Q-branches but also for P and R branches. Line–coupling effects of other species will be included in a future version. Tabulated pressure and temperature dependent absorption cross sections of molecules for which no line data are available are interpolated to actual values and frequencies. As an alternative, so–called pseudolines of these species can be handled in a quasi line–by–line mode, as proposed by G. Toon (private communication). Continua of H_2O, CO_2, N_2, and O_2 are included [13, 14]. Furthermore aerosol continuum emission and extinction can be calculated on the basis of empirical extinction coefficients or on the basis of absorption and extinction cross section as well as phase function spectra generated by a Mie model which is nested with the radiative transfer model. The most recent version also supports a single scattering source function to model the scattering of radiation into the line of sight [15]. KOPRA uses an optimized irregular altitude dependent frequency grid for calculation of absorption cross sections and integration of the radiative transfer equation [16]. Spectroscopic transitions which do not contribute substantially to the overall signal are rejected automatically, where the threshold is driven by a user–defined accuracy parameter. Non–local thermodynamic equilibrium (non–LTE) is taken into account.

The integration of the radiative transfer equation follows a Curtis–Godson approach [1, 2, 3, 4]. Since Curtis–Godson mean values are species dependent, while the value of the Planck function is temperature- and wavenumber- but not species–dependent, there are several options to calculate the temperature relevant for the source function. Either Curtis–Godson mean values for air, for a certain target species, an average over the Curtis–Godson mean values of all species, weighted by their individual absorption cross sections can be used. For calculation of the source function in non–LTE applications the latter approach is mandatory.

KOPRA has both internal ILS models and an interface to read pretabulated ILS functions for convolution of the monochromatic spectra and resampling on a user–specified output grid. Furthermore the numerical radiance integration of the vertical field over an altitude dependent sensitivity function (field of view function) is supported in the observation angle space rather than tangent altitude space. Here and at other instances KOPRA provides some optimization for calculation of limb sequences of spectra in a sense that intermediate results which are needed for calculation of spectra of different elevation angles are calculated only once.

The IMK Retrieval Control Program: The IMK retrieval program is based on a nonlinear thus iterative least squares fit scheme with optional Levenberg Marquardt [17, 18] damping with dynamic adjustment of the damping control parameter [19]. In a nearly linear vincinity of the solution the calculation of an updated Jacobian per iteration is switched off in order to save calculation time.

The retrieval program supports any user-defined regularization operator and offers Tikhonov identity, Tikhonov 1st and 2nd order smoothing, as well as the inverse a priori covariance matrix (optimal estimation) as default settings. Also unregularized inversion is supported. In case of joint fit of multiple parameters, different altitude grids can be defined by the user for different parameters. Multiple microwindow applications are supported, both in an onion peeling [20, 21, 22] and a global fit [23] sense.

Retrieval of the following parameters is supported: VMR of species, temperature, tangent altitude, pressure, empirical continuum signal, offset calibration, horizontal gradients of atmospheric state parameters, aerosol parameters, ILS parameters, non-LTE parameters, gain calibration, and frequency shift.

The Oxford University Processor (WP 2200)

The Reference Forward Model (RFM): The Reference Forward Model (RFM) is a line–by–line radiative transfer model originally developed from GENLN2 [24] to provide reference spectral calculations for MIPAS. It has subsequently been developed into a general purpose radiative transfer model supporting a wide variety of applications.

The representation of the atmosphere is user–defined but can also be set for automatic sub–layering, where the maximum width of each layer is determined by a limit on the variation in pressure–broadened line width or temperature variation. A 2-dimensional option is also available, representing the atmosphere by a series of profiles in the vertical viewing plane with the horizontal coordinate defined by the angle subtended at the Earth centre.

Ray paths through the atmosphere can be defined in terms of elevation angle, geometric or refracted tangent altitudes. The ray tracing uses different algorithms according to whether a 1 or 2 dimensional atmosphere is used. For one dimension, the FASCODE [25] algorithm is used with altitude as the integrated coordinate and a transformation to avoid the singularity near the tangent point. For two dimensions, a fourth–order Runge–Kutta scheme is used to integrate altitude, zenith angle and Earth–centre angle. In both cases, absorber and Curtis–Godson pressures and temperatures are integrated along the ray path. Refraction is calculated using a version of Edlen's formula.

Spectral calculations can be performed using HITRAN [26] line data, HITRAN cross section data (tabulated for arbitrary pressure and temperature coordinates), or look–up tables compressed by singular value decomposition (SVD) [27] employed for the MIPAS operational processing. For line data, the calculation uses a two–pass system with an initial coarse grid (0.5 cm^{-1}) calculation for the interpolation of line wings up to 25 cm^{-1} from line centre, followed by a fine mesh (typically 0.0005 cm^{-1}) for modelling lines within 1 – 2 cm^{-1} from line centre. Total internal partition sums and molecular cross section data are those associated with the HITRAN-96 release, although modified for HNO_3. Line shapes are calculated using a modified version of the Humlicek algorithm [28]. For cross section data a triangulation is used to directly interpolate the associated pressure temperature grid, thus avoiding any intermediate interpolation to resample the pressure and temperature coordinates into a uniform spacing. Both line-coupling and non-LTE are supported by the RFM.

The radiative transfer can either be performed on the fine grid (0.0005 cm^{-1}) or on a user–specified irregular grid. The Curtis–Godson temperature (weighted for each absorber by its absorption) defines the Planck function within each layer but there is also an option to describe the Planck function in terms of a variation with optical depth ("linear–in–tau"), which better represents emission from layers of high opacity.

FOV and ILS convolutions are performed internally using externally supplied functions. The FOV convolution is performed in tangent–pointing space, and the ILS convolution in spectral space.

The Oxford University Retrieval Program: The Oxford University retrieval OPTIMO (oxford processor to invert MIPAS observations) uses an iterative fit with a-priori constraints (optimal estimation) to invert MIPAS spectra. Profiles of constituent VMRs, temperature, pressure, pointing can be retrieved on a user-specified retrieval grid with microwindow dependent continuum and offset. Joint retrievals of multiple parameters can also be performed.

The retrieval uses microwindows selected for MIPAS, and can use masks which exclude parts of the spectrum in order to improve retrieval errors. Other features include:

- Gauss-Newton iterations, or Levenberg-Marquardt damping
- Sequential inclusion of microwindows, or measurements to update estimate of retrieved parameters
- Option to use look-up tables and/or irregular spectral grids for faster forward model calculations
- Kalman filter to incorporate measurements along the viewing track by updating the local estimate of the profile. This also allows horizontal gradients to be calculated and incorporated into the forward model. This can either be applied within one limb-scan sequence or extended across multiple sequences.

Additional tools for use in the processing are the automatic selection of measurements to be included in the retrieval, selection of initial guess profiles for target parameters and contaminants, plus software to visualise retrieval results and diagnostics.

The DLR-a Processor (WP 2300a)

Modular Infrared Atmospheric Radiative Transfer (MIRART): The Modular Infrared Atmospheric Radiative Transfer (MIRART) [29] software has been designed for a variety of applications, arbitrary observation geometries, instrumental fields–of–view (FOV) and line shapes (ILS). Emphasis has been put on efficient and reliable numerical algorithms and a modular approach appropriate for forward simulations and retrieval applications [30].

For the calculation of the Voigt function, MIRART uses an optimized combination of the Humlicek [10] and Hui–Armstrong–Wray [31] complex error function algorithm [32] and switches to pure Lorentzian line shape in the far wings; a further optimization similar in spirit to the work of Kuntz [9] exploits the equidistant wavenumber grid. The wavenumber grid is choosen individually for each altitude level and molecule. Furthermore a coarse grid is used for contributions of lines outside the spectral region of interest, whereas contributions near the line center are calculated on a fine spectral grid. Further line shapes supported are Lorentz or Van Vleck–Huber convolved with Doppler.

Line parameters from the HITRAN [26], HiTemp [33], SAO [34], GEISA [35] or JPL [36] spectroscopic data bases can be used in MIRART. The line strength conversion from the reference temperature used in the database to the atmospheric temperature follows the scheme used in the ATMOS software [37].

In addition to the line contributions, continua are implemented for water (Clough–Kneizys–Davis (CKD) continuum Version 2.2), carbon dioxide, oxygen, and nitrogen [13, 14]. Alternatively the Liebe dry air [38] continuum or an empirical continuum for the far infrared provided by K. Chance [priv. comm. 1996] can be used.

The solution of Schwarzschild's equation and Beer's law requires the integration of spatially varying quantities, which are given only for a set of discrete altitude points, along the line of sight. These integrals are — in contrast to the Curtis–Godson approach — calculated using standard numerical quadrature schemes. MIRART has implemented a trapezoid quadrature scheme, the method of overlapping parabolas, and a piecewise cubic Hermite quadrature [39]. These quadrature rules work for arbitrarily spaced (i.e. not necessarily equidistant) abscissas.

MIRART offers the choice of field–of–view convolution either in the tangent altitude space or in the elevation angle space using Gaussian quadrature rules appropriate for the chosen sensitivity function.

DLR-a Retrieval Code: The DLR retrieval code has been developed to solve inverse problems in atmospheric spectroscopy for a variety of applications, nb. slant up– or downlooking and limb–viewing geometries of Fourier transform, Fabry–Perot, or heterodyne sensors. The retrieval is based on (generally nonlinear) least squares fit techniques minimizing the residual vector of observed spectra and spectra calculated with an estimated atmospheric state vector. In case of limb sounding observations a global fit strategy, i.e., simultaneous fit of the entire limb sequence, is employed. For the solution of the inverse problem stochastic (i.e., optimal estimation) and semi–stochastic methods are used. The semi–stochastic methods implemented are:

- iteratively regularized Gauss–Newton method (with and without bound constraints on the variables) [40],
- Levenberg–Marquardt method for ill-posed problems [41],
- nonlinear Tikhonov regularization [42].

Two crucial points for successful regularization are the choice of the regularization matrix L and the selection of the regularization parameter λ. L is either of a Sobolev type, i.e. a combination of identity, first, and second order derivative, a diagonal weighting matrix or an approximation to the a priori covariance matrix. In the case of iteratively regularized Gauss–Newton the sequence of regularization parameters is choosen using the L–curve criterion for each linear sub–problem or the noise–level criterion, while in case of Tikhonov regularization λ is choosen using the nonlinear L–curve criterion, generalized cross validation, or the discrepancy principle.

The DLR-b Processor (WP 2300b)

DLR-b Forward Modeling: The DLR-b processor uses the KOPRA radiative transfer forward algorithm which already has been described above and thus needs no detail specification here. Some minor discrepancies between the KOPRA versions installed at IMK and at DLR could occur due to asynchronous installations of new versions and extensions being used for specific investigations at IMK (e.g. non-LTE research activities being conducted at Karlsruhe). However, these differences should not affect the basic tests performed for AMIL2DA.

The identity of the forward model was also the reason why the results of the DLR-2 processor did not appear explicitly in previous AMIL2DA forward model comparisons. The comparisons have, of course, been performed by DLR in order to verify the correct installation and parameter handling of the KOPRA forward model after its integration with the retrieval code at DLR. These verification activities allowed us to detect some small typographical problems in the exercise definitions at a rather early stage of the comparison activities. Then, the results obtained during the forward model comparisons were uploaded to the IMK server at Karlsruhe. Checks of the results showed no deviations from the data generated at IMK.

DLR-b Retrieval Code: The retrieval software available at DLR comprises various alternative strategies for the global fit retrieval of trace gas profiles. The retrieval is performed on a selectable grid (e.g. sampling grid, regular fine grid, or user selectable grid) with a flexible choice of the retrieval vector and regularisation options (e.g. joint or sequential trace gas retrieval, support of horizontal gradients, retrieval of continuum and offsets). The retrieval starts with a joint determination of corrected tangent heights, temperature, and pressure, followed by retrievals of trace gases using one of the least squares methods:

- pure least squares
- Levenberg-Marquardt
- optimal estimation
- Tikhonov regularisation
- Levenberg-Marquardt combined with optimal estimation

The matrix inversion algorithm needed for the numerical calculation of profiles is selectable, too:

- singular value decomposition (general or truncated)
- QR decomposition
- Cholesky decomposition
- conjugated gradients

The profile data needed as initial guess profiles, a priori profiles, or interfering species is taken from an internal data base.

The final selection of the most appropriate parameter selection will be made after the end of the Envisat commissioning phase.

The OFM/ORM (WP2400a)

The Optimized Forward Model (OFM): The Optimized Forward Model has been developed for application in the operational near–real–time processing of MIPAS spectra [43]. This implies that major effort has been spent for minimization of computational effort. In particular the sequence of operations has been organized so that unnecessary repeated calculations are avoided and the available random access memory of the computer is fully exploited.

In a first step, the line of sight is determined. The line of sight depends on the viewing direction of the instrument and, due to refraction, is not a straight line, but bends towards the Earth. Since the Earth is assumed locally spherical, the local radius of curvature being determined by the simplified WGS84 model [44] which has been adopted for the Earth shape, the atmospheric layering is spherical too. The atmosphere is considered homogeneous in the horizontal direction, therefore each layer has constant physical properties. The radiative transfer integral, that is a path integral, is computed as a summation of the contributions of a set of discrete layers. A common set of layers is defined for all the observation geometries of the limb sounding sequence. The boundaries of these layers are defined using an automated algorithm that checks the variation across the layer of both temperature and the Voigt half-width of a reference line against pre-defined thresholds. For each layer resulting from this process, Curtis–Godson pressure and temperature are determined. In principle, Curtis–Godson pressures and temperatures have to be computed for each gas, each layer and each limb view of the scan. In practice, only a sub–set of paths (combination of layer and limb view) requires a customized calculation, because, except for the tangent path, the secant law approximation can be applied and consequently the corresponding Curtis–Godson quantities are independent of the limb view angle. Therefore Curtis–Godson quantities are computed for the paths relating to the lowest geometry and only the tangent layers of the other limb views. This is a very effective optimization because it strongly reduces the number of paths for which cross sections have to be computed.

The absorption cross sections can either be calculated line by line (LBL), using a pre–selected spectroscopic database and fast Voigt profile computation [10], or be read from pre–computed look–up tables (LUTs). The use of LUTs is advantageous only if they can be stored in random access memory, and the feasibility of this depends on the amount of memory required. In order to reduce this amount of memory the LUTs are compressed [27] using the ‘Singular Value Decomposition’. The number of singular values, as well as the number of pressure and temperature increments, are optimized so that the maximum difference between the resulting LUT and LBL convolved limb radiances is about a factor ten below the MIPAS measurement noise. In the LBL calculation of the cross sections, line–mixing, pressure–shift, self–broadening, and non–local thermodynamic equilibrium (NLTE) are neglected. In the calculation of the cross–section LUTs only line–mixing and NLTE are neglected.

Finally, the radiadive transfer integral is computed (exploiting the symmetry of the line–of–sight about the tangent point) for an optimized and pre–computed set of frequencies. In order to resolve the sharp features at high altitude, a ’fine grid’ of spectral resolution of the order of 0.0005 cm^{-1} is required. The full radiative transfer calculation is however performed for a subset of fine grid points, the remaining spectrum being recovered by linear interpolation. This subset is denoted ’irregular grid’ and depends on the boundaries of the chosen spectral interval (microwindow), and on the instrument line shape. An optimized irregular grid is determined which is valid for all tangent altitudes, and therefore common to all observation geometries. Typically only 5 – 10 percent of the complete fine grid is sufficient for a satisfactory reconstruction of the spectral distribution. The computation of the radiative transfer and the convolution of the high–resolution spectrum with the apodized instrument line–shape are done in a single optimized step to save computing time. The apodized instrument line shape (AILS) is determined offline from the ILS function, which accounts for misalignment and aperture effects, and the ’Norton–Beer strong’ apodization function [45]. The convolved spectrum is represented on a relatively coarse grid defined via an input parameter.

Using the above procedure, AILS convolved spectra are simulated for a set of tangent altitudes that includes the tangent altitudes of the measured spectra and some additional altitudes necessary for an accurate FOV convolution. The spread of the FOV in the altitude domain is tabulated in a FOV pattern distribution FOV(z) whose shape is constructed with a linear interpolation from a tabulated function. The FOV pattern is assumed to be constant with the scan angle. The effect of field of view is then taken into account by performing, for each spectral frequency, the convolution between the tangent altitude dependent spectrum and the FOV pattern. The variability of the spectrum as a function of tangent altitude is determined by interpolating a polynomial through the spectra simulated at contiguous tangent altitudes in the range of the FOV pattern. The altitude grid at which the spectra are simulated is rather fine, especially in the altitude regions (e.g. below tropopause) where the radiance profile is expected to change rapidly with tangent altitude.

The Optimized Retrieval Model: The IROE Retrieval Model (named Optimized Retrieval Model, ORM) uses the nonlinear least-square fit, performed with the Gauss-Newton method modified according to the Levenberg-Marquardt criterion [18, 46] and the global fit approach [23], i.e. the whole altitude profile is retrieved from simultaneous analysis of all the limb-views of a scan. The profile is retrieved at a number of discrete altitudes smaller than or equal to the number of the observed limb-views. At intermediate altitudes the forward model uses an interpolated value of the profiles. The retrieval of the atmospheric profiles is performed as follows: first pressures at tangent altitudes and temperature profile are retrieved simultaneously, then minor constituents VMR profiles are retrieved individually in sequence. The retrieval model is based on the "microwindow" approach: this means that data analysis is carried-out by considering only narrow (less than 3 cm^{-1} width) spectral subintervals, called "microwindows", containing major information on the retrieved parameters. An important part of the retrieval code is the fast determination of the derivatives of the radiance with respect to the retrieval parameters (Jacobian matrix). The derivatives of the spectrum with respect to volume mixing ratio, atmospheric continuum and tangent pressures are computed analytically (in the sense that the analytical formulas of the derivatives are implemented in the program), while the temperature derivatives are determined in a 'fast numerical' way, i.e. instead of rerunning the forward model as many times as many are the temperature parameters, the derivatives are computed in parallel with the spectra, so that unnecessary repeated calculations are avoided and the limited influence of the change of one temperature parameter on the overall temperature profile is exploited. In the ORM the overall computing effort required for the Jacobian calculation is equal to the effort needed for the calculation of the spectra. The convergence criteria adopted in the IROE code are a compromise between the required accuracy of the parameters and the computing speed of the algorithm. The following three convergence conditions are used to achieve this:

1. condition on linearity: at the current iteration the relative difference between the actual chi-square and the expected value of chi-square computed in the linear approximation must be less than a fixed threshold;

2. condition on attained accuracy: the relative correction that has to be applied to the parameters for the subsequent iteration is below a fixed threshold. Different thresholds are used for the different types of parameters depending on their required accuracy. Furthermore, whenever an absolute accuracy requirement is present for a parameter, the absolute variation of the parameter is checked instead of the relative variation. The non-target parameters of the retrieval, such as continuum and instrumental offset parameters are not included in this check.

3. Condition on computing time: the maximum number of iterations must be less than a given

threshold. The convergence is reached if either condition 1 or condition 2 is satisfied. If only the condition on computing time is satisfied, the retrieval is considered unsuccessful.

The IROE-1 Processor (WP2400b)

The Extended IROE Forward Model (IROE1): The extended IROE forward model (IROE1) processor is based on the OFM but includes the following extensions:

- Line–mixing of CO_2 Q-branches [47]
- pressure–shift,
- self–broadening
- improved H_2O continuum model (CKD 2.4 vs. CKD 2.1 implemented in the IROE2 model)

Local thermodynamic equilibrium is still assumed because its implementation in the IROE code would have required a full re-design of the code itself.

The Extended IROE Retrieval Model (IROE1): Even if in general the accuracy of the forward model turns-out to be improved when considering pressure–shift, self–broadening and line–mixing, it should be noted that pressure–shift and self–broadening have very little impact on MIPAS spectra simulated under realistic atmospheric conditions (self broadening might be important only at very low altitudes for water lines) and line–mixing, as simulated in the IROE1 forward model [47], impacts only localized spectral regions (Q-branches of CO_2). This conclusion is also confirmed by the encouraging results obtained from blind test retrievals (see Sect. 1.3.2). For this reason it was decided not to upgrade the forward model internal to the retrieval scheme and to avoid the neglected effects by adopting an appropriate selection of spectral intervals (microwindows) for the retrieval. The microwindows are selected using an optimization scheme developed at Oxford University and described in Dudhia (1999) [48]. This approach allows also for an accurate estimation of the various error components affecting the retrieved profiles. This is also the approach used in ESA's near real-time Level 2 processor.

If on one hand the joint exploitation of the optimized microwindow selection scheme and the IROE2 retrieval algorithm is expected to provide sufficient accuracy with respect to the neglected spectroscopic effects, on the other hand there is a general concern regarding some instrument–related quantities derived in Level 1b processing and assumed as known in the Level 2 chain. In particular the following quantities determined in the Level 1b processor

- ILS shape
- frequency calibration
- intensity calibration
- instrumental offset

could be affected by a significant error with consequent impact on Level 2 retrieval performance. For this reason we decided to upgrade the IROE2 retrieval scheme in order to allow for a quantification and possibly for a correction of the errors associated with the above quantities. The "improved" version of the IROE2 retrieval scheme is named IROE1 and, compared to IROE2, has the additional flexibility that the user can define via input files the retrieval vector. In addition to the usual state parameters retrieved by the IROE2 code, with the IROE1 code it is also possible to (optionally) retrieve from measured spectra the following parameters:

- ILS broadening parameter (one parameter / spectral band)
- frequency scaling parameter (one parameter / spectral band)

- intensity scaling parameter (one parameter / spectral band)
- MW- and altitude- dependent instrumental offset (IROE2 is able to fit only a MW- dependent instrumental offset).

Of course the IROE1 code can also be operated with the same state vector defined in the IROE2 code and in this case it produces exactly the same results of the IROE2 code.

The RAL Processor (WP 2500)

The Two–Dimensional Forward Model (FM2D): The RAL forward model, FM2D, is a line-by-line code that allows modelling of the atmosphere in two dimensions with the field expressed as a two-dimensional, vertical and horizontal section. Operation in a one-dimensional mode, where the atmosphere is assumed to be spherically symmetric and so may be represented by a single vertical profile, is also possible. Originally designed for microwave wavelengths [49], it has been extended in scope, particularly by inclusion of appropriate continuum formulations, such as that by Clough et al. [13], to allow mid-infrared radiative transfer calculations to be carried out. The model allows application of an instrument function, in terms of basic parameters such as spectral response and field of view, and performs direct, analytic calculation of "weighting functions" (rows of the Jacobian matrix of the forward model radiances with respect to retrieval parameters) for atmospheric parameters.

FM2D has two main parts, an initialisation module and a radiative transfer module. The former deals with the all input parameters including atmospheric model definition, line-shape and spectral grid selection, and instrument characteristics, such as spectral response and field of view. To carry the radiative transfer quadrature, a set of computational grid points in the horizontal and vertical are defined. The module calculates the weights for the interpolation from the points at which atmospheric fields are specified to the computational grid, and also determines the basis functions for the derivatives of the field on the computational grid with respect to perturbation at the points at which input data is specified. This approach allows rapid repeated determination of line-of-sight integrals and weighting functions.

The radiative transfer module calculates radiances and their derivatives with respect to the atmospheric state for the required number of pencil-beam views. The ray-tracing scheme includes refraction which may be modelled in a rigorous two dimensional manner or, alternatively, by assuming horizontal symmetry about the geometric tangent point, which makes the calculation much more rapid and is adequate for many scenarios. The calculation of absorption coefficients follows from evaluation of spectral line and continua contributions; the Voigt line shape calculation used is the Wells [28] version of the modified Humlicek algorithm. To restrict computational memory requirements, monochromatic spectra are convolved with spectrometer response functions for each view, and only the convolved radiances and weighting functions are stored. Once these spectrometer-convolved values have been computed for all pencil-beams, they are convolved with the instrument field of view function before being output.

RAL Retrieval: The RAL retrieval program is a modular code which has an interface to the FM2D forward model thus allowing for two-dimensional fields. It is a least squares algorithm based on the "optimal estimation" philosophy allowing a priori, as well as measurement information, as input. It is designed for retrieval of atmospheric and instrument parameters and exists in two main implementations as a linear and a non-linear scheme.

The linear scheme, based on a linearisation of the forward model, generates information used to characterise retrieval behaviour. It allows calculation of a number of diagnostics, such as retrieval error covariance and averaging kernel matrices, which can be used to address issues such as attainable horizontal resolution, spatial sampling and associated memory requirements and relative benefits of various scan sequences. Such information is used to optimise retrieval product selection and grids for particular measurements, and to determine error characteristics for the instrument.

The non-linear scheme is designed for the retrieval of products from real or synthetic measurements. It is a non-linear, iterative retrieval scheme capable of retrieving horizontal and vertical structure from measurements. It uses a Levenberg-Marquardt type algorithm with a sophisticated updating method to allow rapid and efficient convergence.

Matrix algebra routines to efficiently handle band diagonal and patially block-diagonal matrices have been implemented within the retrieval schemes to cope with the large matrix dimensions associated with 2-D retrieval problems.

Complementary Spectroscopic Data (WP 2600)

In this Section we present the spectroscopic data which are made available. The spectral interval spanned by the data is adapted to the spectral domain covered by the MIPAS experiment, namely 600-2500 cm^{-1} The data have been made accessible in a dedicated report [6].

Ozone $^{16}O_3$: The ozone molecule $^{16}O_3$ has been recently the subject of extensive laboratory studies [50, 51, 52, 53] in the 10μm region in order to improve the line positions and intensities in this spectral domain which is extensively used for atmospheric retrievals and in particular by MIPAS. We have compared the four sets of experimental data and the following conclusions have been reached:

- The four sets of data are highly consistent on a relative basis (agreement better than 2%)
- The three sets of data from ref. [50, 51, 52] agree very well as far as absolute intensities are concerned (dispersion of $\approx$ 0.8 %, 1σ standard deviation of $\approx$ 1.7 %) whereas the intensities from Ref. [53] are consistently $\approx$ 4 % higher.

As a consequence it was decided to rely on the sets of data from ref. [50, 51, 52] and these intensities were fitted to derive the relevant transition moment constants. Using these constants a new line list was generated for the two bands absorbing at 10μm, namely ν_1 and ν_3. When comparing to HITRAN96 one gets for the following deviations: For the ν_1 band HITRAN values are 4.4% higher than the new calculations, and for the ν_3 band, HITRAN values are 3.5% higher.

Precisely the newly calculated data concern the cold bands ν_1 and ν_3 as well as the ν_2 band which was also measured in ref. [52]. It is worth noticing that, if one wants to use these new data, the intensities of all the other bands (hot bands, isotopic species) have to be divided by 1.04 in order to account for the change in the absolute intensities of the cold bands and hence be consistent.

Hypochlorous acid HOCl: Recent studies [54, 55] of the spectroscopic properties of this molecule have shown that the HITRAN96 spectral parameters concerning the ^{35}Cl and ^{37}Cl isotopic variants of this species were not of sufficient quality both for the line positions and intensities. As far as the atmospheric databases are concerned, the main problem was related to the line intensities in the 8.1μm spectral region. Indeed, this molecule is unstable and always exists in the equilibrium.

$$H_2O + Cl_2O \leftrightarrows HOCl$$

The main difficulty is then to estimate its partial pressure in the cell. Different methods can be used (see ref. [55] for their description) but when one looks at the literature it appears that there is a huge scatter among the various results concerning the total band intensities (Table 8 of ref. [55]). To avoid this difficulty, the method used in ref. [55] was to measure simultaneously the far infrared and the 8.1μm line intensities. Since the intensities can be precisely calculated in the far infrared using the dipole moment derived from stark experiments, one can use them to estimate accurately the partial pressure of HOCl and hence to get reliable intensities at 8.1μm. These new intensities are on the average 66% lower than the HITRAN96 ones.

Nitrogen dioxide NO_2: The 6μm region is widely used to retrieve atmospheric NO_2 profiles from balloon borne or satellite instruments since it corresponds by far to the strongest absorption of this molecule: ν_3 band. On the other band, as far as spectroscopy is concerned, due to the spin-rotation interaction the infrared vibration-rotation lines appear as doublets. This spin-rotation interaction can be treated through a perturbation method or directly, the latter method giving much more accurate results.
In HITRAN96 only two bands appear in the 6.2μm region:

- The fundamental ν_3 band for which the spin-rotation interaction was taken fully into account [56].
- The first hot band $\nu_2 + \nu_3 - \nu_2$ for which this interaction was treated through a perturbation method [57], hence providing one with results of a quality not sufficient for experiments like MIPAS.

It is worth noticing that no other hot bands are available in this spectral region in the HITRAN database preventing one to deal with possible NLTE phenomena. Based on recent spectroscopic studies, new spectral parameters have been generated. They are:

- The band system[58] $\{011, 030\} \longleftarrow (010)$ which replaces the first hot band $\nu_2 + \nu_3 - \nu_2$
- The band system [59] $\{120, 101\} \longleftarrow \{100, 020, 001\}$, the strongest band of which is $\nu_1 + \nu_3 - \nu_1$ (HIT13-4)
- The band system [60] $\{040, 021, 002\} \longleftarrow \{100, 020, 001\}$ the strongest bands of which are $2\nu_3 - \nu_3$ and $2\nu_2 + \nu_3 - 2\nu_2$
- The band system [61] $\{022, 003\} \longleftarrow \{040, 021, 002\}$ the strongest bands of which are $3\nu_3 - 2\nu_3$ and $2\nu_2 + 2\nu_3 - (2\nu_2 + \nu_3)$

1.3.2 Forward Model Intercomparison (WP 3000)

The role of the radiative transfer forward modeling in the data processing chain of remotely sensed data is crucial. In order to prove the reliability of the participants' forward models and to detect potential forward model deficiencies, a cross comparison exercise was carried out to mutually validate radiative transfer codes. The idea of the setup of the intercomparison exercise was to start from simple settings proving the basic functionalities of the radiative transfer codes, and then to proceed to more complex and realistic scenarios.

Test Scenario (WP 3100)

In order to avoid any masking of differences in the basic functionalities of the codes by additional sophistication introduced by realistic atmospheric simulations, the first set of tests refer to cell transmittance calculations (see Table 1).
In a second step, atmospheric limb emission spectra have been intercompared (see Table 2). The profiles of atmospheric state parameters were available via the AMIL2DA web–site. Unless explicitly mentioned, the HITRAN98 spectroscopic database, an update of Ref. [26], was used. For CFC-12, cross section data measured by P. Varanasi (Ref. [62] and subsequent updates) were used. Furthermore, vibrational temperatures [63], pretabulated MIPAS-FOV and AILS were provided to the participants. In the following we report a summary of the finings of the forward model intercomparison experiment, while the complete results are published in a dedicated report [64]:

Table 1: Cell Transmittance Test Cases

Test Id. /	Spectral Region cm^{-1}	Cell Length m	Species	VMR ppmv	p hPa	T K	Con-tinua	Chi Factor	Line Mixing	ILS
1	1270.0–1280.0	5.0	N_2O[1]	100	1013.25	296	/	/	/	/
2	1274.2–1275.0	5.0	N_2O[1]	100	20.0	296	/	/	/	/
3	1274.2–1275.0	20.	N_2O[1]	100	2.0	296	/	/	/	/
4	1274.2–1275.0	20.	N_2O[1]	100	2.0	296	/	/	/	yes[2]
5	1274.2–1275.0	20.	N_2O[1]	100	2.0	296	/	/	/	yes[3]
6	1274.2–1275.0	20.	N_2O[1]	100	2.0	296	/	/	/	yes[4]
7	1270.0–1280.0	5.	N_2O[1]	100	1013.25	250	/	/	/	/
8	1274.2–1275.0	5.	N_2O[1]	100	20.0	250	/	/	/	/
9	1274.2–1275.0	20.	N_2O[1]	100	2.0	250	/	/	/	/
10	1830.0–1840.0	50.0	NO N_2O O_3	$5. \times 10^2$ $5. \times 10^5$ $1. \times 10^5$	20.0	250	/	/	/	/
11	2390.0–2500.0	10^6	CO_2	355	250	296	/	yes	/	/
12	2390.0–2500.0	10^6	CO_2	355	250	250	/	yes	/	/
13	715.0–725.0	50.0	CO_2	355	250	250	/	yes[5]	yes	/
14	715.0–725.0	50.0	CO_2	355	50	250	/	yes[5]	yes	/
15	738.0–744.0	500.0	CO_2	355	250	250	/	yes[5]	yes	/
16	738.0–744.0	1000.0	CO_2	355	50	250	/	yes[5]	yes	/
17	1600.0–1610.0	100.0	H_2O	1000	250	250	yes	/	/	/

[1] only one transition at 1274.6166 cm^{-1} to be considered.
[2] unapodized instrument line shape
[3] apodized instrument line shape
[4] apodized simplified (pretabulated) instrument line shape
[5] chi–factor may not be active in this microwindow under consideration of line mixing.

Table 2: Atmospheric Radiance Test Cases

Test Id.	Spectral Region cm^{-1}	tangent altitude km	Species Considered	FOV	ILS	Continua	Line Mixing	non LTE
18[1]	1215.0–1217.0	15	H_2O, CO_2, O_3 N_2O, CH_4	/	/	yes	/	/
19	1215.0–1217.0	15	H_2O, CO_2, O_3 N_2O, CH_4	/	/	yes	/	/
20	1215.0–1217.0	40	H_2O, CO_2, O_3 N_2O, CH_4	yes	yes	yes	/	/
21	1215.0–1217.0	15	H_2O, CO_2, O_3 N_2O, CH_4	yes	yes	yes	/	/
22	790.0–794.0	15	CO_2, O_3	/	/	/	yes	/
23	790.0–794.0	15	CO_2, O_3	yes	yes	/	yes	/
24	920.0–940.0	15	CO_2, O_3, CFC-12	/	/	/	yes	/
25	920.0–940.0	15	CO_2, O_3, CFC-12	yes	yes	/	yes	/
26	1600.0–1610.0	10	H_2O, N_2O, CH_4 O_2, NO_2	yes	yes	yes	/	/
27	675.5–676.5	100	CO_2, O_3	yes	yes	yes	/	/
28	675.5–676.5	100	CO_2, O_3	yes	yes	yes	/	yes
29	967.0–968.0	100	CO_2, O_3	yes	yes	yes	/	/
30	967.0–968.0	100	CO_2, O_3	yes	yes	yes	/	yes

[1] standardized altitude grid of 1 km used for integration of radiative transfer equation.

Vibrational Temperatures (WP 3200)

Introduction: This report describes the calculation of the vibrational temperatures climatology that has been developed within this project. This is an extension to the previously report on the vibrational temperatures supplied earlier in this project. Thus, it is heavily based on that report and on the models described in López-Puertas and Taylor (2001) [65]. We therefore describe here only the major updates and the major differences with respect to those formerly calculated within the ESA study *'Study on the Simulation of Atmospheric Infrared Spectra'* reported by Clarmann et al. (1998) [66] and those reported earlier in the project. A more detailed description can be found in those reports and the references cited below.

The vibrational temperatures have been calculated for the 5 reference atmospheres compiled in different studies of ESA by John Remedios and co-workers [67] (see Table 3). These reference atmospheres comprise profiles for the kinetic temperature, pressure and many species abundances, and cover typical and extreme atmospheric conditions for which the potential non-LTE effects vary from weakest to moderate to strongest. The reference atmospheres for the calculation of the non-LTE populations have been set up from 0 to 120 km using a grid of 1 km, except for NO, which are extended up to 200 km.

Table 3: Reference Atmospheres

Ref. Atm.	Season/Latitude	Solar Illumination
1	Mid-latitude	Day, SZA=60°
2	Mid-latitude	Night
3	Polar Winter	Night
4	Polar Summer	Day, SZA=60°
5	Equator	Day, SZA=60°

Some changes have been introduced in these reference atmospheres in order to correctly compute the non-LTE populations. They fall generally within three categories: a) to include correctly the chemical or photochemical constraints for certain species; b) the extension in altitude for some species; and c) the extension of the reference atmospheres to electronically and vibrationally excited species needed for the non-LTE calculations. A summary of the changes introduced are described below.
We have included consistent profiles for:

- NO, NO_2, O and O_3 due to the reactions $NO_2+O \rightarrow NO+O_2$ (important excitation mechanism for NO(v)), and $NO+O_3 \rightarrow NO_2+O_2$ (important excitation mechanism of NO_2(v)).
- O, O_2 and O_3 due to $O+O_2+M \rightarrow O_3$ (important excitation mechanism for O_3(v)).
- H and O_3 due to $H+O_3 \rightarrow OH+O_2$ (important excitation mechanism for OH(v)).
- For N_2, O_2, O, Ar, H_2O in order to satisfy that the sum of all vmr is equal to 1.

Since O, H and OH are not included in the MIPAS reference atmosphere, there were no problems to adapt profiles from the Garcia and Solomon model [69] for these gases. In order to NOT change any MIPAS target species abundances we kept NO_2 and O_3 and changed only N_2, O_2 and NO for night-time conditions as follows:

(i) Including consistent O and O_2 from Garcia and Solomon [69] to get the right $O+O_2+M\rightarrow O_3(v)$ production.

(ii) Introduce a considerably reduced NO in the nighttime stratosphere (but not in troposphere).

Table 4: Summary of the changes introduced in the ESA reference atmospheres.

Gas	Hitran ID	Data source	Lower limit (km)	Upper limit (km)	vmr at 200 km (ppmv)
Pressure		MIPAS	0	120	
		hydrostatic	120	200	
T_k		MIPAS	0	120	
		MSIS	130	200	
H_2O	1	MIPAS	0	120	1.0×10^{-4}
CO_2	2	MIPAS	0	120	2.0
O_3	3	MIPAS	0	120	1.0×10^{-6}
N_2O	4	MIPAS	0	120	1.0×10^{-6}
CO	5	MIPAS	0	120	1.0
CH_4	6	MIPAS	0	120	1.0×10^{-5}
NO_2	10	MIPAS	0	120	5.0×10^{-10}
HNO_3	12	MIPAS	0	120	1.0×10^{-17}
NO	8	MIPAS	0	120	
		Gérard and Roble (1988) [68] For polar night, the MIPAS midlat night profile has been used below 70 km	135	200	
O_2	7	MIPAS	0	90	
		MSIS	130	200	
O	34	Garcia and Solomon [69]	0	90	
		MSIS	130	200	
N	152*	MSIS	70	200	
H	154*	Garcia and Solomon [69] $[H] = [H]_{GS}*[O_3]_{GS}/[O_3]_{MIPAS}$ in order to get consistent OH production in the mesosphere	0	110	1.0×10^{-2}
OH	13	Garcia and Solomon [69]	0	112	1.0×10^{-12}
N_2	22	$vmr(N_2) = 1 - vmr(Ar) -$ vmr(all gases above)			

*Not in HITRAN. KOPRA internal reference.

(iii) We made $N_2 = 1 -$ sum of all other vmrs.

(iv) We made $[H] = [H]_{GS}*[O_3]_{GS}/[O_3]_{MIPAS}$.

Table 4 describes the reference atmospheres used in the generation of the vibrational temperatures and Table 5 the data sources. The profiles have been spline interpolated within gaps.

This climatology of vibrational temperatures includes calculations for the 5 reference atmospheres and conditions described above for the following species and vibrational levels:

1. CO_2: 56 vibrational levels, emitting at 15, 10, and 4.3 μm and the $N_2(1)$ level.
2. CO: the CO(1–0) transition near 4.6 μm.
3. O_3: 249 levels, emitting around 14.6, 10 and 4.8 μm.
4. H_2O: 6 levels, emitting around 6.3 and 4.7 μm+ $O_2(1)$.

Table 5: Data source for the reference atmospheres.

	Data source	Reference
MIPAS:	ESA reference atmospheres `day,ngt,win,sum,equ`	Remedios (2001) [67]
MSIS:	day 35°N, 12.00 local time, April 30th, F10.7=200, AP=10	Hedin (1991) [70]
	ngt 35°N, 0.00 local time, April 30th, F10.7=200, AP=10	
	sum 85°N,12.00 local time, June 30th, F10.7=200, AP=10	
	win 85°N,12.00h local time, Dec 30th, F10.7=200, AP=10	
	equ same as day	
Gérard and Roble chemical transport model		Gérard and Roble (1988) [68]
Garcia and Solomon chemical transport model run for 2006		Garcia et al. (1992) [71]
		Garcia and Solomon (1994) [69]

5. CH_4: 12 levels, emitting around 7.6 and 6.5 μm.

6. NO: 6 levels emitting near 5.3 μm.

7. N_2O: 41 levels originating the 8.6, 7.8, 4.5, 4.0, 3.6, and 3.0 μm bands.

8. NO_2: 7 (0,0,v_3) levels, originating the ν_3 fundamental and hot bands in the 6.2–7.0 μm interval.

9. HNO_3: 8 levels, originating the 5.9, 7.5, 11, and 22 μm bands.

10. OH: 9 vibrational levels.

The vibrational temperatures are given at 1 km grid from 0 to 120 km, except nitric oxide (NO) which is given up to 200 km. The vibrational temperatures have been written in the KOPRA format and are available at `http://www.iaa.es/~puertas/amil2da/vt.html`. The files are named as `vt_mm_aaa.kop`, where `mm` is the molecule (`CO2, CO, `), and `aaa` the reference atmosphere (`day, ngt, win, sum, equ`).

General Improvements: The vibrational temperatures of some species have been computed with completely new and improved models. This is the case for O_3, NO, and N_2O. OH has been added to the new set, which was not present in the previous dataset. For CO_2 and H_2O the number of vibrational levels has been extended.
The new vibrational temperatures have also some improvements which are common to most species. These include:

1. Those due to an improved reference atmosphere data set:
   (a) The new reference atmospheres are hydrostatically consistent.
   (b) The species abundances are now physically and chemically consistent. E.g.,
   – consistent O_3 and O for the calculation of the vibrational temperatures of O_3 and H_2O
   – consistent NO and NO_2 for the calculation of the vibrational temperatures of NO and NO_2
   – consistent NO and O_3 for the calculation of the vibrational temperatures of NO_2 and
   – consistent O_3 and H for OH vibrational temperatures.

2. Some vibrational temperatures depend on the volume mixing ratio (vmr) of the species considered, e.g., O_3, NO_2, NO and OH. This implies that, for estimating non-LTE effects correctly, the same abundances used in the calculation of their vibrational temperatures should be used in the forward model when computing the atmospheric radiance. This might lead to incorrect retrieved quantities for some species if the vibrational temperatures are not re-calculated within the retrieval scheme.

3. The correction of the small artificial non-LTE deviations in the stratosphere (more important for CO_2) that were present in the previous set due to an inappropriate interpolation in the non-LTE models.

4. A better estimation of the upwelling tropospheric flux, calculated now using the line-by-line KOPRA code, has been introduced for all levels of all species.

CO_2: The model used for these calculations has been updated from previous calculations including the findings of the analysis of ISAMS data [72, 73]. This includes a more accurate calculation of the populations of the v_3 levels of the 636 CO_2 isotope emitting in the 4.6 μm region. Also, a new CO_2 vmr profile in the upper mesosphere has been used. This is significantly smaller than previously thought in this atmospheric region [74].
The new vibrational temperatures also incorporate significant improvements arisen from a very detailed comparison with the model developed at AFRL within the framework of the SABER project. In particular, a new method for solving the system of radiative transfer and statistical equilibrium equations is used. This couples more accurately the 2.7, 4.3 and $N_2(1)$ states (the v_3–system), and also the v_3 and v_2 (15 μm) systems. As a result, this leads to consistent day/night differences in the 15 μm levels. Other improvements have been included in the calculation of the solar photoabsorption rates, the revision of some rate constants, the radiative losses by laser emissions at 10 μm, the radiative transfer in the 2.7 μm levels, and the inclusion of additional collisional processes of moderate significance.
The model has also been extended to other important vibrational levels as the 626–2.0 μm states, and the 15 μm levels of the very minor isotopes. More details of the current model can be found in López-Puertas and Taylor (2001) [65] and in Wintersteiner et al. (2002) [75]. Fig. 1 shows an example of the vibrational temperatures for the CO_2 major isotope for levels from the lowest energy (15 μm) to higher (2.0 μm).

O_3: A new non-LTE model has been used to calculate the vibrational temperatures of O_3 levels. A brief description of the model can be found in López-Puertas and Taylor (2001) [65] and a more detailed in Martín-Torres and López-Puertas (2002) [76]. The model computes vibrational temperatures for 249 levels. The major improvements in this model with respect to the previous one are:

(i) The inclusion of radiative transfer in the ν_1, ν_2, and ν_3 fundamental bands.

(ii) The absorption of solar radiation in the 4.8 μm bands.

(iii) The use of a novel collisional scheme with a new parameterization of the relaxation of the highly excited vibrational levels.

(iv) The inclusion of the results of the analysis of the ISAMS O_3 data, principally the use of a nascent distribution for $O+O_2+M \rightarrow O_3(v_1,v_2,v_3)+M$ which favours the population of the $O_3(v_1,v_2,v_3)$ highest energy levels.

(v) The use of consistent O_3 and O abundance profiles, which is very important for calculating accurate O_3 vibrational temperatures in the mesosphere.

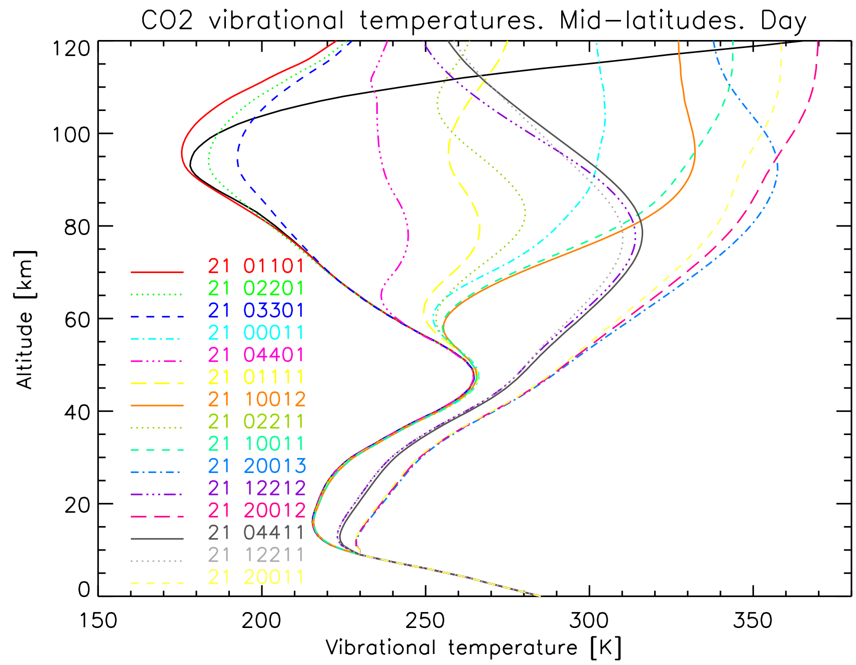

Figure 1: Vibrational temperatures for CO_2 vibrational levels for midlatitude daytime conditions.

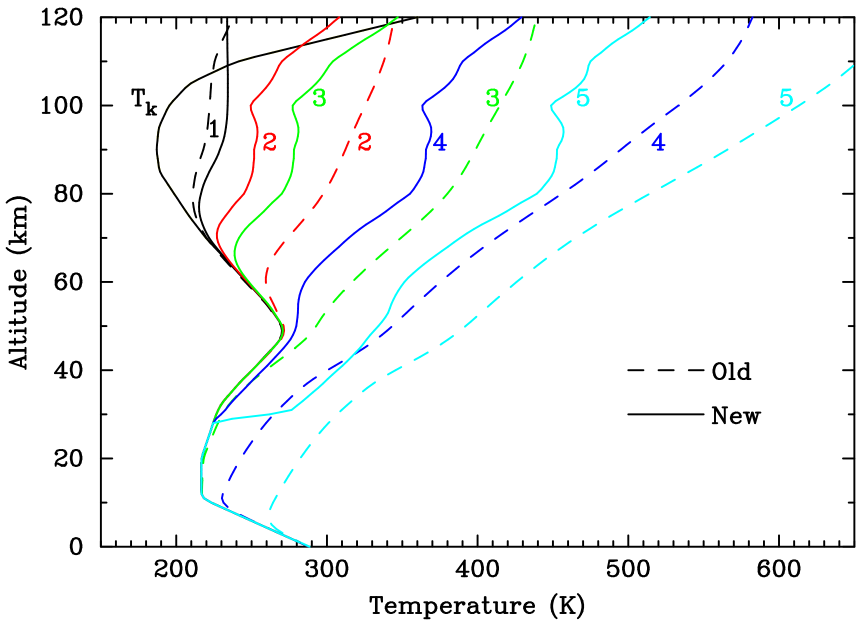

Figure 2: Comparison of the vibrational temperatures for the $O_3(0,0,v_3{=}1–5)$ levels for the mid-lat day reference atmosphere. Dashed: previous calculations; solid: new calculations.

As a result, the O_3 vibrational temperatures are rather different. Fig. 2 shows some comparison with previous values. The lowest energy levels ($v_1{=}v_2{=}v_3{=}1$) have now significantly larger vibrational temperatures in the mesosphere, while the higher-energy ($v_1,v_2,v_3{\geq}2$) levels are much less populated. Figs. 3–6 show some examples of the O_3 vibrational temperatures for the v_1, v_2, and v_3 levels. One major feature is that, in general, the v_2 levels are much more populated than their

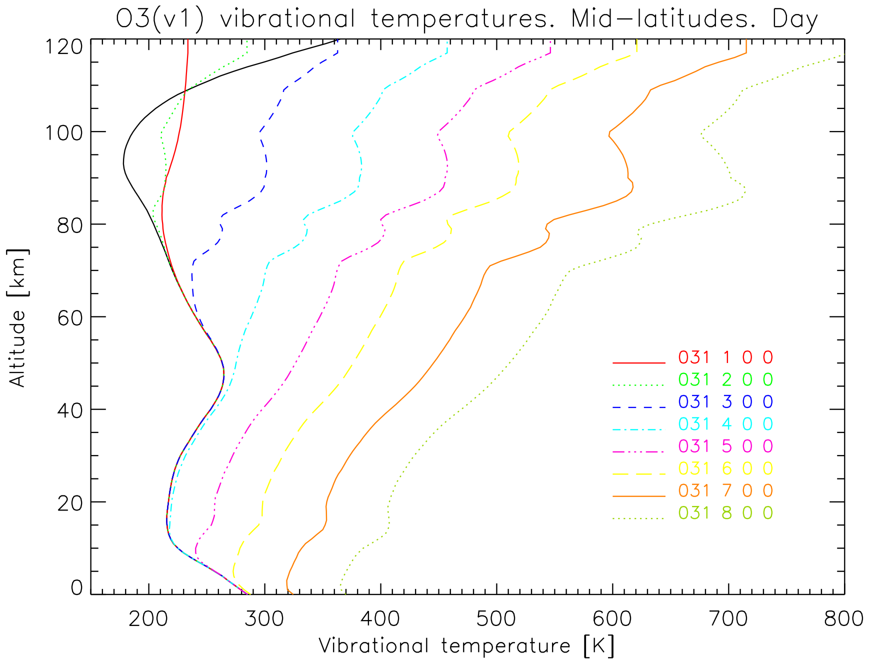

Figure 3: Vibrational temperatures for $O_3(v_1{=}1\text{–}8)$ levels for midlatitude daytime conditions.

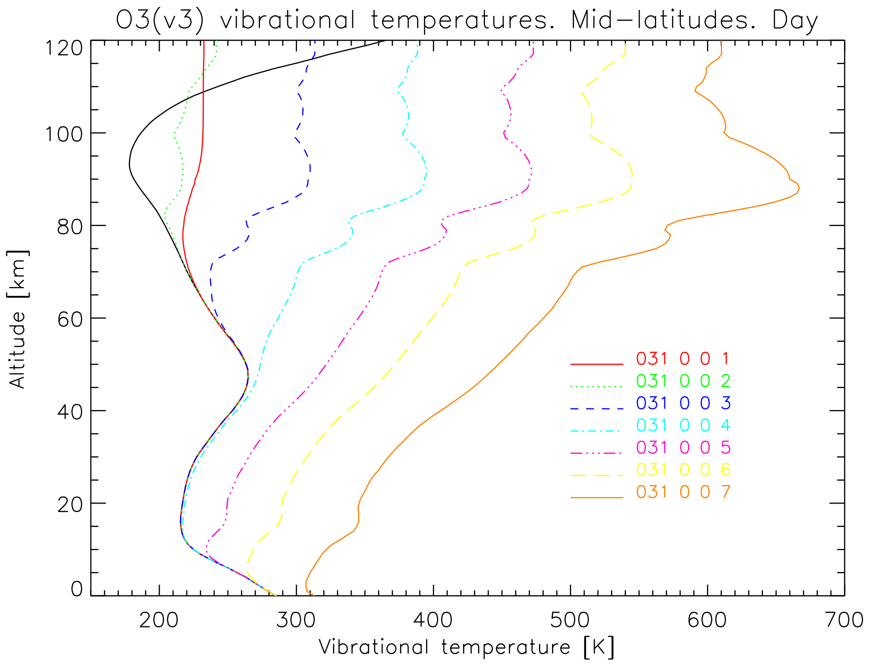

Figure 4: Vibrational temperatures for $O_3(v_3{=}1\text{–}7)$ levels for midlatitude daytime conditions.

corresponding v_1 and v_3 states (see Fig. 6).

H_2O: The non-LTE model used for the calculations of the H_2O vibrational temperatures has been updated with the results obtained from the analysis of the CIRRIS-1A and CRISTA data. Table 6 summarizes the major parameters affecting the H_2O vibrational temperatures and their

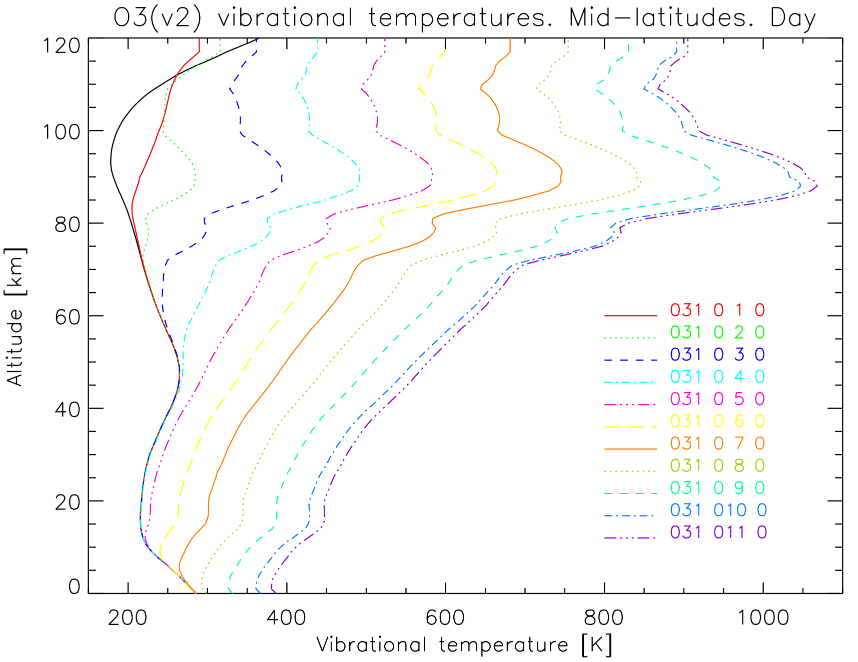

Figure 5: Vibrational temperatures for $O_3(v_2{=}1\text{–}11)$ levels for midlatitude daytime conditions.

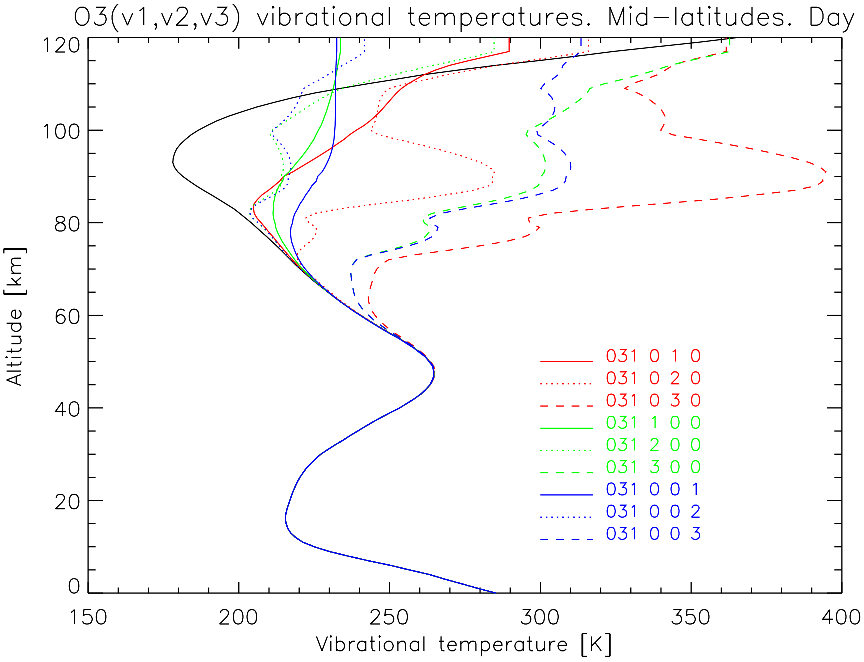

Figure 6: Vibrational temperatures for some $O_3(v_1,v_2,v_3)$ levels for midlatitude daytime conditions.

values derived from those experiments. The mid-point values derived from the CRISTA experiment have been used in these calculations.

In addition to those improvements, the Curtis matrices of the strongest H_2O bands, and the tropospheric flux in all the H_2O bands have been calculated more accurately. Also, consistent O_3 and O profiles have been used. The latter is not so important as for O_3 but might have significant

Table 6: H_2O non-LTE parameters.

Parameter	Inst.	Minimum	Nominal	Maximum
k_{vv}, $\times 10^{-12}$, $H_2O(010)$–$O_2(1)$	ISAMS	1.0	1.7	3.1
	CRISTA	-	1.7	3.1
	CIRRIS	0.9	1.5	
k_{vt}, $\times 10^{-12}$, $O_2(1)$+O	ISAMS	0.65	1.3	2.6
	CRISTA	0.7	1.3	-
ϵ, O_3+h$\nu \rightarrow O_2(1)$	ISAMS	2	4	6
	CRISTA	-	4	6

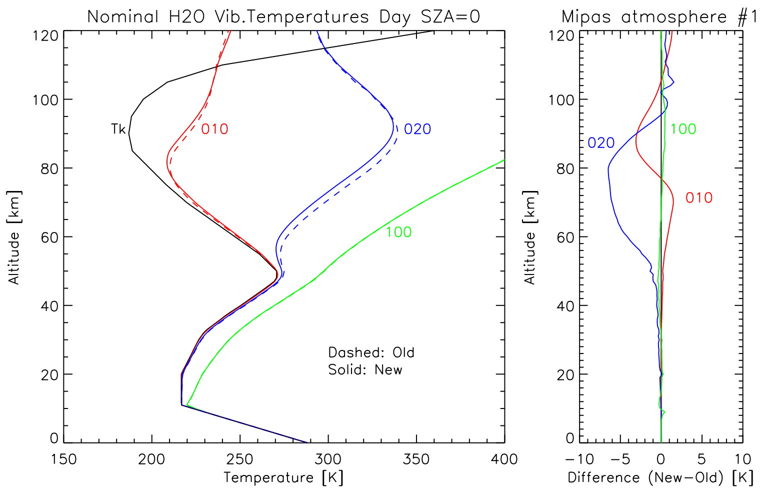

Figure 7: Comparison of the vibrational temperatures for H_2O levels for the mid-lat day atmosphere. Left panel: vibrational temperatures; dashed: previous calculations; solid: new calculations. Right panel: vibrational temperature differences.

effects since O_3 intervene in the excitation of $O_2(1)$, and O in the subsequent thermalization of $O_2(1)$. Any inconsistency in the O_3/O ratio can directly influence the $O_2(1)$ population and hence that of $H_2O(010)$.
Figures 7 and 8 show some comparisons with previous values. The differences for the levels of the main isotope (Fig. 7) are not very large. Those of the (010) level of the minor isotopes are significantly smaller now in the upper mesosphere (see Fig. 8). This is due to a more accurate inclusion of the tropospheric flux, which was previously overestimated.

NO: A new model for the NO(v) vibrational states has been included. The improvements are as follows:

(i) The model has been extended to the v=2 and 3 vibrational states. Previously, only the v=1 state was considered.

(ii) Rotational and spin non-LTE have been included for the 3 vibrational levels.

(iii) Absorption of the tropospheric flux has been included very accurately.

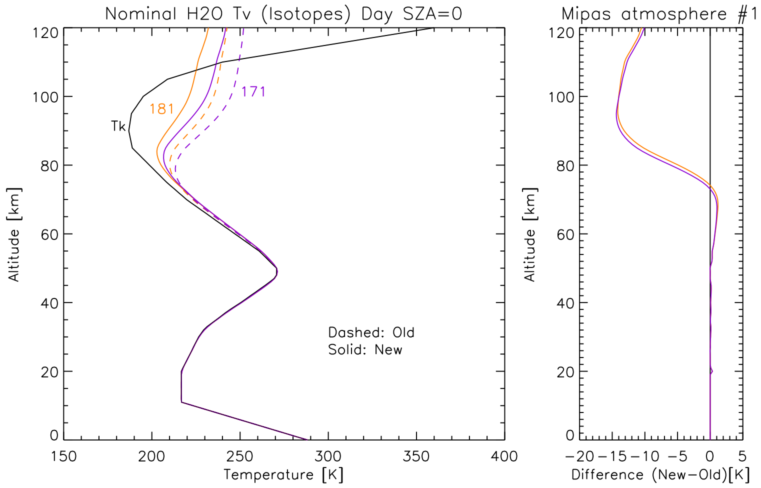

Figure 8: Vibrational temperatures for the (010) level of the H_2O minor isotopes for the mid-lat day atmosphere. Left panel: vibrational temperatures; dashed: previous calculations; solid: new calculations. Right panel: vibrational temperature differences.

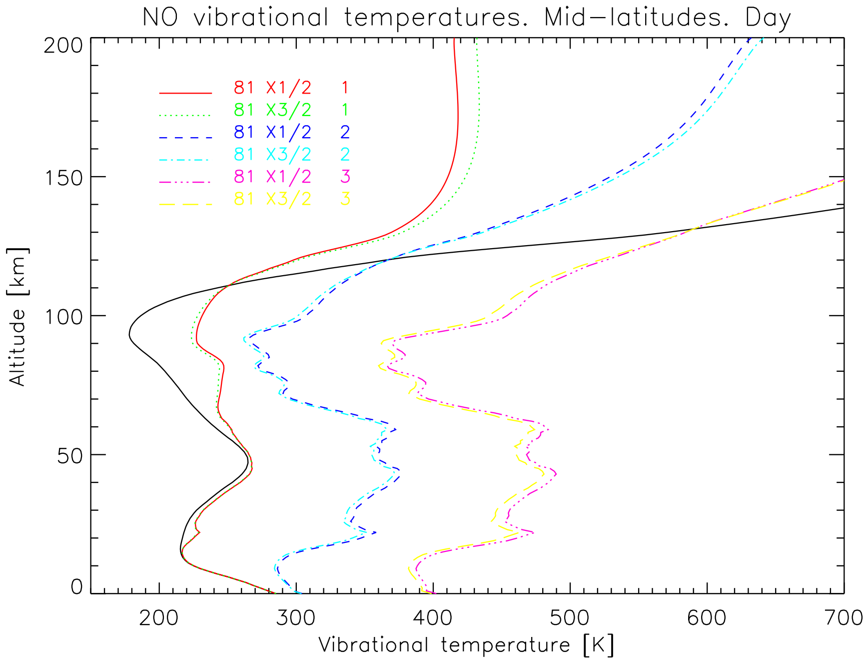

Figure 9: Vibrational temperatures for NO(v=1–3) for the mid-latitude daytime reference atmosphere.

(iv) Exchange between atmospheric layers has also been included.

(v) The chemical and photochemical production of NO(v) in the stratosphere has been included.

(vi) The collisional processes have been updated, including the recent analysis of the CIRRIS-1A data and the newly measured rate for $NO(1)+O \rightleftharpoons NO+O$, which is 2.3 times smaller than the previous value.

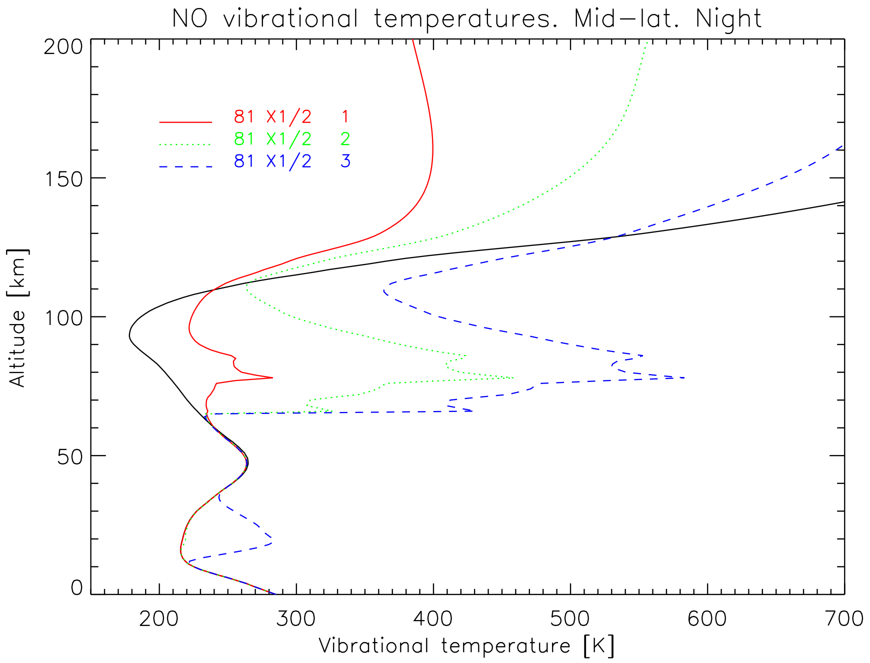

Figure 10: Vibrational temperatures for NO(v=1–3) for the mid-latitude nighttime reference atmosphere.

Table 7: NO collisional processes.

No.	Process/$f(v)$	T_e^r(K)	$k^\dagger$
1a	$NO(1,J,S) + O_2 \rightleftharpoons NO(0,J',S') + O_2$	T	2.4×10^{-14}
1b	$NO(1,J,S) + O \rightleftharpoons NO(0,J',S') + O$	$0.74T + 24$	2.8×10^{-11}
2a	$NO(2,J,S) + O_2 \rightleftharpoons NO(1,J',S') + O_2$	T	7.4×10^{-14}
2b	$NO(2,J,S) + O \rightleftharpoons NO(1,J',S') + O$	$0.74T + 24$	1.3×10^{-11}
3	$NO(2,J,S) + O \rightleftharpoons NO(0,J',S') + O$	$0.74T + 24$	1.8×10^{-11}
4	$NO_2 + O \rightarrow NO(v,J,S) + O_2$ $f(v=0,1,\geq2)=0.681, 0.222, 0.070$	T	9.7×10^{-12}
5	$NO_2 + h\nu \rightarrow NO(v,J,S) + O$ $f(v)$: altitude dependent	5000	
6	$N(^2D) + O_2 \rightarrow NO(v,J,S) + O$ $f(v=0,1,\geq2)=0.03, 0.05, 0.92$	T	5.7×10^{-12}
7a	$N(^4S)_{thermal} + O_2 \rightarrow NO(v,J,S) + O$ $f(v=0,1,\geq2)=0.04, 0.07, 0.89$	3000	1.15×10^{-11} $\exp(-3503/T)$
7b	$N(^4S)_{sup-ther} + O_2 \rightarrow NO(v,J,S) + O$ $f(v=0,1,\geq2)=0.04, 0.07, 0.89$	5000	

$T_e^s = T$ for collisions with O_2 and $T_e^s = 200\,K$ for collisions with $O(^3P)$.

The processes considered in the model are summarized in Table 7. A detailed description of the model can be found in Funke and López-Puertas (2000) [77] and López-Puertas and Taylor (2001) [65].

Figures 9, 10, and 11 show some typical examples for the NO(v) vibrational levels. They clearly show the chemical excitation in the daytime stratosphere. It is also noticeable how the vibrational

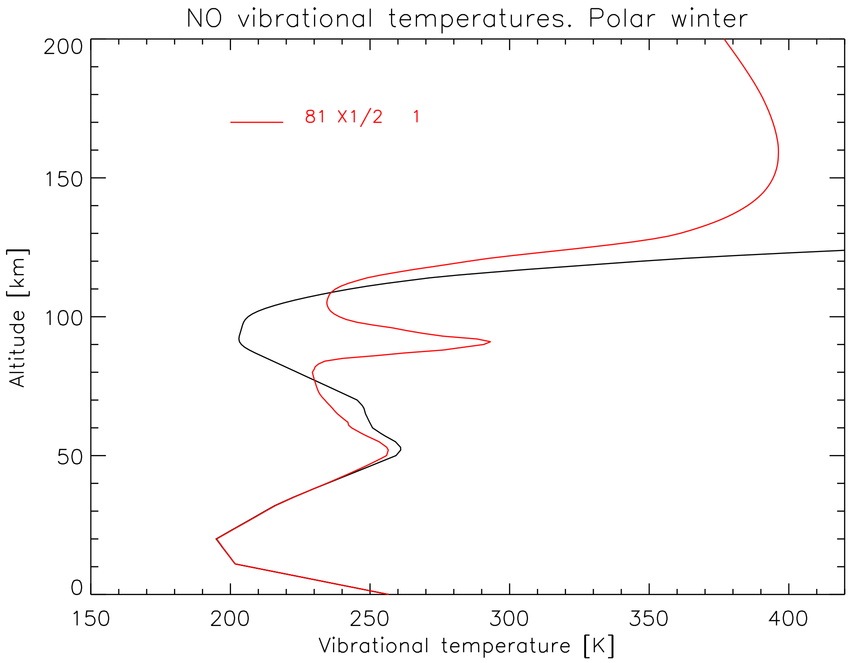

Figure 11: Vibrational temperature for NO(v=1) for the polar winter reference atmosphere.

temperature of NO(1) is significantly smaller than the kinetic temperature in the polar winter lower mesosphere (see Fig. 11). The peak in the upper mesosphere is caused by the concentrations of NO and NO_2 in the reference atmospheres. It is probable that this peak is not realistic.

N_2O: A new model for the vibrational temperatures of the $N_2O(v_1,v_2,v_3)$ levels has been included. The previous model was rather crude and treated the radiative transfer very approximated. We have calculated vibrational temperatures for 41 (v_1,v_2,v_3) levels emitting near 17, 7.8, and 4.5 μm. The model is described in López-Puertas and Taylor (2001) [65]. We give here a brief summary. The model includes the following processes:

(i) Radiative processes: Spontaneous emission, absorption of tropospheric flux, absorption of solar radiation, and, for the strongest bands, exchange of radiation between atmospheric layers.

(ii) Collisional processes: Vibrational-thermal and vibrational-vibrational collisional processes with $N_2(1)$ and O_2 (1). This requires the coupling with the CO_2 and H_2O models described above.

The concrete processes and collisional relaxation rates are described in López-Puertas and Taylor (2001) [65].
Figures 12 and 13 show the vibrational temperatures for most of the levels for the mid-latitude daytime atmosphere. They show typical aspects as those of other molecules. The lower energy levels are generally closer to LTE, while the high energy ones are considerably away from LTE mainly because of the absorption of solar radiation. More details of the vibrational temperatures can be found in López-Puertas and Taylor (2001) [65].

OH: The vibrational temperatures of the OH(v=1–9) vibrational levels have been included in the climatology for the first time. They are excited by the Bates-Nicolet reaction: $O_3+H \rightarrow OH(v \leq 9)+O_2$, and de-excited by spontaneous radiative emission and thermal quenching: $OH(v)+M \rightleftharpoons OH(v'<v)+M$.

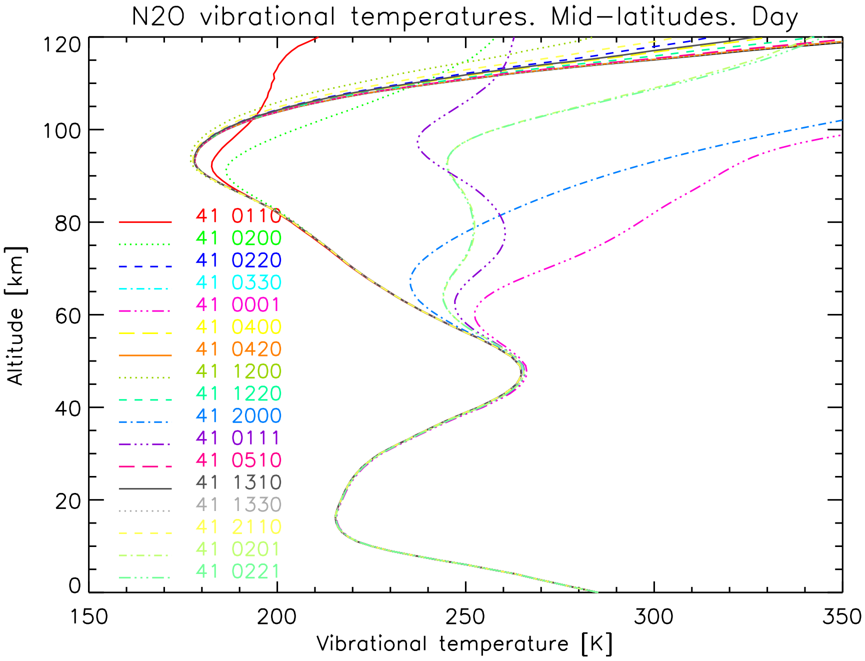

Figure 12: Vibrational temperatures for $N_2O(v_1,v_2,v_3)$ lower energy levels for the mid-latitude daytime reference atmosphere.

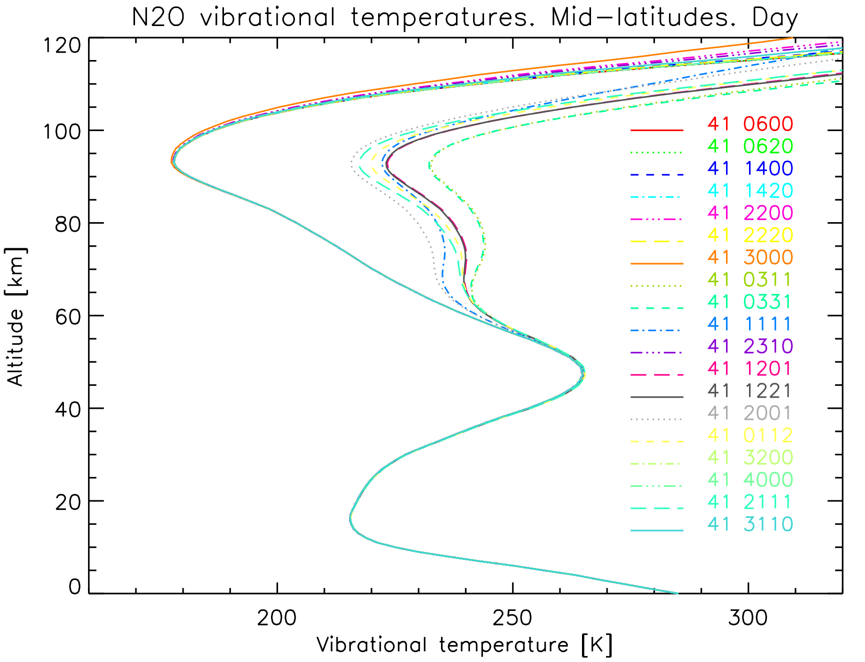

Figure 13: Vibrational temperatures for $N_2O(v_1,v_2,v_3)$ higher energy levels for the mid-latitude daytime reference atmosphere.

Typically the population of OH(v=1–9) are not given by vibrational temperatures but by their number densities. Here, to make them comparable to other species, we have plotted vibrational temperatures. They are generally much larger than those of other species (see Figs. 14 and 15).

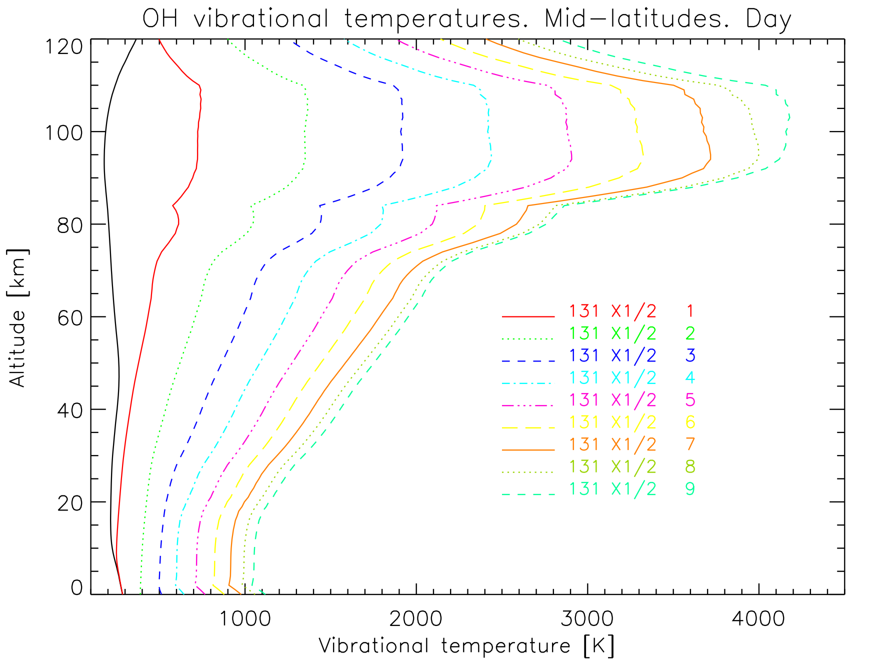

Figure 14: Vibrational temperatures for OH(v=1–9) for the mid-latitude daytime atmosphere.

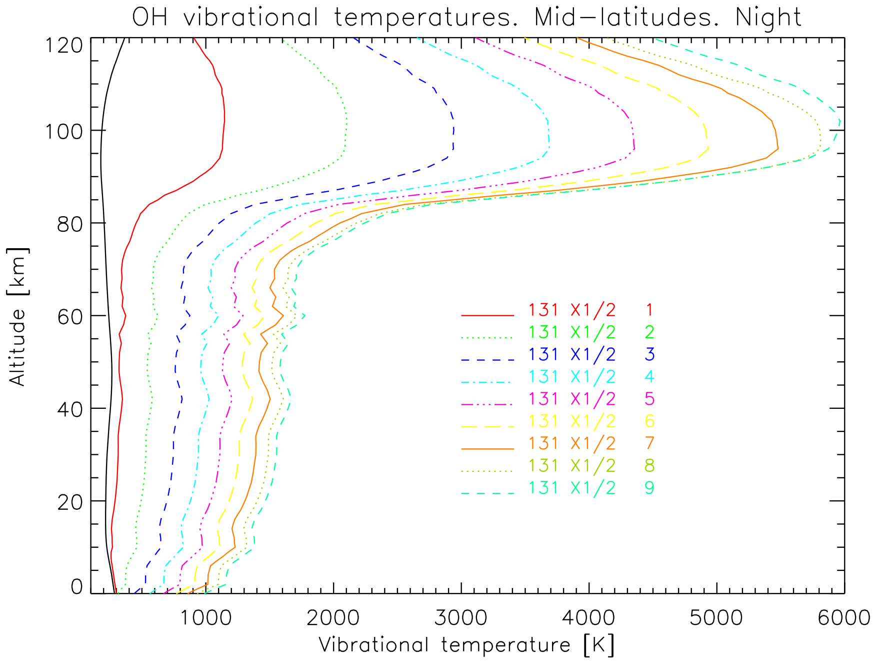

Figure 15: Vibrational temperatures for OH(v=1–9) for the mid-latitude nighttime atmosphere.

Note also that they are larger for nighttime than for daytime around the mesopause, because O_3 is more abundant at nighttime. More details of the vibrational temperatures can be found in López-Puertas and Taylor (2001) [65].

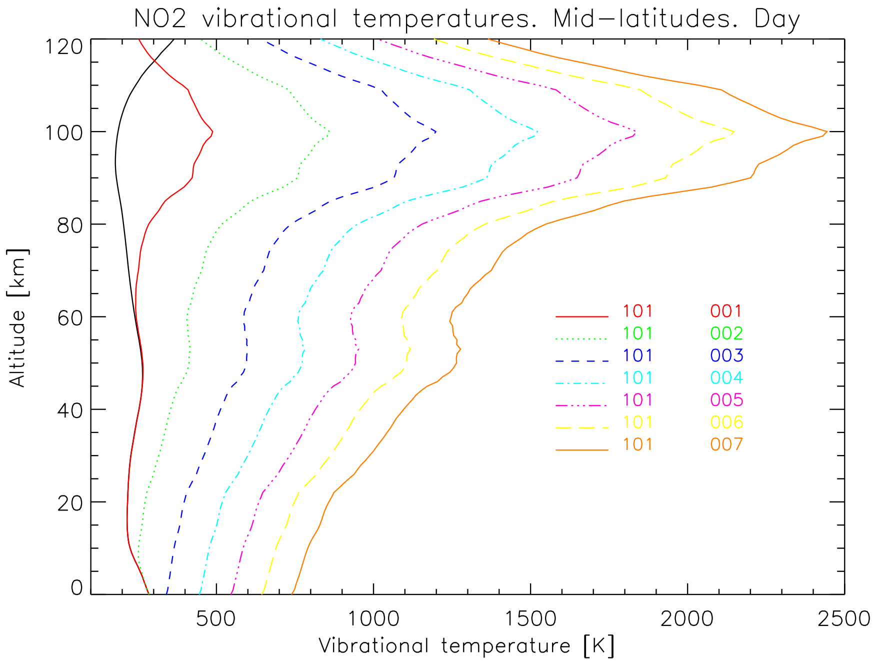

Figure 16: Vibrational temperatures for NO_2 for the mid-latitude daytime atmosphere.

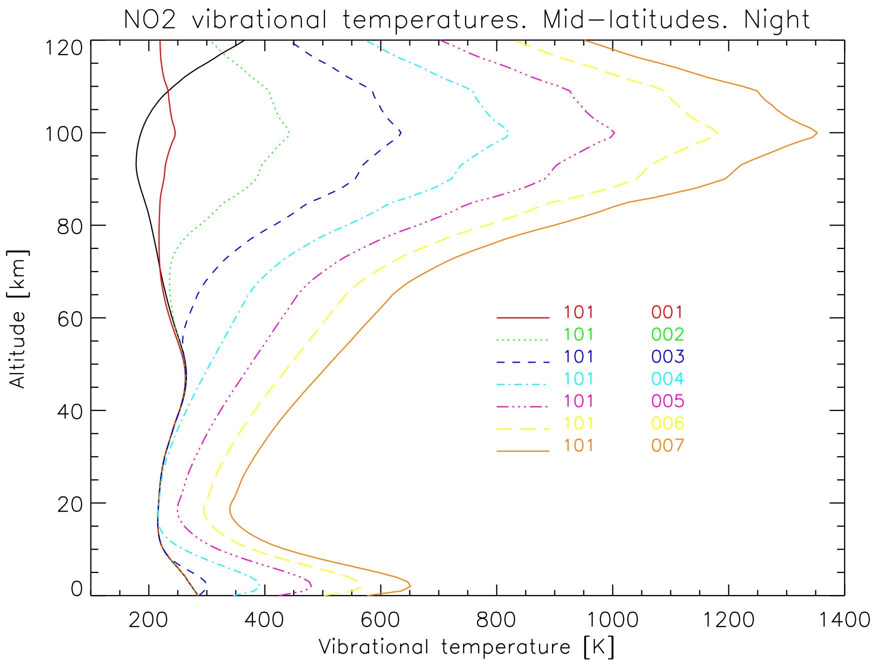

Figure 17: Vibrational temperatures for NO_2 for the mid-latitude nighttime atmosphere.

CO, CH_4, NO_2, and HNO_3: The vibrational temperatures of CO, CH_4, and HNO_3 have experimented little changes. They have been improved by a more accurate implementation of the absorption of the tropospheric flux. The changes are very little and are more significant for nighttime conditions, when the absorption of the tropospheric upwelling flux ('earthshine') is more important. The general behaviour is that we have slightly smaller vibrational temperatures in the

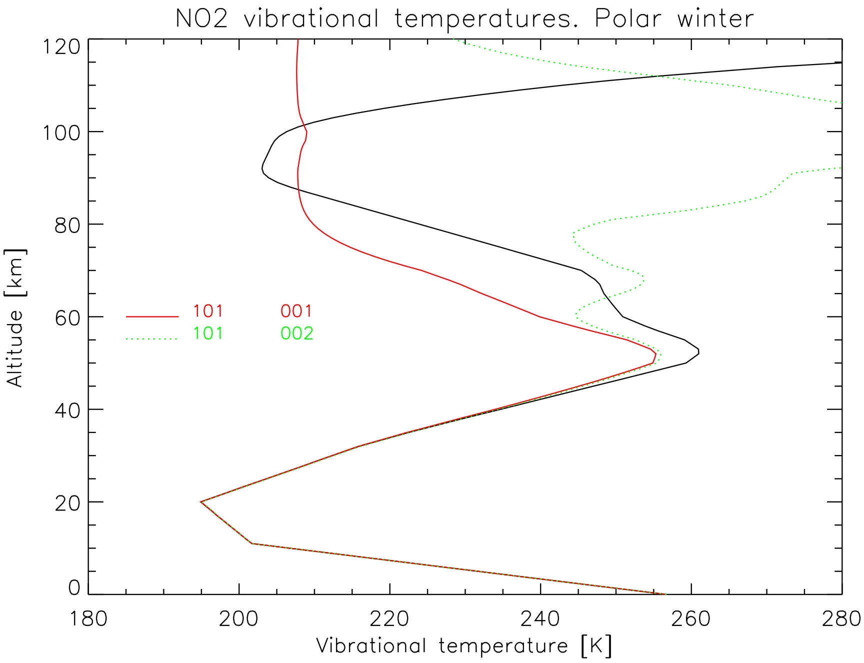

Figure 18: Vibrational temperatures for NO_2 for the polar winter reference atmosphere.

upper mesosphere for nighttime conditions.

The vibrational temperatures of NO_2 are significantly different. The processes considered are the same as previously and with the same rates. They are, however, very sensitive to the populations of O_3, NO, and to NO_2 itself. So the differences actually reflect the new species abundance profiles. A example of the vibrational temperatures obtained for daytime and nighttime conditions are shown in Figs. 16 and 17. The important case of underpopulation of the first excited v_3 level, responsible for the NO_2 fundamental band near 6.5 μm, in the polar winter upper stratosphere and mesosphere is also shown in Fig. 18.

Summary and Conclusions: Overall, the new set of vibrational temperatures has been considerably extended and improved. Vibrational temperatures for one new molecule have been included. Three new non-LTE models (O_3, NO, N_2O and OH) have been developed and used. Others (CO_2 and H_2O) have been considerably extended. The reference atmospheres have been corrected to accurately include the non-LTE enhancements. The results of the most recent analyses of non-LTE emissions of satellite instruments have been incorporated. The collisional rates of many reactions have been updated, and the radiative transfer has been improved in many cases. As a result, the present vibrational temperature climatology can be considered as the most complete, comprehensive and accurate compilation of non-LTE populations ever done.

Radiative Transfer Calculations (WP 3300)

Each participant has performed radiative transfer calculations for the scenarios defined in WP 3100, as far as the particular case was supported by the relevant radiative transfer algorithm. Spectra have been sent to IMK for intercomparison. The complete results are compiled in a dedicated report [64].

Intercomparison (WP 3400)

Line Intensities and Evaluation of Spectral Lineshape: First, the calculation of line intensities and the evaluation of spectral line shapes has been assessed for various pressures and temperatures. Three different pressures were chosen, corresponding to dominating pressure broadening, to dominating Doppler broadening, and to balanced pressure and Doppler broadening, respectively. Calculations were carried out for the HITRAN reference temperature 296 K as well as for 250 K which is more realistic for stratospheric conditions. In order to better detect detail differences between the modeling approaches, single transition monochromatic transmittance spectra have been intercompared, i.e. spectra which have not been convolved by any instrument line shape function (tests 1–3 and 7–9).

In test 2, which serves as an example for illustration, and throughout all cell transmittance calculations, the RFM and FM2D results agree extraordinarily well (Fig. 19). This is explained by the fact that both FM2D and RFM use the same modified Humlicek algorithm by Wells [28]. The KOPRA relies on a Humlicek implementation by Kuntz [9]; differences between the original Humlicek and the Kuntz implementation are below 2×10^{-6}; differences RFM-KOPRA and FM2D-KOPRA are explained by the use of different Humlicek implementations, which switch between accuracy–driving Humlicek regions at slightly different distances from the line center. However, since the differences are very small, they are not of relevance.

The OFM uses the original Humlicek algorithm [10] but switches to pure Lorentzian lineshape quite close to the line center; the major part of differences is attributed to the fact that the OFM calculates the Voigt function only in some points and uses linear interpolation in between.

MIRART uses yet another Voigt implementation, utilizing the Hui et al. approach [31] near the line center, Lorentzian line shape in the far wings, and Humlicek [10] in between. The structure in the difference plot is explained by the fact that for this case MIRART calculates only three data points by means of Humlicek region 1, and switches to Lorentzian shape quite soon. By application of the Voigt instead Lorentzian lineshape within a wider spectral interval around the line center, this discrepancy could be removed. The accuracy of the Humlicek 1982 algorithm is about 10^{-4}, the accuracy of the Hui algorithm is about 10^{-5} to 10^{-6}. Thus, the use of different Voigt algorithms can explain the observed differences. All differences are in the order of size or smaller than the accuracy specification of the original Humlicek algorithm, i.e. 10^{-4}.
Comparison spectra calculated for 296 K and such calculated for 250 K gives no hint at any particular problem with temperature dependence of line intensities, except for MIRART, which reveals a factor of two larger differences than for 296-K case. There seems to be a component in the differences which is caused by the temperature dependent line intensity. MIRART uses the scheme as proposed by Ref [37], while all the other codes use the Gamache [26] total internal partition sum parametrization.
In summary, it can be concluded from test cases 1–3 and 7–9 that the calculation of line strengths and the evaluation of the line shapes is performed by each code within the individual accuracy specification.

Instrument Line Shape: In a next step, monochromatic spectra were convolved by an instrument line shape (Tests 4 – 6). While some codes include tools to provide instrument line shapes for dedicated instrument specifications (e.g. KOPRA [78]), this intercomparison focuses on the case of a pretabulated instrument line shape (Test 6), which was an "ideal" Fourier transform spectrometer line shape related to 20 cm optical path difference plus Norton–Beer "strong" apodization [45]. All the differences in the calculated spectra are very small and probably not relevant for real data analysis. A small offset of -0.4×10^{-6} between the RFM and KOPRA is attributed to renormalization of the ILS by the RFM (the numbers in the supplied ILS add up to 10000.047). Some structure in the RFM-KOPRA difference is caused by numerical precision – running the – RFM

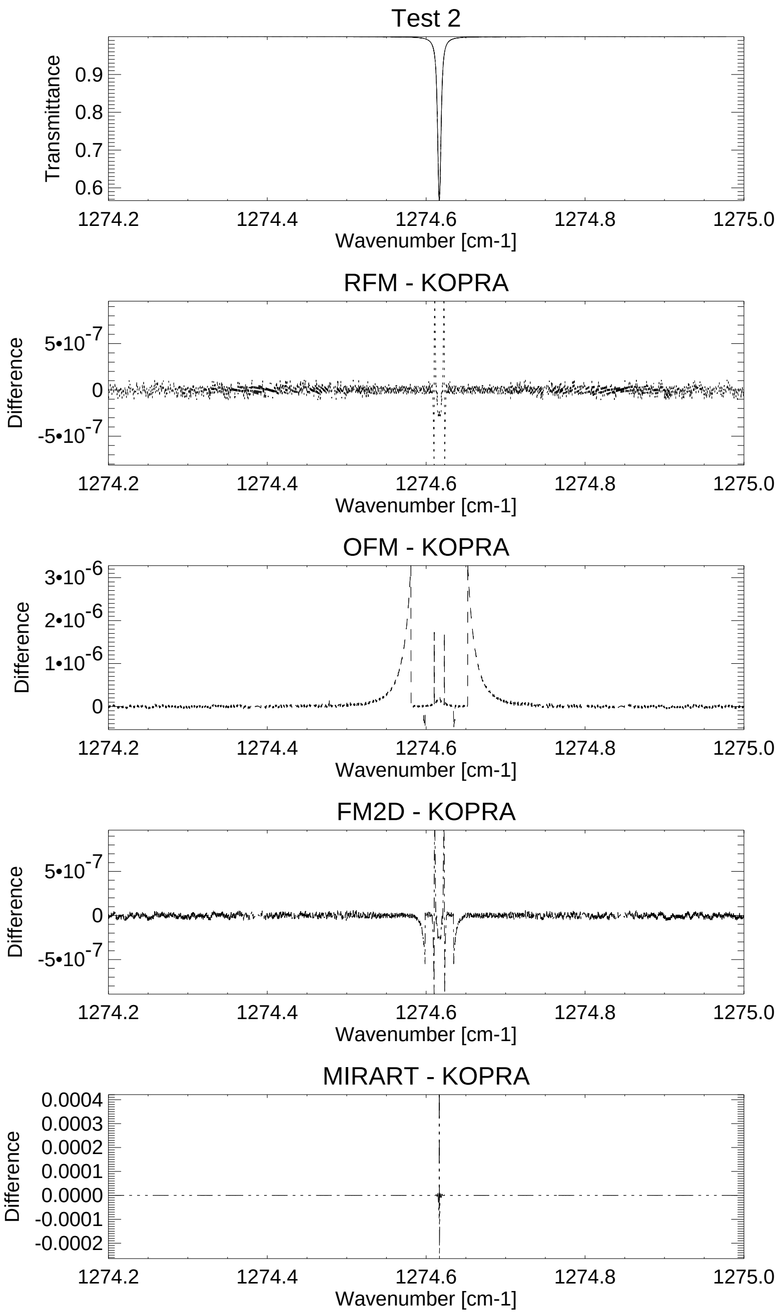

Figure 19: Results of test case 2. The uppermost panel shows the spectrum, whereas the other panels show difference spectra with respect to KOPRA. Differences between spectra are such small that they are not resolved in the uppermost panel.

with double–precision output produces a similar signature when compared to the RFM default single precision output. In summary, there is no evidence of any substantial convolution problem in any of the codes.

Line Rejection Criteria: In theory every transition contributes to the signal at every frequency grid point. Since consideration of all transitions obviously is not practicable, each model applies a line wing truncation or line rejection criterion, which is driven by the optimal trade–off between computational efficiency and accuracy. Different choice or implementation of such criteria leads to remarkable different results in test cases 10 and 11:
In test case 10 (Fig. 20), both RFM and FM2D spectra reveal smaller continuum–type background extinctions than KOPRA spectra. RFM uses a ± 25 cm^{-1} line rejection criterium around each 1 cm^{-1} sub–interval; KOPRA uses a $\pm$ 25 cm^{-1} line rejection criterium around the microwindow boundaries, i.e. uses more transitions outside the microwindow, which explains the larger background absorption in KOPRA spectra. Due to nonlinearity in radiative transfer, different background signal also causes different signal in line peaks. In MIRART, line wings truncated at 10 cm^{-1} from the line center per default, except for H_2O-lines, where line wings are truncated at ± 25 cm^{-1} in order to comply with the water vapour continuum implementation.

Self Broadening: Large OFM-KOPRA differences in test case 10 are explained by the fact that the OFM code does not consider self–broadened half–widths; the half–widths of all the lines are calculated using only the air–broadened half–width parameter. This approximation should not turn out to be too rough in real atmospheres, but makes a substantial difference in high–resolution cell transmittance calculations.

In contrast, the IROE1 code includes the "correct" calculation of self–broadening. Therefore IROE1 results agree much better with the other codes than the OFM. The residual difference is explained by interpolation effects as explained under test cases 1 ff. These interpolation effects add up in case of multi–transition calculations.

Chi–Factor Implementation: All chi–factor implementations rely on references [79, 80, 81]. In test case 11, any chi–factor related problems are masked and partly compensated by the differences caused by different treatment of line wings discussed above. To isolate the test of the chi–factor, difference spectra computed with and without the chi–factor have been calculated for the KOPRA and the RFM (Fig. 21). The net effect of chi–factors is considerably different in KOPRA and RFM for both models, and is masked and partly compensated by the differences caused by different treatment of line wings.

The OFM uses the same line rejection criterion as KOPRA; thus differences are significantly smaller than RFM-KOPRA. Differences are much smaller than a tenth of a percent of the net effect of the chi–factor. FM2D does not inlude any chi–factors, which explains the difference and reveals the importance of the chi–factor in this wavenumber region.

Assessment of test case 12, which is identical to case 11 except that the temperature is 250 K gives no evidence of any problems related to the temperature dependence of the chi–factor, since no additional residuals are visible in comparison to Exercise 11.

Line Coupling: The line coupling characteristics of the forward model was assessed for $\Sigma - \Pi$-type bands and for $\Pi - \Delta$-type band. Tests 13–14 assess the CO_2 Q-branch near 720 cm^{-1} (sigma pi), whereas tests 15–16 cover the pi–delta–type CO_2 Q-branch near 741 cm^{-1}. Test cases

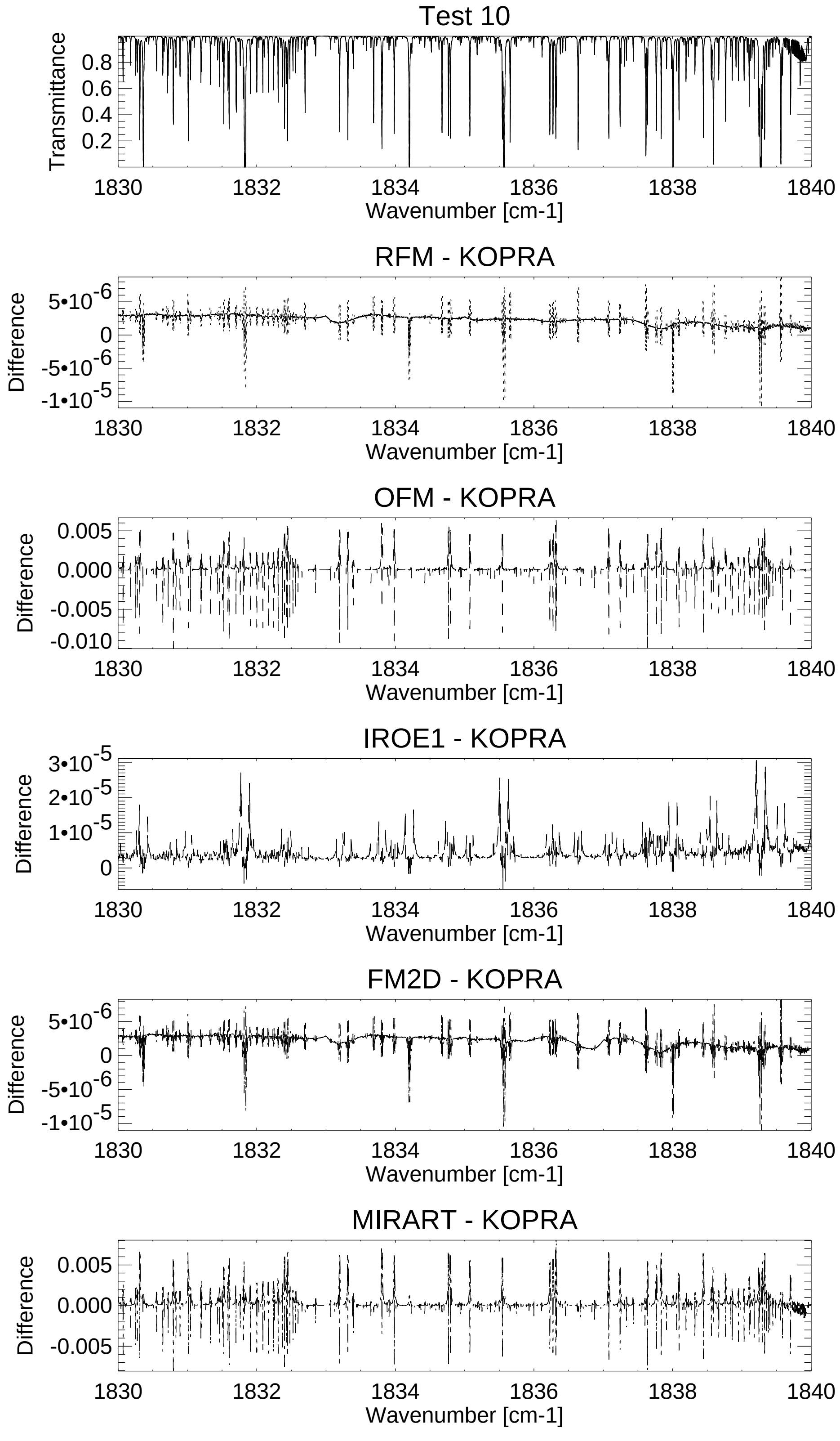

Figure 20: Results of test case 10. The uppermost panel is the KOPRA spectrum, whereas the other panels show difference spectra with respect to KOPRA. Differences between spectra are such small that they are not resolved in the uppermost panel.

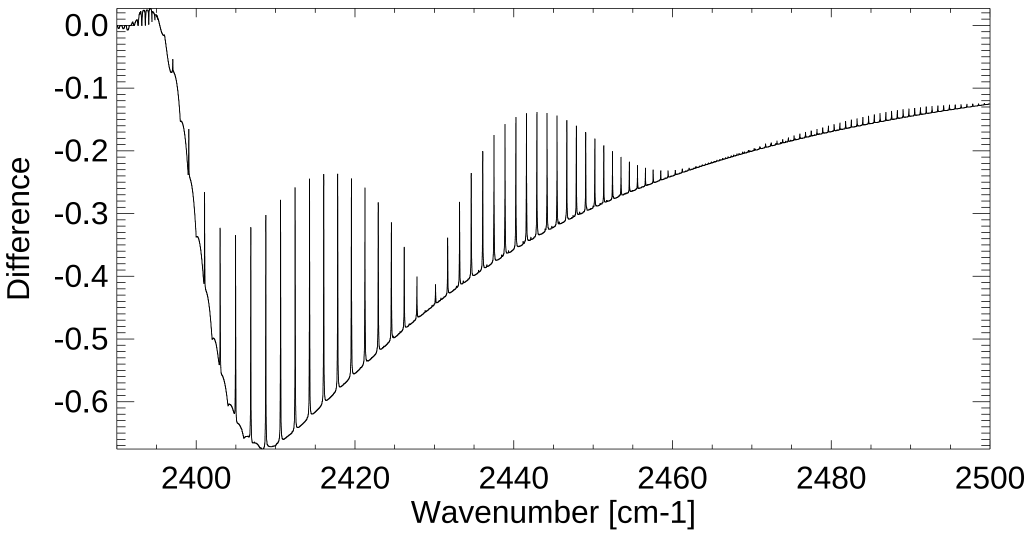

Figure 21: Transmittance difference of net effects of chi–factor application between RFM and KOPRA, calculated as (RFM(with chi–factor)-RFM(without chi–factor)-(KOPRA(with chi–factor)-KOPRA(without chi–factor))

22 and 23 are the related atmospheric limb emission scenarios. The RFM uses the Rosenkranz approximation [12] as described in Ref [82], while KOPRA supports the direct diagonalization approach, which is considered more accurate in particular for high pressures. Fig. 22 shows the results of test case 13, which is the 720 cm^{-1} Q-branch at 250 hPa. Comparison of net effects of line mixing in RFM and KOPRA spectra proves that the different treatment of line mixing is fully responsible for the differences between RFM and KOPRA spectra. Furthermore, by selecting the Rosenkranz approximation in KOPRA, the differences disappeared. At 50 hPa, the differences between RFM and KOPRA is a factor of 100 smaller than for the high–pressure case of test case 13. This is due to the fact that the KOPRA code switches automatically to the Rosenkranz approximation for lower pressures, since this algorithm then approximates the line coupling effect quite accurately. If the KOPRA code is forced to apply direct diagonalization also in this case, differences increase by a factor of three.
The OFM and FM2D codes do not consider line–mixing at all. This explains the differences and shows the significance of line–mixing for the given conditions. As expected, residuals are much lower (a factor of six) in the low pressure case than in the high-pressure case.

The same explanations apply to test cases 15 and 16 (pi–delta–type CO_2 Q-branch at 250 and 50 hPa, respectively). Application of the codes to atmospheric conditions (test case 22, 792 cm^{-1} CO_2 Q-branch) leads to deviations between RFM and KOPRA spectra of 0.6% at the band head, while the net effect of line mixing is 10%. Test case 23, which is identical to case 22 except that the MIPAS instrument line shape as well as the field of view are considered, proves that the relevance of line mixing clearly exceeds the MIPAS noise level (up to a factor of 10). Compared to test case 22, the differences between KOPRA and RFM are increased and are now in the order of size of the noise level. The dominating reasons for these discrepancies, however, are not the different line mixing implementations, but the different line wing cut–off criteria, as well as different numeric treatment of the integration of the radiance field over the non–infinitesimal instrument field of view. Even for these test cases under realistic conditions, i.e. atmospheric radiance spectra, MIPAS instrument line shape and field of view, line coupling remains the driving source of differences between KOPRA and RFM on the one hand and FM2D and the OFM on the other hand. These differences exceed the MIPAS noise level by far and reach 350–400 $nW/(cm^2\ sr\ cm^{-1})$.
Pressure shift was found to be important, too. This feature is included in all codes except the OFM. No pressure shift–related residuals were found in the spectra which have been calculated under consideration of pressure shift, unless for atmospheric calculations where different treatment of atmospheric refraction in one of the codes caused different effective pressure (test case 18).

Water Vapour Continuum: Test cases 17 and 26, where the water vapor continuum was assessed, have been chosen intentionally identical as for the "Intercomparison of Transmittance and Radiance Algorithms" (ITRA) in the late 80's [83], in order to allow further comparison. RFM and FM2D spectra agree extraordinarily well (Fig. 23); this is attributed to the fact that the basic theory and methodology for modelling far line wings / continuum are the same for the FM2D and the RFM; however, the practical implementation and code are different. Both codes use a Wells version of the Voigt routine [28].

The different line rejection criterion (c.f. test case 10) does not hold here as an explanation for differences between RFM-KOPRA and FM2D-KOPRA, because in case of activated continua–parametrizations, KOPRA also uses the grid point related rejection criterion at 25 cm^{-1} in order to be consistent with the continuum specification.

Several sinusoidal features with wavelengths 1 cm^{-1} are apparent in the difference spectra RFM-KOPRA and FM2D-KOPRA. This is, because for each 1 cm^{-1} interval, the RFM explicitly evaluates line wing contributions at 0.5 cm^{-1} spacing and interpolates other points using an inverse quadratic function.

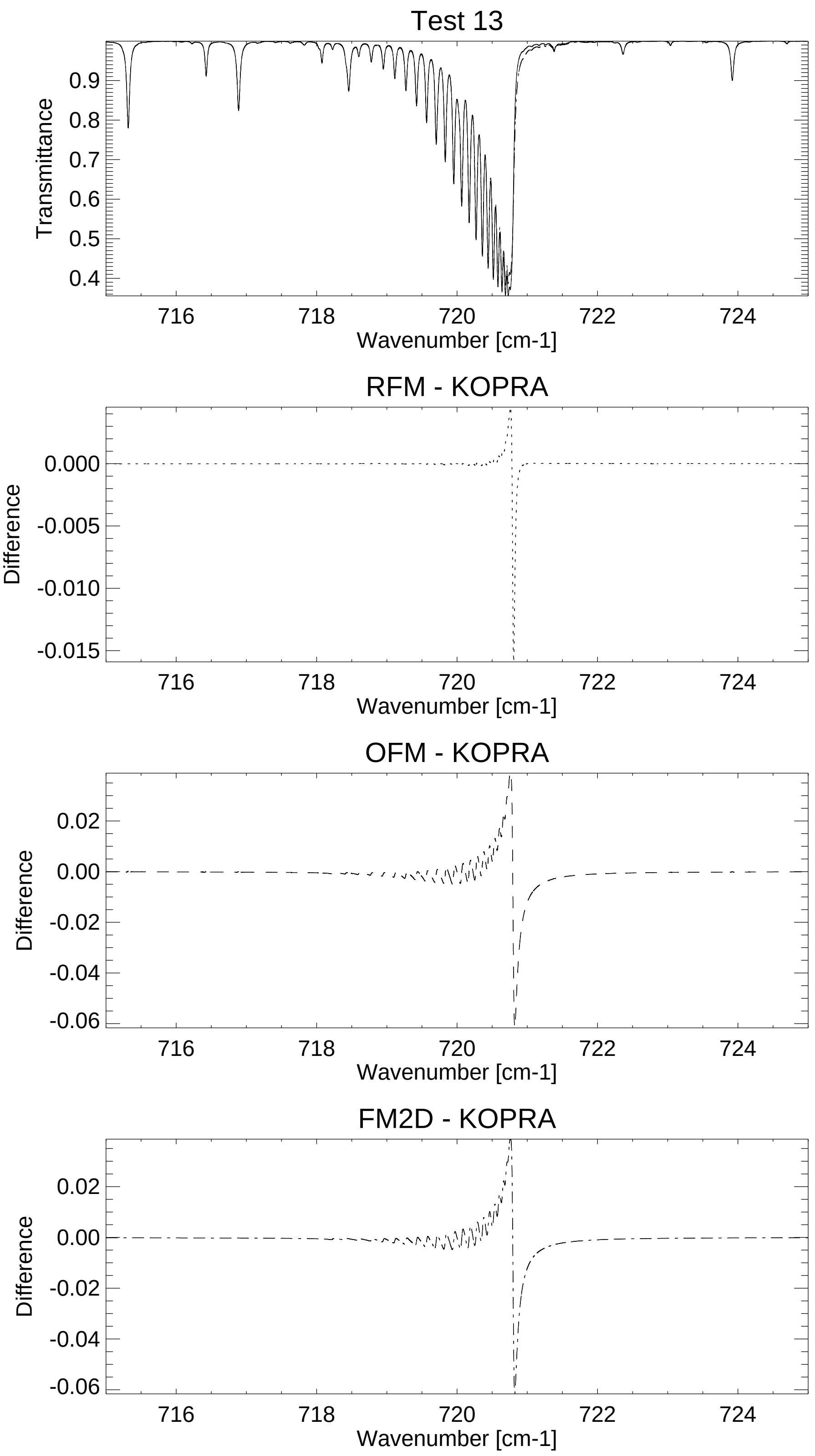

Figure 22: Results of test case 13. The uppermost panel is the KOPRA spectrum, whereas the other panels show difference spectra with respect to KOPRA. Differences between spectra are such small that they are not resolved in the uppermost panel.

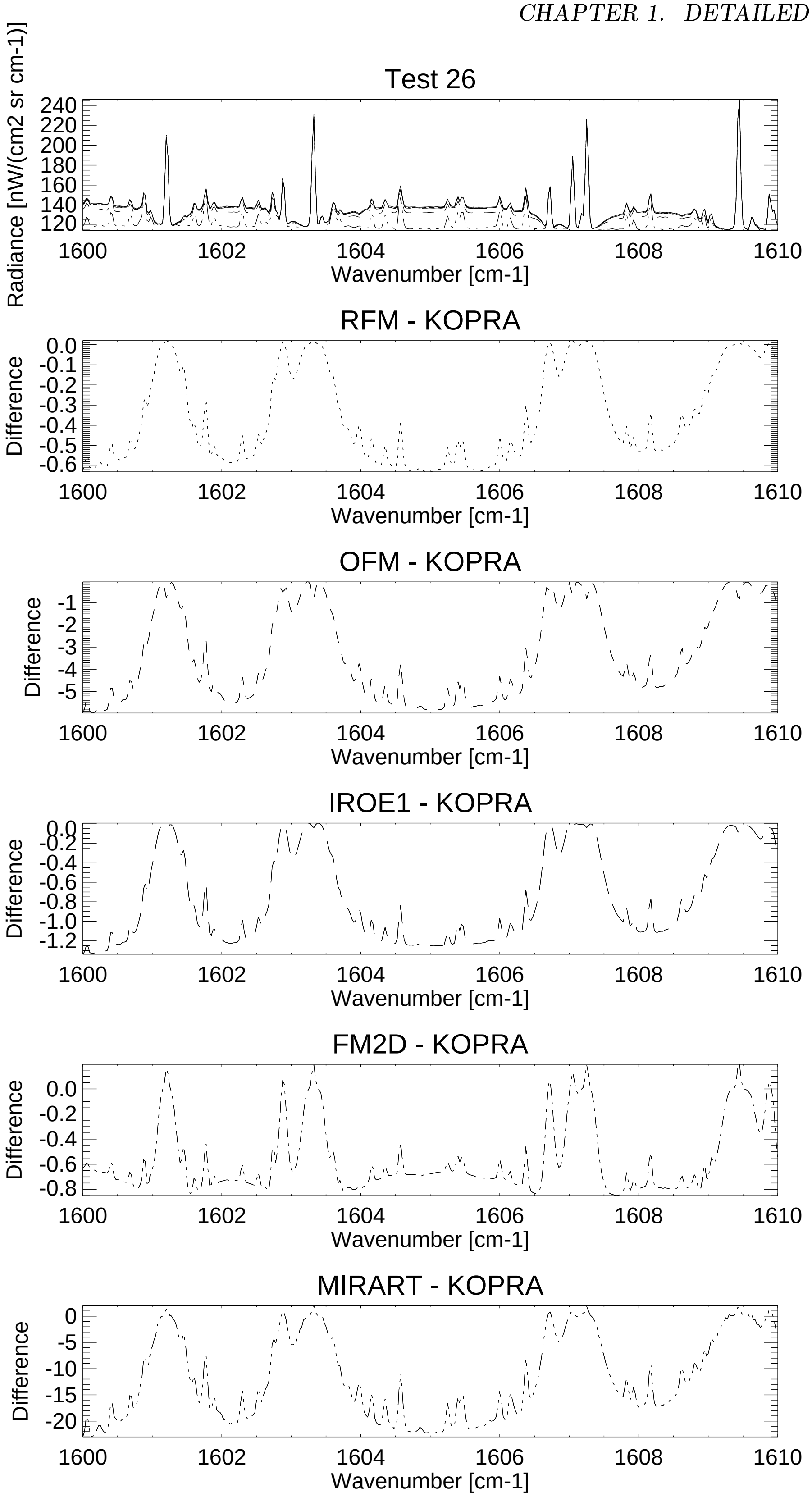

Figure 23: Results of test case 26. The uppermost panel are radiance spectra (KOPRA: solid; RFM: dotted; OFM: dashed; IROE1: long dash; RAL: dashed–dotted; MIRART: dashed doubledotted). The other panels show difference spectra with respect to KOPRA.

The following versions of CKD continua have been used: KOPRA: CKD 2.4; RFM: CKD 2.1; MIRART: CKD 2.2; OFM: CKD 2.1.; FM2D: CKD 2.1. The use of the CKD 2.4 water vapour continuum in the IROE1-code results in improved consistency with the other codes. The remaining discrepancies are attributed to line shape effects as discussed in test cases 1 and 2.

Compared to ITRA exercise, where dramatic differences in calculated radiance spectra were caused by different – or missing – water vapour continuum implementations in the codes under assessment then, there is excellent agreement between all codes now.

Treatment of Inhomogeneous Atmosphere: While the overall agreement of radiance spectra calculated typically was good, the numerical treatment of the inhomogeneous atmosphere proved to deserve major attention (Test cases 18–21): The choice of the altitude grid on which the integration of the radiative transfer equation is performed, as well as the rule for interpolation of volume mixing ratios with altitude (linear versus logarithmic) has visible impact on the radiance spectra. Even for the 15 km tangent height, there was no evidence for differences due to modeling of atmospheric refraction, except for MIRART which did not consider refraction in its version used for this intercomparison experiment.

Field of View Convolution: The numerical integration of the calculated radiance field over the non–infinitesimal field of view of the MIPAS instrument is handled in a different manner in the codes under investigation. Differences refer to both the number of pencil beams used for the numerical integration as well as to the interpolation rules applied to the values of the field of view function and the radiance field.

KOPRA and RFM spectra agree well, both in magnitude and shape (Fig 24); also the shape of residual patterns OFM and FM2D agree well. The number of pencil beams used for convolution of the radiance field with the field of view function is in particular important. KOPRA uses 17, which may be too much for quasi–operational use. RFM uses 14 points. FM2D uses 10 pencil beams, while the OFM uses 3 pencil beams only; this should explain the observed differences. MIRART used 12 pencil beams which, calculated for 35, 36, ..., 45 km tangent altitudes for which the pretabulated FOV function had been provided, thus avoiding interpolation of pencil beam radiances in the tangent altitude space. Additional tests have shown that doubling the number of pencil beams in the FM2D leads to considerably smaller differences.

Some differences are explained by the fact that the FM2D assumes linear variation with elevation of the product field–of–view response times pencil beam radiance, while RFM assumes linear variation of both these quantities, and thus quadratic variation of the product. As expected, these differences become smaller, when more pencil beams are used in the FM2D. The OFM assumes linear variation of the field of view function, while the pencil beam radiance variation with altitude is described by a polynomial of degree number of pencil beams minus one.
All difference spectra are correlated/anticorrelated to the radiance spectrum; this first suggests that differences resulting from different weighting of the pencil beams in the numerical field of view convolution scheme would be responsible for the differences. This, however, could be ruled out for the comparison with RFM spectra by comparing infinitesimal field of view spectra (pencil beam calculations): These differences are in the same order of magnitude as the field of view convolved spectra differences. Instead, the differences in field of view convolved spectra are attributed to the different continuum level.

For OFM and FM2D spectra without field of view the differences are reduced by a factor of 3 and 4, respectively. That means that the largest part of the differences in the test with field of view is due to field of view convolution.

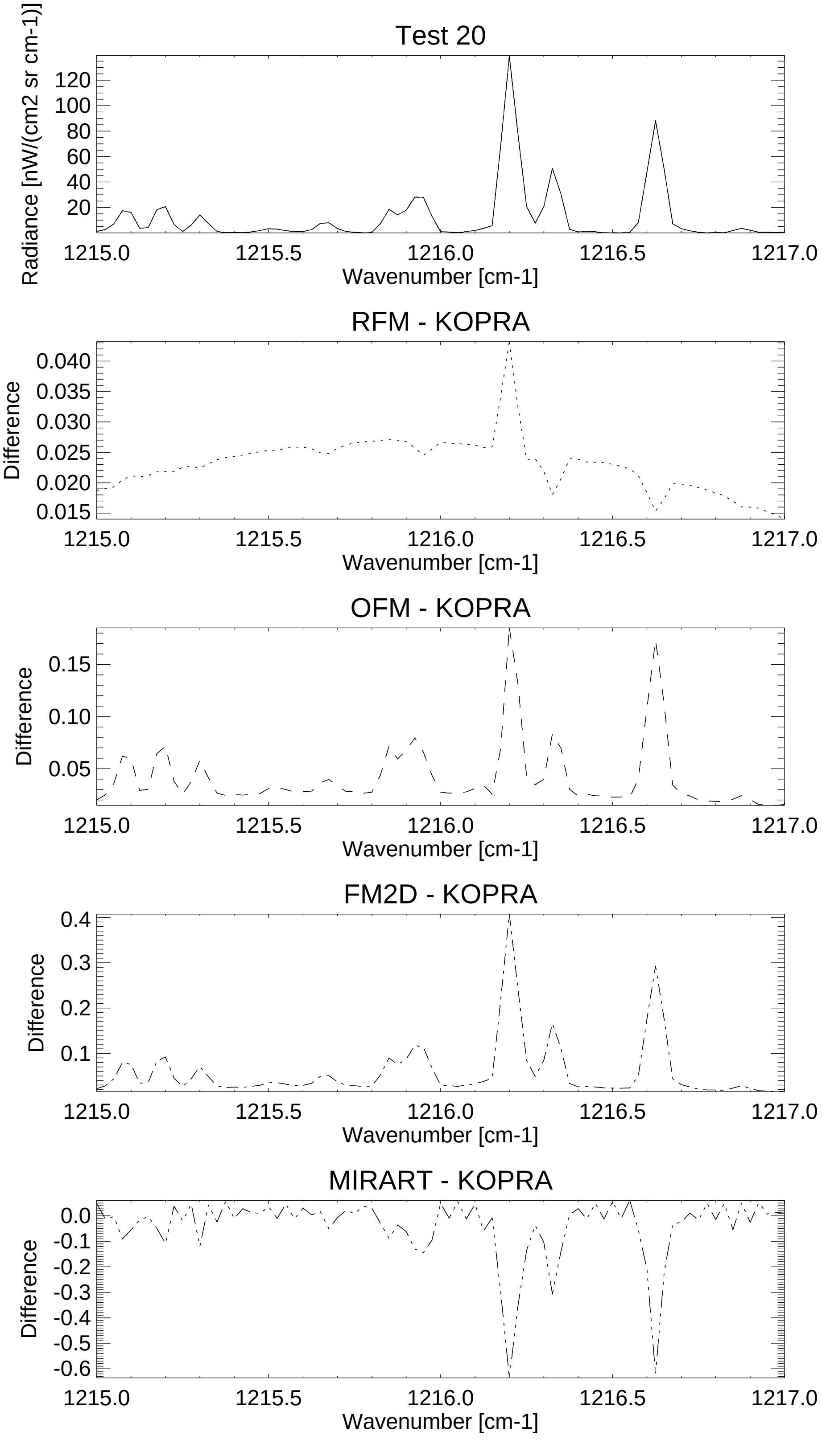

Figure 24: Results of test case 20. The uppermost panel is the KOPRA spectrum (KOPRA: solid; RFM: dotted; OFM: dashed; RAL: dashed–dotted; MIRART: dashed doubledotted). The other panels show difference spectra with respect to KOPRA.

A particular problem with the tabulated field of view used here should be mentioned in conclusion: The ESA-supplied functions are not always tabulated down to zero response, since the field–of–view measurements distributed by ESA did not always cover the entire field of view. Different codes handle this problem in a different manner. The FM2D code sharply cuts off the field–of–view function to zero after the last tabulated data point. The RFM sets zero points one field–of–view grid point space away from the last point. Also the OFM extrapolates the field of view sensitivity smoothly down to zero. Meanwhile the MIPAS field–of–view as measured has been attributed to a non–appropriate measurement setup and thus has been withdrawn.

Absorption Cross–Sections of Heavy Molecules: The spectral features of heavy molecules are not calculated in a line–by–line mode but by interpolation of cross section spectra measured at different pressures and temperatures. In test cases 24 and 25 the CFC-12 band system near 920 cm^{-1} has been chosen to assess the cross section interpolation. Laboratory measurements of these cross sections have been provided by P. Varanasi. These are an extension to the data set described in [62].

Most pronounced residuals between RFM and KOPRA spectra are in the high wavenumber slopes of the Q-branches (Fig. 25). These are even amplified when the instrument field of view is considered. Differences between the OFM and KOPRA spectra are smaller.

Non–Local Thermodynamic Equilibrium: The purpose of test cases 27–30 was assessment of non–local thermodynamic equilibrium (non–LTE) modeling on the basis of precalculated vibrational temperatures. While the microwindow used in test cases 27 and 28 actually lies outside the MIPAS band, the spectral intervals used here have been chosen to allow comparison to a joint activity of the International Radiation Commission (IRC), where further radiative transfer models were investigated for non–LTE conditions [84]. The only codes under investigation here, which support non–LTE, are RFM and KOPRA. As already found during the IRC activities, there is no evidence of non–LTE related discrepancies in radiative transfer modeling between RFM and KOPRA.

Fixing of Radiative Transfer Modeling Problems (WP 3500)

During the calculation of spectra for the intercomparison, and during the intercomparison itself, several shortcomings in the radiative transfer algorithms have been detected, which have been fixed subsequently.

IMK/KOPRA (WP 3510): A problem in KOPRA was discovered and fixed when dealing with test case 10. If the HITRAN parameter for self-broadened halfwith is zero (i.e. unknown) it is now set equal to the air-broadened halfwith (which should never be zero in HITRAN).

Problems with numerical accuracy of field-of-view discretization appeared in the exercises where instrumental field-of-view is taken into account. It became clear that five pencil beams (as originally used) were not enough to get good comparisons with models using higher discretization. Setting this number to 17 solved the problem. This is a change in a parameter of the KOPRA input file and no changes in the program itself were necessary.

For support of bug-fixing in other models various tests were made: different temperatures for cuvette exercises, with/without CO_2-chi-factor, with/without line-mixing and with different line-mixing implementations (Rosenkranz/direct diagonalization).

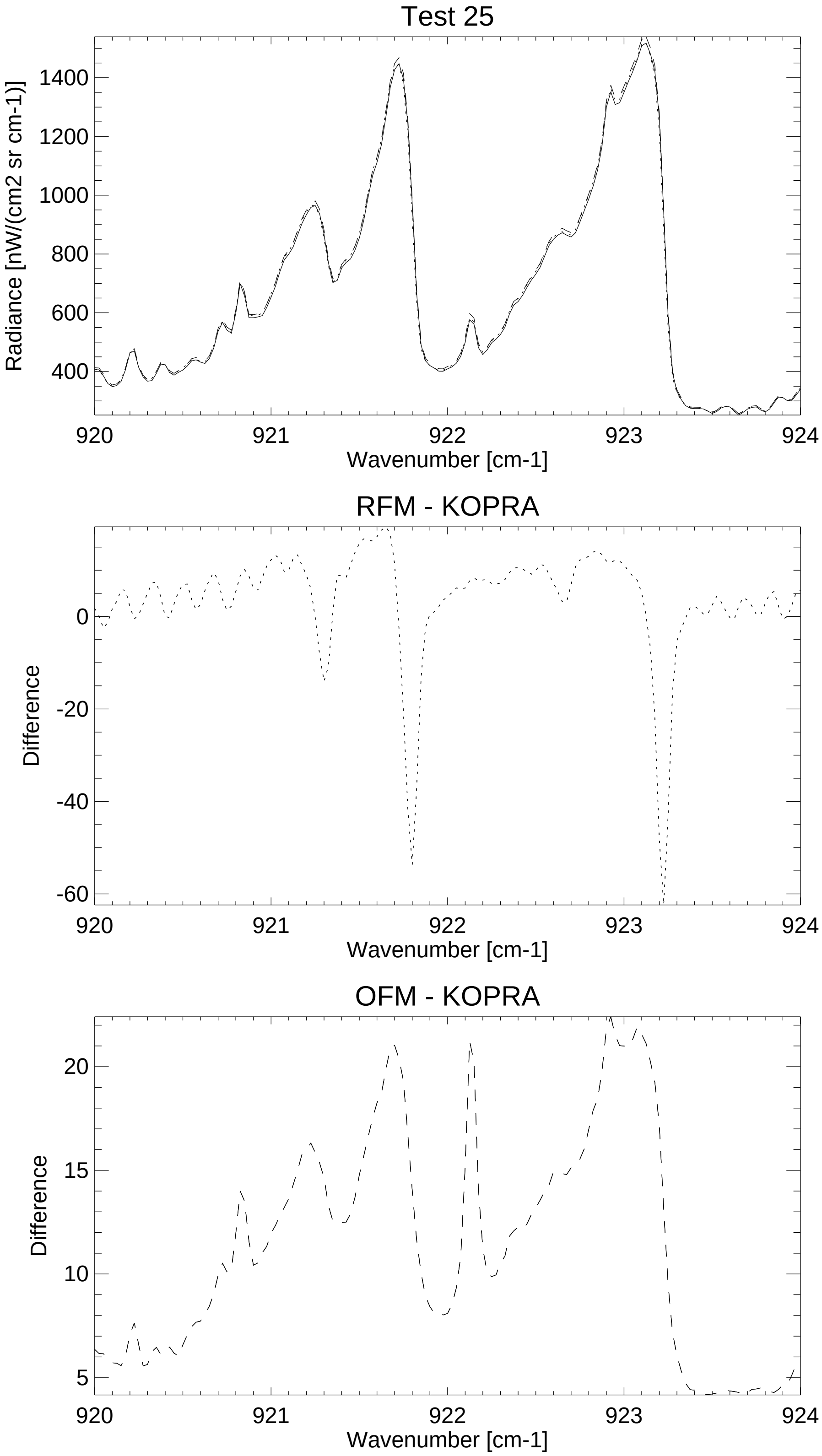

Figure 25: Results of test case 25. The uppermost panel is the KOPRA spectrum, (KOPRA: solid; RFM: dotted; OFM: dashed). The other panels show difference spectra with respect to KOPRA.

Oxford University/RFM (WP 3520): The upgrades of RFM during/in consequence of the intercomparison experiment were only a couple of bug fixes in response to problems occurring with unusual combinations of options.

MIRART/DLR (WP 3530): Initial discrepancies in cases where field-of-view convolution was activated were traced back and finally attributed to a misunderstanding of the sign convention of the asymmetric pretabulated field. This bug could easily be removed. Furthermore, atmospheric refraction of the ray path has been implemented and tested against the FASCODEray tracing algorithm [25].

IROE1/IROE (WP 3540): The intercomparison exercise carried-out in the frame of this study highlighted the fact that some assumptions adopted in the IROE2 model have significant impact in the simulation of some spectral regions covered by MIPAS. Therefore, since some of these assumptions are relatively easy to avoid, the IROE2 model has been upgraded (the upgraded processor is named IROE1) to include: pressure-shift, self-broadening, and CO_2 Q-branch line-mixing. In particular, CO_2 Q-branch line-mixing has been implemented using the approach of Hartmann and the calculation can be done exploiting either the full relaxation operator or the first order approximation (less time consuming). In addition to the above effects, compared to IROE2, the IROE1 forward model includes also a more recent model for water-vapor continuum emission (CKD v. 2.4) and a functionality that allows to include in the calculations the emission of heavy molecules (e.g. N_2O_5, $ClONO_2$, CFCs etc.) that is characterized by broad spectral features simulated by means of pre-tabulated absorption cross-sections.

RAL/FM2D (WP 3550): No further issues or improvements were required.

1.3.3 Blind Test Retrieval Experiment (WP 4000)

The purpose of the blind test retrieval experiment was to prove that the participants' codes successfully can retrieve temperature and volume mixing ratios of species from spectra as expected from the MIPAS measurement. This test was intended rather as a test under realistic conditions than a mere sensitivity study. For this reason, the participants were provided with limited amount of information, which was: time and location of the measurement, nominal measurement geometry, and MIPAS instrument specification. All other data, such as pressure temperature model, abundances of species, vibrational temperatures, exact measurement geometry were not known to the participants. This rigorous strategy was decided to guarantee realistic conditions.

There were a few exceptions to the rigorous test conditions: A separate test case has been defined where pressure and temperature profiles as well as line-of-sight information were provided to the participants. This was to make participation possible also for groups which plan not to retrieve these quantities but to rely on the operational ESA data product. Furthermore the following sources of error have been neglected throughout the blind test retrieval experiment: Instrument line shape errors, horizontal gradients of state parameters, scattering.

While the final goal of the participants is to retrieve data beyond the operational ESA data product, this retrieval experiment focuses on the key species, since

- Key species retrievals are a good exemple to demonstrate the capability of a retrieval processor. Only if the easier key species retrievals are understood, the non-key species retrievals will be reliable.

- Key species can be treated by all groups, while handling of further species often need more sophisticated retrieval approaches (e.g. consideration of non-local thermodynamic equilibrium). In this sense retrievals of key species are better intercomparable among the groups.

- To improve the data quality of key species beyond the quality of the operational ESA data products is a further goal in itself.

Generation of Test Data (WP 4100)

Generation of Reference Data: In a first step, pressure, temperature, and and volume mixing ratio profiles have been compiled for a polar summer scenario (80^o N latitude, 12.00 h local time, 70^o solar zenith angle) from the ground up to 200 km altitude. In order to guarantee self-consistency of the partitioning of chemically active species, volume mixing ratios have been preferably taken from chemical transport models (see Table 8). Volume mixing ratio profiles for species other than NO, O, O_2, and N above 112 km [71, 69] or 120 km (MIPAS reference atmospheres have been extrapolated to reasonable values. A structured temperature profile has been simulated by pertubation of the original profile with a wave structure below 100 km. Pressure has been calculated hydrostatically. In a second step, vibrational temperatures of CO_2, H_2O, O_3, NO, NO_2, N_2O, HNO_3, CO, OH, and CH_4 have been calculated for the previously defined atmospheric conditions. Several improvements with respect to previous calculations of NLTE populations have been made. (see the Report on the vibrational temperatures climatology, deliverable D7) In general, the chemical and hydrostatic consistence of the atmospheric input data as well as the line-by-line calculation of tropospheric upwelling fluxes lead to more realistic vibrational temperatures. In particular, new NLTE models for OH, NO, N_2O and O_3 have been used and improvements of kinetic rates have been included for the other molecules.

Table 8: Volume mixing ratio sources used.

Data source	Month	Latitude	Atmospheric parameter
2D CTM [71, 69]	July	79N	temperature and all gases available from model below 112 km
MSIS high solar activity (F10.7 = 200, AP = 10) [70]	May	85N	N, O_2, and O $>$ 112 km
2D CTM Gerard&Roble solar cycle maximum [68]	June	80N	NO $>$ 120 km
MIPAS reference atmosphere complilation, J.J. Remedios	April	80N	CO_2 $<$ 120 km
US standard atmosphere 1976 USSTANDARD			some minor constituents

Generation of spectral data: Two different sets of spectral data covering all MIPAS channels have been generated. The first set (BT1) has been calculated for the tangent height of the nominal observation scenario while for the second set (BT2) these tangent heights have been perturbed within the expected pointing error (absolute error: -663 m, $1\!-\!\sigma$ relative error: 136 m) of MIPAS. The resulting tangent altitudes for BT1 and BT2 are summarised in Table 9.

All spectral data has been calculated with the KOPRA forward model. The following gases have been included for line by line calculation: H_2O, CO_2, O_3, N_2O, CO, CH_4, O_2, NO, SO_2, NO_2, NH_3, HNO_3, OH, HF, HCl, HBr, ClO, OCS, H_2CO, HOCl, N_2, HCN, CH_3Cl, H_2O_2, C_2H_2, C_2H_6, COF_2, HO_2. The following cross section gases have been included: CFC-11 (CCl_3F), CFC-12 (CCl_2F_2),

Table 9: Used tangent heights (km).

BT1	6.00	9.00	12.00	15.00	18.00	21.00	24.00	27.00	30.00
	33.00	36.00	39.00	42.00	47.00	52.00	60.00	68.00	
BT2	5.09	8.13	11.19	14.26	17.32	20.39	23.46	26.52	29.56
	32.60	35.51	38.37	41.34	46.31	51.25	59.29	67.32	

CFC-22 ($CHClF_2$), SF_6, CFC-14 (CF_4), CCl_4, CFC13 (CCl_2FCCl_2), CFC-114 ($CClF_2CClF_2$), N_2O_5, $ClONO_2$.
Spectral data has been mainly taken from HITRAN2000. Updates from the HITRAN web-page have been considered for CH_4, O_2, and C_2H_2. H_2O, O_3, HNO_3, and HOCl line data have been taken from the IROE HITRAN96 update. An updated version of NO_2 lines (see Section 1.3.1) has been used. Cross section data has been taken from HITRAN2000.
CO_2 Q branch line mixing has been calculated with the direct diagonalisation method using line mixing data from Hartmann et al. [47]. Gas continua for N_2, O_2, CO_2 and H_2O have been included. A volcanic aerosol continuum has been calculated with the internal Mie model using a Pinatubo aerosol size distribution [85] reduced by a factor of two in order to account for polar conditions and H_2SO_4 refraction indices from Tisdale et al. [86]. NLTE has been considered for CO_2 (112 bands), H_2O (11 bands), O_3 (224 bands), NO (12 bands), NO_2 (6 bands), N_2O (53 bands), HNO_3 (7 bands), CO (1 band), OH (63 bands), and CH_4 (13 bands).
A trapezium shape field-of-view (1.22 mrad base, 0.854 mrad top) has been applied using a discretisation of 7 pencil beams. The instrumental lineshape used in the generation of blind test spectra is identical to that used in the forward model intercomparison. Noise has been added to the spectra according to the NESR values summarised in Table 10. Finally, an altitude independent instrumental offset (see Table 10), which varies smoothly with frequency, has been applied to the generated spectra.

Table 10: Instrumental noise (unapodised) and offset (1-σ-deviation) for each channel

Channel	NESR (nW/(cm^2 sr cm^{-1})	Offset (nW/(cm^2 sr cm^{-1})
A	30.0	100.0
AB	17.0	80.0
B	12.0	40.0
C	4.0	12.0
D	4.0	8.4

Blind Test Retrievals (WP 4200)

The blind test data were distributed among the participants. All participating groups calculated retrievals based on their own microwindow selection, without consideration of non-LTE (for this retrieval experiment only), and using the choice of processing parameters they intend to use when applying the processors to real MIPAS data. The detail choice of processing parameters were the following:

IMK choice of processing parameters: The IMK retrieval code (using KOPRA forward model) was used to perform retrievals from the blind test spectra. The following inputs and set-up options were used:

- Simultaneous multi-microwindow inversion.
- Regularization with Tikhonov-type first order differences operator for temperature and abundancies. Optimal estimation for line of sight according to specified line of sight uncertainties.

- Microwindows selected from the IMK MW database, for retrievals over the full 6-68 retrieval range (30 microwindows per target parameter, spectral masks to exclude points which degrade the retrieval).
- Line-by-line calculation of absorption coefficients.
- Retrieval vector: absolute tangent altitude; T and vmr on a fixed 1-km grid (above 44 km 2-km grid, above 70 km 5-km grid); hydrostatical p adjustment; continuum up to 32 km, microwindow-dependent but subject to "clustering" (i.e. one continuum value for several tiny microwindows within a 5 cm^{-1} interval and smoothness constraint in the wavenumber domain; offset constant with altitude but microwindow-dependent.
- HITRAN98 spectroscopic data.
- CO_2 line mixing not activated in KOPRA.
- H2O continuum included in FM calculations.
- Non-LTE not activated in KOPRA.
- FOV represented by 5 points for tangent altitudes below 15 km, 3 points above.
- Constituent retrievals performed in sequence (except joint fit for CH_4 and N_2O).

Oxford University choice of processing parameters: The OPTIMO retrieval code (using RFM forward model) was used to perform retrievals from the blind test spectra. The following inputs and set-up options were used:

- sequential inclusion of microwindows, iterating over each microwindow in turn until convergence was reached.
- Optimal estimation, using a priori atmospheric profiles and covariance (with interlevel correlations) to constrain retrieval.
- Microwindows selected from the ESA MW database, for retrievals over the full 6-68 retrieval range (4-10 microwindows per target parameter, spectral masks to exclude points which degrade the retrieval).
- Look-up tables (LUTs) for absorption coefficients and irregular spectral grids
- Retrieval vector: ln(p) and T at tangent points or ln(VMR) at tangent points, plus continuum up to 30 km and radiometric offset (both microwindow dependent). The p,T retrieval treats the lowest tangent point as fixed at 6 km and calculates the remaining tangent point altitudes using the hydrostatic equation.
- Pointing knowledge included in pressure, temperature a priori covariance matrix.
- HITRAN-MIPAS spectroscopic data.
- CO_2 lineshape included in LUTs, line mixing not included in LUTs.
- H2O continuum included in FM calculations by default, non-LTE not included.
- Atmospheric layering: MIPAS measurement grid.
- FOV represented by 5 points, 1.5 km spacing.
- Constituent retrievals performed in parallel, i.e. climatological profiles assumed for all contaminants.

DLR-a choice of processing parameters: The atmospheric state vector to be retrieved is a discrete representation of the volume mixing ratio of the sought molecule, an altitude dependant empirical continuum (using the same discretization), and a constant baseline correction. Pressure, temperature as well as other gases were assumed to be known.

DLR-b choice of processing parameters: The parameters selected by DLR originated from a series of tests and optimisation attempts. In essence, the most important parameters are:

- sequential retrieval of all species;
- use of multiple microwindows for each species to be retrieved;
- use of microwindows from existing databases to allow comparisons with previous test retrievals aimed at a quantitative determination of physical effects;
- retrieval of vertical profiles of species, height constant offsets per microwindow, and height-dependent aerosol continua per microwindow (below 30 km) on the measurement grid;
- line by line calculation of of absorption coefficients with adaptive determination of atmospheric layering (as provided by the KOPRA forward model);
- regularized inversion using a bias-free version of optimal estimation with dedicated constraint levels for each species to be retrieved;
- use of HITRAN spectroscopic data with improvements provided by partner institutions;
- precise FOV modelling;
- line mixing enabled, NLTE handling disabled;

IROE choice of processing parameters: Blind–test retrievals were carried-out using the following setup:

- The retrieval code was operated in the IROE2 configuration (i.e. no instrumental parameters were retrieved together with target parameters)
- Retrieved species: limited to MIPAS key species (pressure, temperature, H_2O, O_3, HNO_3, CH_4, N_2O, NO_2).
- Retrievals were carried-out using the spectral intervals (microwindows) selected by the Oxford University team for near real-time retrieval of key species (July 01 version).
- Only used a-priori information: engineering information on pointing. Covariance data generated using a dedicated tool that simulates MIPAS pointing system performance.
- Spectroscopic database: HITRAN_MIPAS_PF2.0 (MIPAS-specific compilation basedon the HITRAN database and upgraded in the frame of a joint effort of IROE and LPM.
- Initial guess atmosphere: climatological profiles corresponding to 80^o N latitude. BT2 retrievals: VMR retrievals were operated using retrieved pressure and emperature.
- Global fit: the full set of observations relating to a limb-scanning sequence is simultaneously fitted (multi-MW and multi-altitude fit)
- Method: Nonlinear least squares fit using Levenberg - Marquardt
- Regularization: switched OFF
- Retrieval state vector

1. PT retrieval:
   - Tangent pressure
   - Temperature at tangent pressure
   - Atmospheric continuum: one profile for each MW, up to 36 km plus linearity constraint within 10 cm^-1
   - Instrumental offset: one parameter for each MW, tangent height-independent
2. VMR retrievals:
   - VMR at tangent pressure
   - Atmospheric continuum: one profile for each MW, up to 36 km + linearity constraint within 10 cm^-1
   - Instrumental offset: one parameter for each MW, tangent height-independent

   Note: the altitude scale of the output profiles is reconstructed using hydrostatic equilibrium (the lowest tangent altitude is assumed as known). Therefore retrieved profiles may suffer of a vertical shift if they are represented as a function of altitude.

- Retrieval altitude range: established in the frame of the procedure for selection of optimized occupation matrices (microwindows / altitudes, done at Oxford University)
- Sequence of retrievals: simultaneous retrieval of P and T plus sequential retrieval of the key species (H_2O, O_3, HNO_3, CH_4, N_2O, NO_2). The order of VMR retrievals is chosen so that the reciprocal interference of the species is minimized.

RAL choice of processing parameters: The RAL team's primary interest is in retrieval of O_3 and H_2O in the UTLS region. The intention make use of the operational temperature and pressure retrievals and therefore the retrieval processor was only applied to blind test 1 (BT1) measurements with correct pressure and temperature information.
Setting up the processor includes forward and retrieval model configuration as well as selection of appropriate microwindows.

- Forward model configuration

  The FM2D forward model was used with the following set-ups:
  - optimised, irregular frequency grid
  - variable atmospheric layering from 3 to 5 km
  - pre-calculated absorption coefficients using the HITRAN 1998 data base
- Microwindow selection

  The RAL microwindow selection scheme ranks microwindows for the chosen primary targets (in this case O_3 and H_2O). It is based on selection of 1 cm^{-1} microwindows for all altitudes and uses pre-calculated $K^T S_y^{-1} K$ matrices.
- Retrieval model configuration

  The retrieval model used for this work is a flexible scheme that allows joint retrieval of multiple atmospheric species as well as instrument parameters.

  The current configuration is as follows:
  - profiles of O_3 and H_2O as primary targets
  - use of the 10 "best" microwindows for the primary targets as indicated by the selection scheme
  - CO_2, N_2O, CH_4, NO_2, HNO_3 also included in state vector to accommodate spectral modelling errors

- 2 continuum coefficient profiles per microwindow
- 1 altitude independent offset per microwindow
- spectral contaminants : CH_3Cl, NH_3, HCN, C_2H_2

Intercomparison of Results (WP 4300)

The general shape of the profiles is retrieved well, as well as the absolute values of prominent points of the profile (minima, maxima). Some minor residuel features (overshooting or smoothing in the vincinity of minima/maxima or in the domain of extreme altitude gradients are explained as responses of the retrieval systems to finite sampling along with regularization. For source gases (CH_4 and N_2O) their occur problems near/below the tropopause region. Here saturation of spectra makes Jacobians small and thus retrieval difficult. The good matching of IMK retrieved profiles of stratospheric species (e.g. O_3 and HNO_3) and reference profiles at extreme high or low altitudes is obtained at the cost of a large number of microwindows. Thus, it reflects rather the particular processor setup rather than the general functionality of the processor. It shows that there is room for improvements beyond the operational data product if there are enough computer resources available.

The specification of line of sight retrieval is quite different for the IMK, Oxford and IROE codes. IMK attemps to retrieve both absolute and relative tangent altitudes but depends on a priori knowledge of a reference point where altitude and pressure are known. This point is used to build up a hydrostatic atmosphere. In spite of a bad temperature/pressure a priori profile, the knowledge of the absolte line of sight information is improved by a factor of two with respect to the a priori line of sight information. As for line-of-sight and temperature retrievals, the DLR-b processor follows an approach similar to the IMK processor, where a reference point at a given altitude is used to obtain absolute tangent point altitudes.

The Oxford algorithm retrieves the relative tangent altitudes (differences between adjacent tangent altitudes) quite reliably: the differences between retrieved and true tangent altitudes are quite independent from the absolute altitude.

The IROE code retrieves tangent pressures and derives, through hydrostatic equilibrium, also an estimate of tangent altitude increments. Therefore, if a tangent altitude is assumed as known (e.g. the lowest of the scan) it is possible to reconstruct the overall altitude scale of the retrieved profiles. However, the adopted approach does not attempt to correct for possible tangent altitude offsets (common to the whole scan sequence) and therefore retrieved profiles may turn-out to be affected by a vertical offset whenever represented as a function of altitude. This is not surprising because the independent variable in the IROE retrievals is pressure and hence the retrieved parameters can be represented correctly only in the pressure domain (see results of BT retrievals reported in document D42, deliverable of the present study).

The overall conclusion is that most of the processors work as defined even in ths test which is assumed to be close to reality. This experiment can be seen as successful "readyness for real data test".

Fixing of Problems (WP 4400)

IMK (WP 4410): All in all, the Karlsruhe processor performed well in the blind test retrieval experiment. Two actions were taken to improve the performance: First, a tool has been generated which allows regularization of continuum profiles not only in the altitude domain, but also in the wavenumber domain. While from a mathematical point of view this seems to be quite an ad hoc decision, from a physical point of view this certainly is reasonable, since whatever causes the radiance continuum has quite a low wavenumber-dependence, which justifies a smoothing constraint of

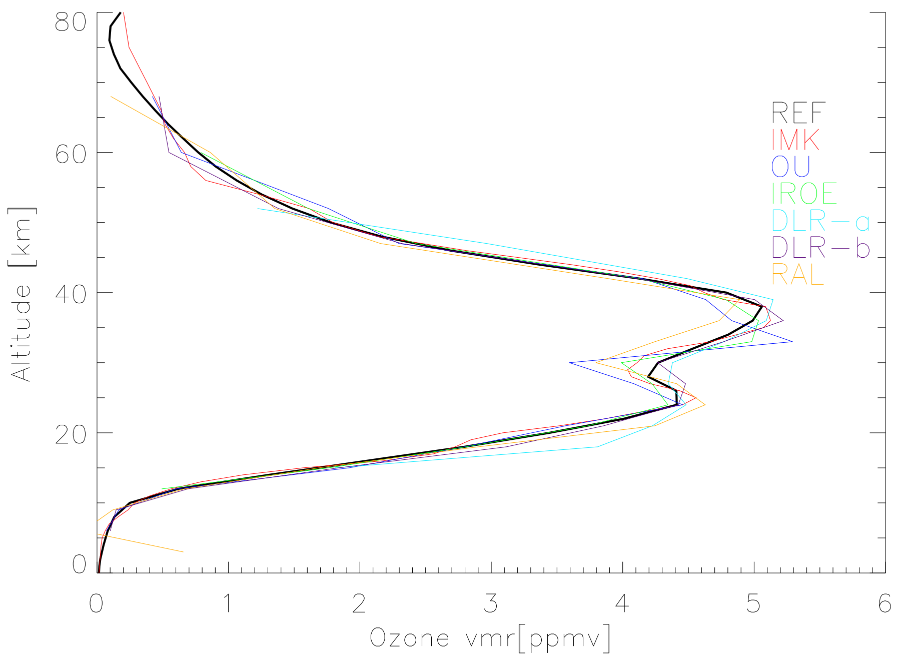

Figure 26: Results of blind test retrieval experiment with given line of sight and temperature information.

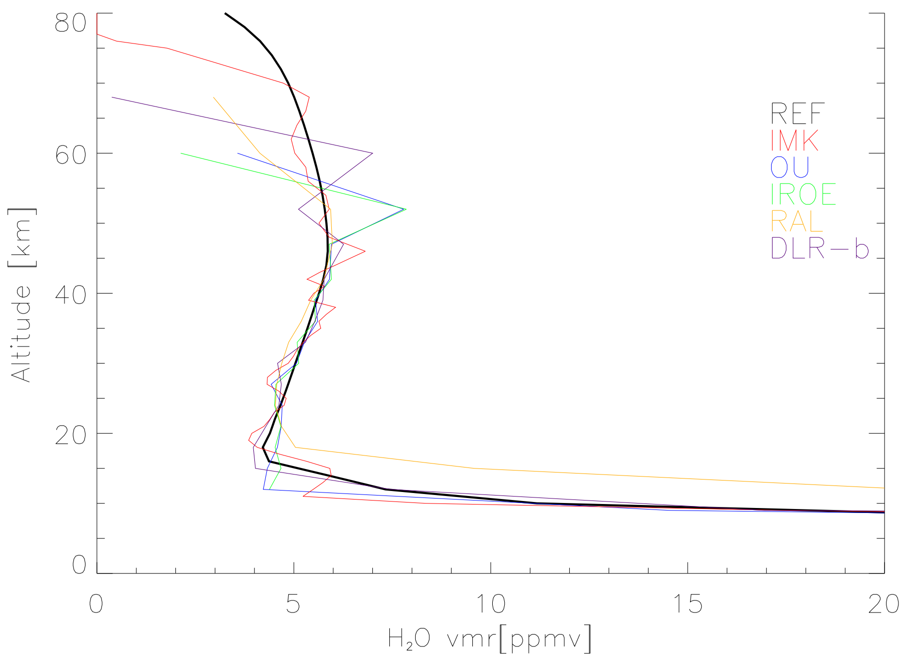

Figure 27: Results of blind test retrieval experiment with given line of sight and temperature information.

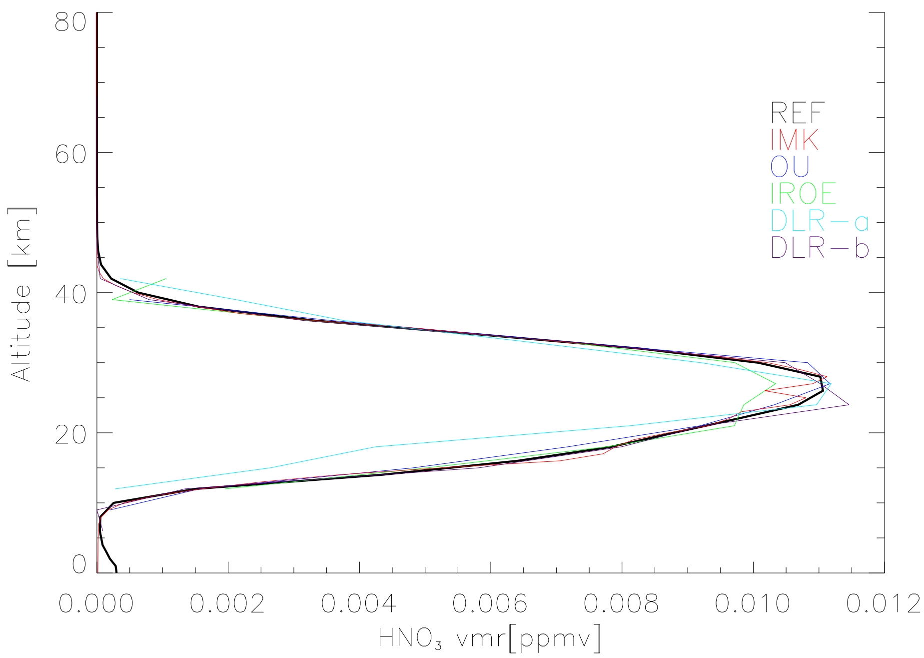

Figure 28: Results of blind test retrieval experiment with given line of sight and temperature information.

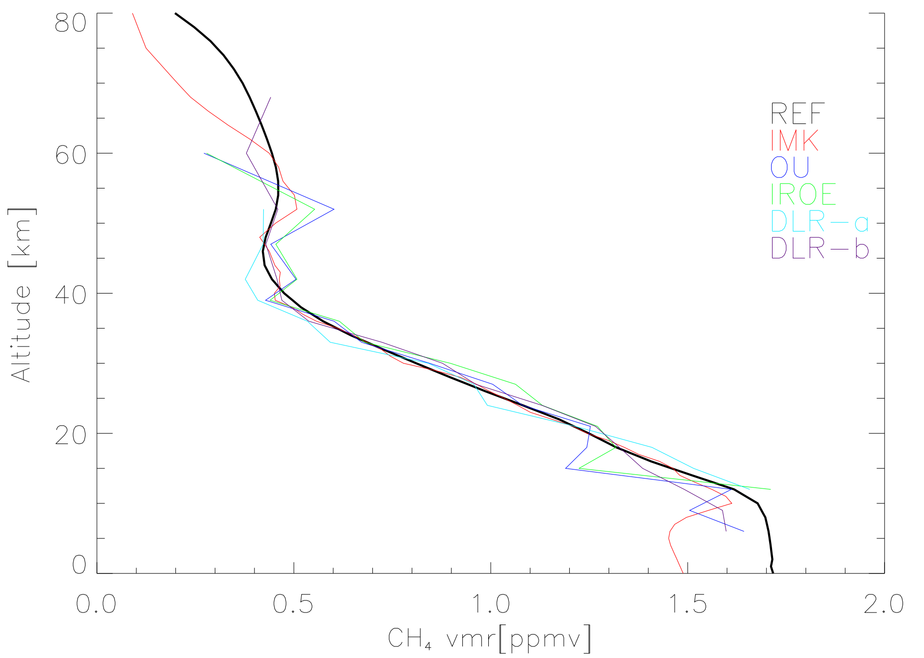

Figure 29: Results of blind test retrieval experiment with given line of sight and temperature information.

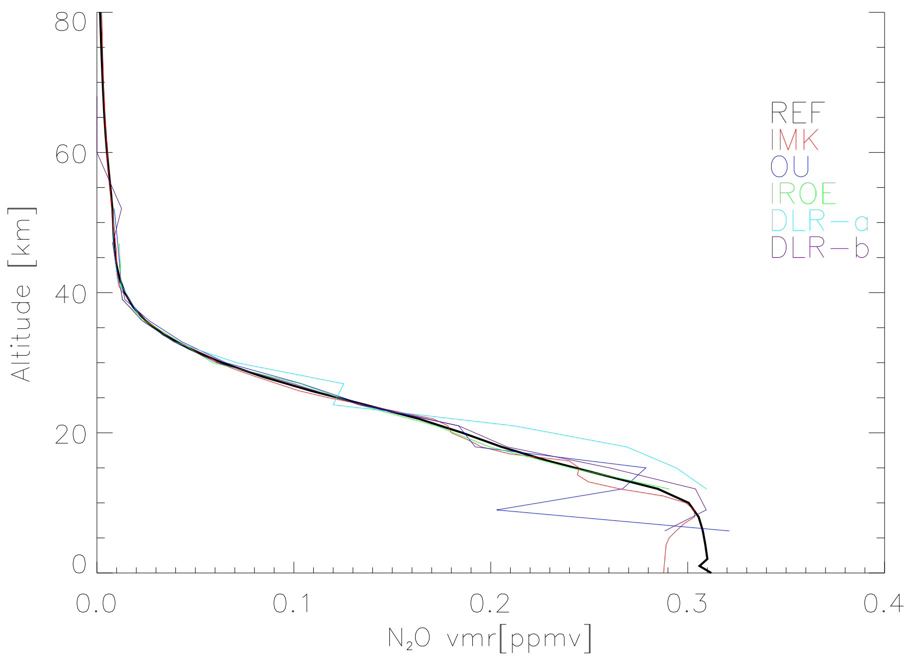

Figure 30: Results of blind test retrieval experiment with given line of sight and temperature information.

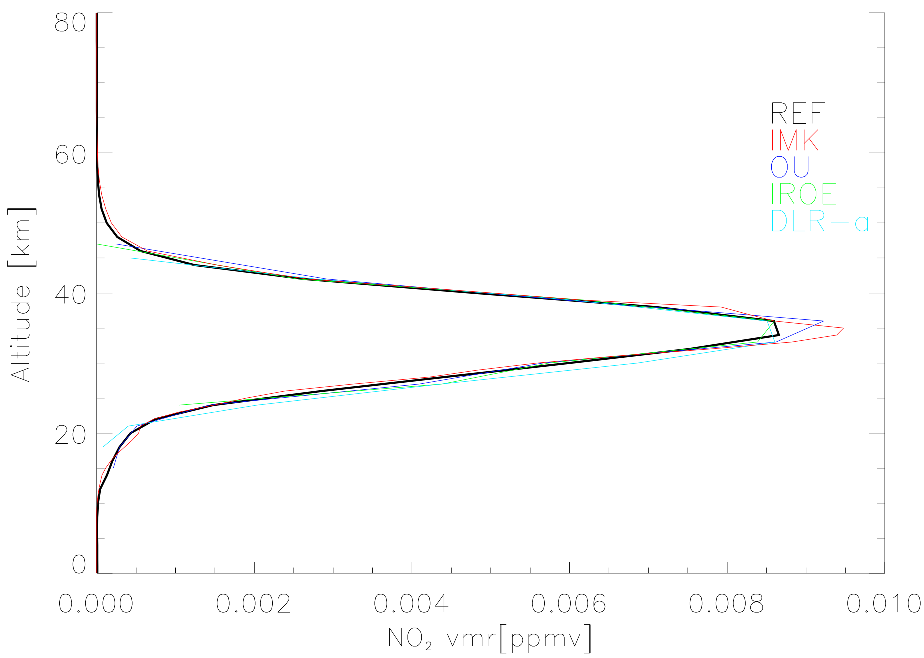

Figure 31: Results of blind test retrieval experiment with given line of sight and temperature information.

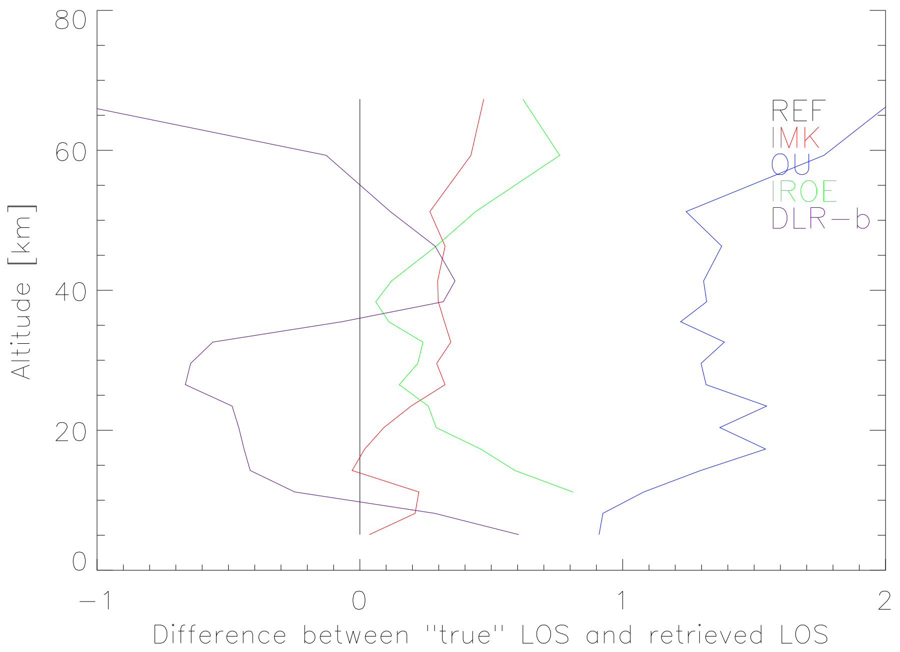

Figure 32: Results of blind test line of sight retrieval experiment.

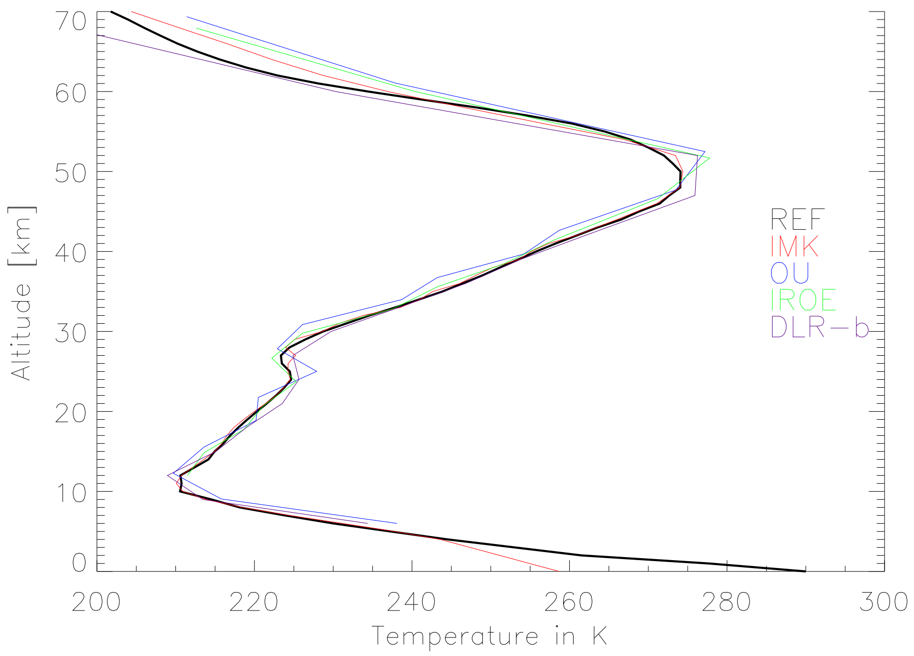

Figure 33: Results of blind test temperature retrieval experiment.

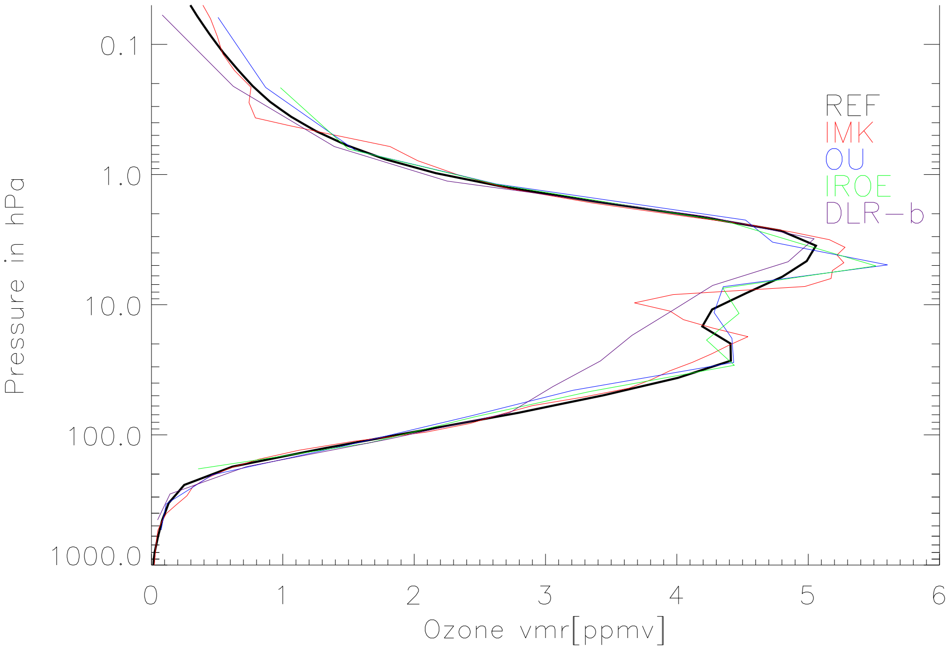

Figure 34: Results of blind test retrieval experiment on the basis of retrieved line of sight information and temperature.

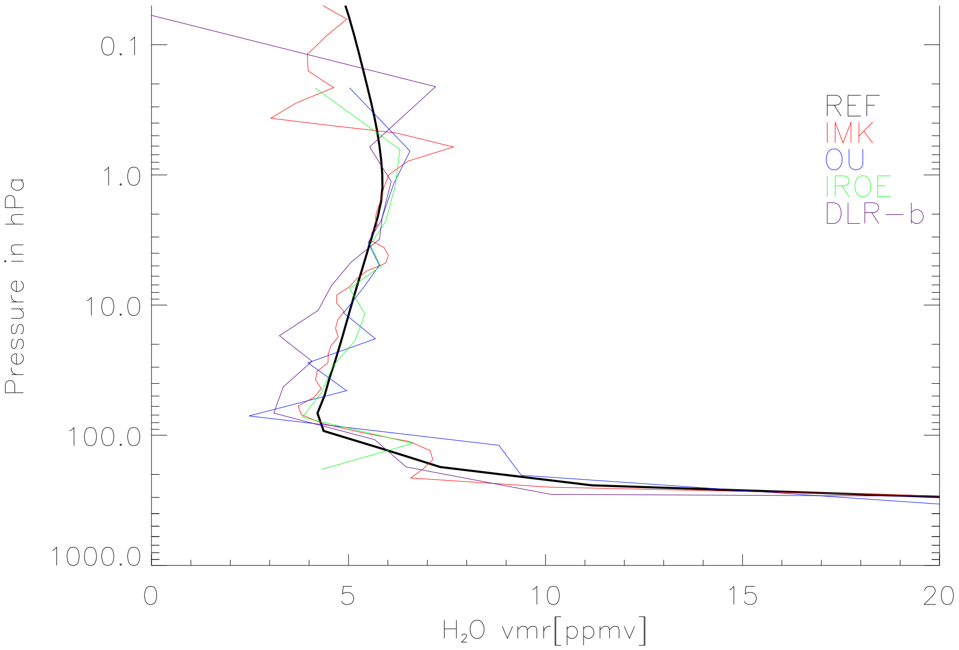

Figure 35: Results of blind test retrieval experiment on the basis of retrieved line of sight information and temperature.

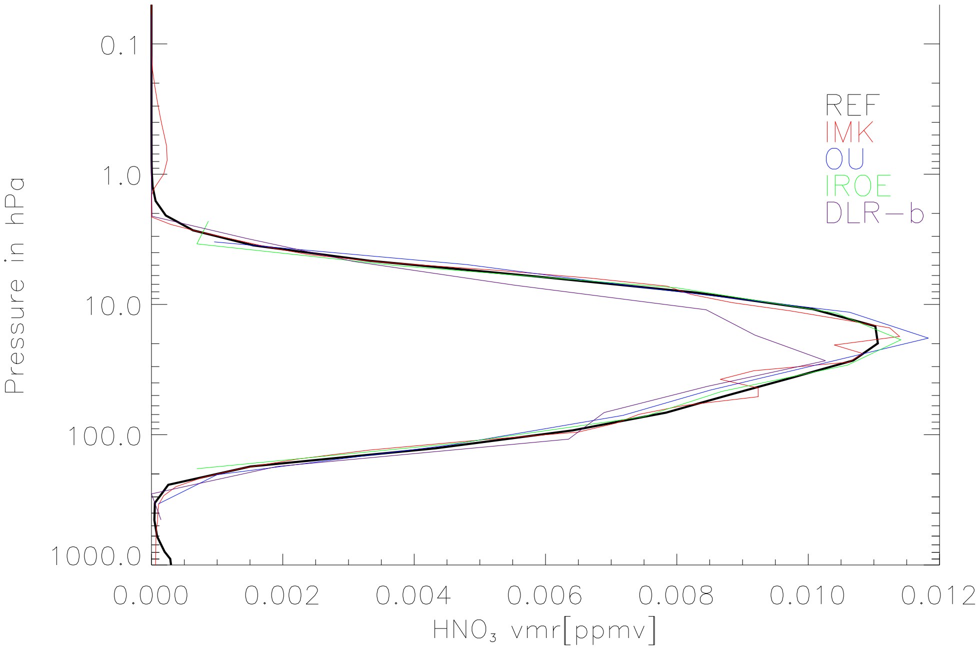

Figure 36: Results of blind test retrieval experiment on the basis of retrieved line of sight information and temperature.

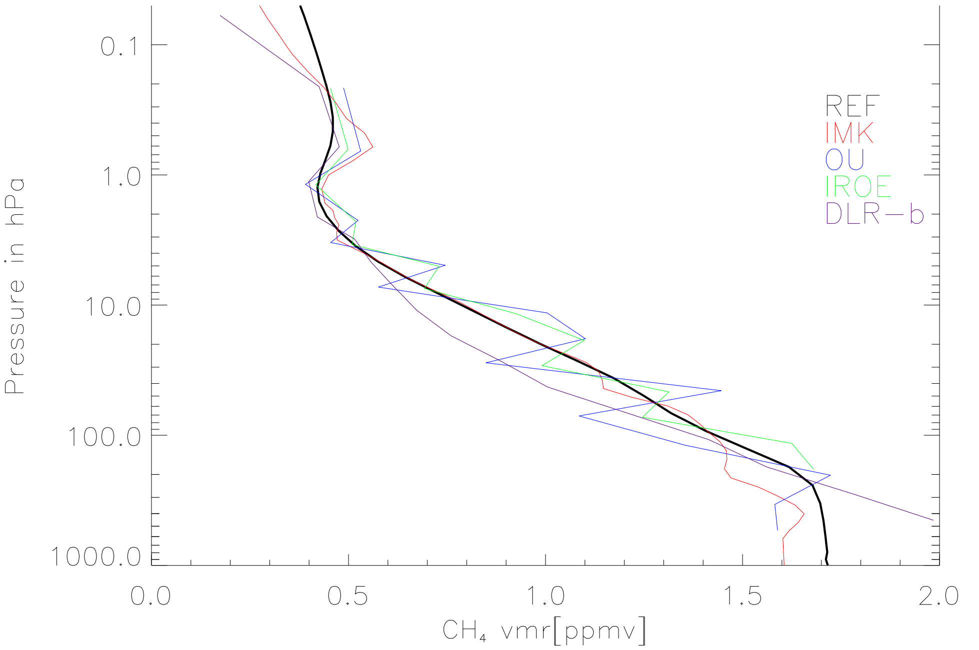

Figure 37: Results of blind test retrieval experiment on the basis of retrieved line of sight information and temperature.

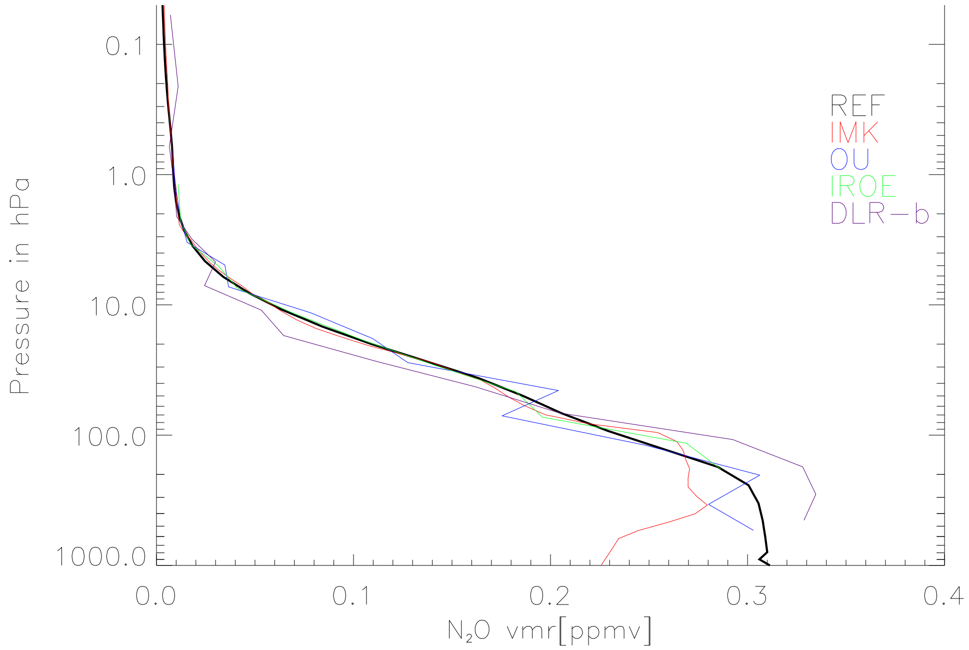

Figure 38: Results of blind test retrieval experiment on the basis of retrieved line of sight information and temperature.

continuum with wavenumber. This regularization approach led to better retrievals in cases when a microwindow was used only at lower altitudes. The profile shape of the continuum related to this microwindow first could not be retrieved for altitudes above the highest tangent altitude. Using the new regularization approach, the information on the profile shape comes from adjacent microwindows. This strategy avoids error propagation through unrealistic continuum profiles above the uppermost tangent altitude where the microwindow is used to the retrieval of target state parameters at lower altitudes.

Another change in strategy has been to retrieve NO_2 and CH_4 simultaneously in a joint fit approach rather than one after the other. This does not only improve the result, but also reduces the number of microwindows needed, and thus also computational effort, since for the joint fit a smaller number of microwindows is required to obtain the same accuracy than for each single fit.

Oxford University (WP 4420): Retrievals were run using different options in the OPTIMO processor and results intercompared. In most cases no significant differences were found, leading to the following conclusions:

- look-up tables and irregular grids work well (cf line by line calculations and full spectral grid)
- different contaminant profiles have little effect on retrieved profiles.

The initial intercomparison with other groups showed that the BT2 constituent profiles were slightly shifted in altitude, and that the retrieved pointing profile was quite far from the true values. Subsequently, some problems have been fixed and improvements have been made to the retrieval code:

- An error in pointing values used in BT2 constituent retrievals was removed;
- The p,T retrieval was improved by accounting for hydrostatic equilibrium in the calculation of pressure Jacobians (enables more stable convergence), and using a more sophisticated a priori covariance matrix, which includes both atmospheric and pointing uncertainties, and a hydrostatic constraint.
- Including one or more additional points above the state vector in the retrieval leads to more realistic profiles, as the effect of the initial guess profile outside the retrieval range is reduced.
- . The code has been made more flexible (user specifies retrieval set-up) and faster.

Differences remaining between Oxford retrieved profiles and true profiles are thought to be caused by:

1. degraded resolution of retrieval cf 'true' profiles;
2. correlations in a priori covariance matrix, causing the profile to follow the shape of the a priori profile somewhat;
3. initial guess profile very different from true profile (so profile very different from truth outside retrieval range).

DLR-a (WP 4430a): The main upgrades of this new retrieval code were the implementation of an altitude dependant continuum fit and the use of better microwindows. (However, it is not planned to use a sophisticated microwindow scheme and occupation matrix approach similar to the operational MIPAS Level 2 processors.)

Table 11: Spectral region, altitude range, and method used by DLR–a retrieval code in BT1.

gas	μ–window	z–grid	method	reg. matrix
O_3	715–717	15–52	IRGN	Sobolev 0.25, 0.0, 0.75
NO_2	1600.50–1601.40	18–45	IRGN, bounds	2. deriv. matrix
N_2O	1270.825–1272.025	12–52	IRGN, bounds	diag. weighted matrix
HNO_3	870.65–871.35	12–42	IRGN	identity matrix
CH_4	1355.15–1356.75	12–52	IRGN	diag. weighted matrix

DLR-b (WP 4430a): Some late changes and extensions of the retrieval code intended to provide additional features like logarithmic fitting, exclusion of selected microwindows during continuum retrievals, and improved run-time performance led to some hitherto undiscovered side effects during the AMIL2DA retrieval tests and necessitated immediate code modifications following the mid-term meeting. This included some tables used for data input, species specific regularisation, and the selction of ILS parameters. As a result, the results have been improved considerably compared to previous profiles.

IROE (WP 4440): In general the observed discrepancies between IROE retrieved and 'true' profiles are consistent with the estimated total error of the retrieved profiles. However there are a few exceptions to this general rule and we discuss here about the origin of the relatively large discrepancies observed in these few cases. In the retrieval algorithm the topmost and the lowermost retrieved profile points are used to scale the initial guess profiles outside the retrieval altitude range, so that the initial guess profile turns out to be smoothly connected with the retrieved profile at the edges of the retrieval range. This approach implies that if the assumed shape of the initial guess profile outside the retrieval range is different from the shape of the real profile, the topmost and the lowermost retrieved points are affected by an extra error due to the fact that the fit tries to compensate for the different shape of retrieved and initial guess profiles outside the retrieval range using the extreme retrieved points. So far the Oxford tool evaluating the total error budget does not account for this type of error which, therefore, may show-up as an unpredicted discrepancy in our results. For this reason we also repeated the BT2 retrievals using as initial guess the 'true' profiles perturbed using only scaling factors (in this case the shape of the initial guess was consistent with the shape of the 'true' profiles). We named 'CS' this test (CS = Correct Shape). The CS test showed that this 'shape error' affects significantly the BT2 retrievals in the following cases:

1. Pressure at high altitudes (only marginally at low altitudes)
2. Temperature at high altitudes,
3. Water below the hygropause,
4. NO_2 at high altitudes

The CS test shows also that the 'shape error' does not affect ozone and nitric acid that are the remaining two cases with relatively large discrepancies between 'true' and retrieved profiles. Comparison between results of BT1 and BT2 tests shows that at low altitudes, tangent pressure error (that is 9%) has a significant impact on both ozone and nitric acid retrievals at the same altitudes. Most likely this large error in the retrieved pressure at low tangent altitudes in BT2 is due to the large correlation existing between atmospheric continuum and tangent pressure at these altitudes. The discrepancy observed in the retrieval of nitric acid at high altitude in the BT1 test is the only case for which there is a relatively weak explanation: at this altitude the amount of HNO_3 is very little and the retrieval provides very unstable values for both VMR and its noise error. We think therefore that the discrepancy observed at high altitudes in the HNO_3 BT1 retrieval is smaller than that observed in the BT2 case only because of a different number of iterations that took place in the two tests. Methane and N_2O retrievals had no problems in all the analyzed test cases.

Based on the results of blind test retrievals the following conclusions can be drawn:

1. In general the IROE2 code provides stable results also in presence of systematic errors in the forward model. In particular, the following systematic error sources are active in our test retrievals:
   - VMR profiles of contaminants assumed in the IROE2 code are different (within the limits of the atmospheric variability) compared to the profiles assumed by IAA for the generation of simulated observations,
   - IROE2 operates in LTE conditions while observations are simulated including NLTE
   - IROE2 neglects line-mixing while simulated observations include line-mixing,
   - IROE2 neglects pressure shift and self-broadening while simulated observations do include these effects,
   - 'shape error', as explained above.
2. The error estimates supplied by the Oxford tool (MWMAKE) and the covariance of the retrieval are in general consistent with the discrepancies between retrieved and reference (true) profiles with a good confidence level. The only discrepancies not fully consistent with the error predictions were found in the cases in which a) the 'shape error' (presently neglected in MWMAKE, but will be included in a future version) is significant and b) the tangent pressure error exceeds its expected value (3%).
3. Neglecting pressure-shift and self-broadening does not impact the accuracy of the retrieved profiles in the considered test cases. Therefore there is no clear indication suggesting that these two effects can not be neglected in MIPAS retrievals.
4. The loss of accuracy due to neglecting NLTE and Line-Mixing can be adequately controlled using an appropriate selection microwindows for the retrieval. Therefore, again, there is no clear indication suggesting that simulation of NLTE and Line-Mixing is compulsory for the retrieval of MIPAS key species at the presently required accuracy level.

RAL (WP 4450): The initial iteration of the blind test cases revealed an artifact in the minimisation routines which lead to large oscillations in the target species. This has been corrected and the processor now produces realistic profiles.
In the current results values deviate somewhat from the true profile at the lowest altitudes, in particular for H_2O. This is likely do be alleviated at least in part by using finer atmospheric level spacing in the forward model but work is also ongoing to focus the microwindow selection to the lower altitudes. Some generic improvements in efficiency are also in progress.

Discrepancies Processor IROE-R (WP 4500)

On the basis of the conclusions of the BT retrievals (WP 4440), it was decided not to improve the IROE2 code by including the simulation of presently neglected effects, but rather to upgrade the retrieval code (the upgraded retrieval code being referred as IROE1) to include the capability of detecting in MIPAS spectra possible anomalies that may be due to residual effects for which a correction is operated in Level 1b processing (e.g. frequency and intensity calibration, ILS determination, instrumental offset). In particular, we introduced in the IROE1 retrieval code the possibility to optionally fit, simultaneously with the main target parameters (pressure, temperature or VMR), the following additional parameters:

1. frequency shift parameter (one parameter for each spectral band),
2. intensity scaling parameter (one parameter for each spectral band),

3. ILS broadening parameter (one parameter for each spectral band),

4. MW- and altitude- dependent instrumental offset.

The newly implemented functionalities were tested. In particular, in the cases of pressure, temperature and H_2O the feasibility of the joint retrieval of the main target parameters together with an instrument–related parameter was assessed and the accuracy of the retrieved instrumental parameters was characterized. The results of these tests are reported in the document D42 (deliverable of the present study). The conclusions can be summarized as follows:

1. Simultaneous fit of pressure, temperature or H_2O profiles and frequency shift parameters is feasible with the JUL01 microwindows (MWs). The error associated with the retrieved frequency shift parameter is of the order of 10^-4 cm^-1, therefore the precision is comparable with spectroscopic errors (that are sweep independent and transition dependent)

2. Fit of intensity scaling parameters. There is a strong correlation between intensity calibration and temperature. An error of about 5calibration parameters determines a offset of about 2 K in the retrieved temperature profile. Therefore it is not possible to determine the absolute values of the intensity calibration parameters, but in case that MWs belonging to different bands are used in the retrieval, the ratio between the intensity calibration parameters of different bands can be determined.

3. The simultaneous fit of pT or H_2O profiles and the ILS broadening parameters is feasible. We found however that in order to attain good quality retrievals, stringent convergence criteria must be adopted.

4. Fit of MW- and altitude- dependent instrumental offset. The retrieval is able to recover the reference altitude-dependent zero-level calibration within its retrieval error (ESD). However for some of the MWs of the JUL01 set the sensitivity to instrumental offset parameters is relatively poor and for these MWs the estimated standard deviation of the retrieved instrumental offset exceeds the measurement noise.

Standardization of Retrieval Errors (WP 4600)

Introduction: A retrieved profile $\hat{\mathbf{x}}$ can generally be represented as some smoothing of the 'true' profile $\mathbf{x}$ plus error terms:

$$\hat{\mathbf{x}} = \mathbf{A}_x\mathbf{x} + (\mathbf{I} - \mathbf{A}_x)\mathbf{x}_a + \mathbf{G}(\delta\mathbf{y} - \delta\mathbf{f}) \tag{1.7}$$

where $\mathbf{A}_x = \partial\hat{\mathbf{x}}/\partial\mathbf{x}$ is the *Averaging Kernel Matrix* for the retrieval grid, $\mathbf{x}_a$ is any *a priori* constraint (which may be zero), $\mathbf{G} = \partial\hat{\mathbf{x}}/\partial\mathbf{y}$ is the *Gain Matrix* representing the mapping of the measurements $\mathbf{y}$ into the retrieval, $\delta\mathbf{y}$ is the vector representing the error in each measurement, $\delta\mathbf{f}$ is the vector representing the error in each corresponding forward model calculation.
Rearranging this gives the difference between the retrieval and the 'true' profile $\mathbf{x}$:

$$\hat{\mathbf{x}} - \mathbf{x} = (\mathbf{A}_x - \mathbf{I})(\mathbf{x} - \mathbf{x}_a) + \mathbf{G}(\delta\mathbf{y} - \delta\mathbf{f}) \tag{1.8}$$

It is convenient to define $\delta\mathbf{y}$ to contain just the random noise component of measurement error, while including correlated or persistent effects such as calibration errors in $\delta\mathbf{f}$ along with the forward model errors. The random noise is routinely propagated through each retrieval and the covariance of $\mathbf{G}\delta\mathbf{y}$ gives the random errors reported with each profile (see under the individual retrieval descriptions).
In this analysis we examine the other terms in the above equations required for a full characterisation of a retrieval: the averaging kernel ($\mathbf{A}_x$) and the systematic error contribution ($\mathbf{G}\delta\mathbf{f}$). Finally, 'REC' analysis is used to attempt to identify the spectral signatures of various components of $\delta\mathbf{f}$ in the retrieval residuals.

Averaging Kernels: The averaging kernel for the retrieval grid can be calculated from the gain matrix (dependent on the retrieval scheme) and the Jacobian matrix $\mathbf{K}_x = \partial \mathbf{y}/\partial \mathbf{x}$,

$$\mathbf{A}_x = \mathbf{G}\mathbf{K}_x \tag{1.9}$$

For an unconstrained least squares fit,

$$\mathbf{G} = \left(\mathbf{K}^T\mathbf{S}_y^{-1}\mathbf{K}\right)^{-1}\mathbf{K}^T\mathbf{S}_y^{-1} \tag{1.10}$$

where $\mathbf{S}_y$ is the covariance of the measurement noise $\delta\mathbf{y}$. Therefore, in this idealised case, $\mathbf{A}_x$ is the identity matrix. In practice such a retrieval usually results in profiles with unacceptably large oscillations so it is necessary to introduce some additional smoothness constraint, either directly by 'regularisation' or indirectly through the introduction of *a priori* information. This has the effect of trading vertical resolution for improved precision, effectively averaging the vertical information in the profile.
However, even if $\mathbf{A}_\mathbf{x} = \mathbf{I}$, the real atmospheric profile always contains structure at finer vertical resolution than the discrete levels represented by $\mathbf{x}$. We can represent this by defining a *high resolution* averaging kernel $\mathbf{A}_z$ (no longer a square matrix) representing the mapping of some detailed representation of the 'true' profile $\mathbf{z}$ into the retrieval on a coarser grid

$$\begin{aligned}\hat{\mathbf{x}} &= \mathbf{A}_z\mathbf{z} \\ &= \mathbf{A}_x\mathbf{L}\mathbf{z}\end{aligned} \tag{1.11}$$

where $\mathbf{L} = \partial\mathbf{x}/\partial\mathbf{z}$ is some type of averaging operator converting the high resolution profile $\mathbf{z}$ to the retrieval grid $\mathbf{x}$.
For these purposes, the high resolution profile will be defined as 1 km resolution, matching the 'true' input profiles for the blind test calculations. The high resolution averaging kernel $\mathbf{A}_z$ then represents the mapping of the true profile into the profile that should be retrieved given a perfect forward model and perfect (noiseless) measurements.
There are three methods for calculating these high resolution averaging kernels:

1. Numerical simulations: perturbing a 1 km level of an input profile, calculating the resulting measurements, passing these through the retrieval code and differencing the results compared to the results of an unperturbed profile. This yields a single column of $\mathbf{A}_z$.

2. Calculating high-resolution Jacobians $\mathbf{K}_z = \partial\mathbf{y}/\partial\mathbf{z}$

$$\mathbf{A}_z = \mathbf{G}\mathbf{K}_z \tag{1.12}$$

3. Using an estimate of $\mathbf{L}$ (combined with the readily available $\mathbf{A}_x$), which is not as simple an averaging process as it might seem. The retrieval forward model often uses an internal high resolution profile constructed by interpolating the retrieved profile,

$$\hat{\mathbf{z}} = \mathbf{H}\hat{\mathbf{x}} \tag{1.13}$$

where $\mathbf{H} = \partial\hat{\mathbf{z}}/\partial\hat{\mathbf{x}}$ is a model-specific interpolation (e.g., linear in VMR with altitude). The averaging of the true profile $\mathbf{z}$ to the retrieval grid can be thought of as the inverse of this process. Since $\mathbf{H}$ is not square there is not a unique solution, however if we assume that $\mathbf{A}_x \simeq \mathbf{I}$, the retrieval will converge to a profile $\hat{\mathbf{x}}$ which, when interpolated by $\mathbf{H}$, most closely matches the true profile $\mathbf{z}$. Minimising $(\mathbf{z} - \mathbf{H}\hat{\mathbf{x}})^2$ gives the standard least squares solution for $\mathbf{L}$

$$\mathbf{L} = \left(\mathbf{H}^T\mathbf{H}\right)^{-1}\mathbf{H}^T \tag{1.14}$$

Using one of the three methods outlined, each group has provided an estimate of the high resolution (1 km) averaging kernel for each retrieval.

Systematic Errors: Systematic errors are those errors which are correlated between measurements or forward model calculations (excluding the local correlations introduced by apodising the random noise). In general, these errors will also be correlated between one profile and the next according to various time/spatial scales.
Such errors are usually difficult to characterise, but some estimates have been made as input to various microwindow selection schemes. We can also use such a scheme to analyse the errors expected from the set of microwindows used in each blind test retrieval.
The following errors have been considered, calculated for mid-latitude day-time conditions:

- Calibration errors

  GAIN uncertainty in radiometric gain calibration (± 1 %)

  ILS uncertainty in instrument line shape calibration

  SHIFT uncertainty in spectral calibration (± 1 cm^{-1})

- Forward model parameter errors

  [**gas**] climatological 1-σ variabilities of 28 species

  CTMERR uncertainty in modelling gaseous (mostly H_2O) continua (± 25 %)

  HITRAN estimated uncertainties in HITRAN line parameters (molecule/band specific)

  TEM effect of propagation of temperature retrieval errors ($\pm$ 1 K)

  PRE effect of propagation of pressure retrieval errors ($\pm$ 2 %)

- Forward model errors

  NONLTE effect of assuming local thermodynamic equilibrium applies at all altitudes

  CO2MIX effect of ignoring CO_2 line-mixing effects

  GRA effect of assuming horizontally homogeneous atmosphere in line-of-sight direction ($\pm$ 1 K/100 km temperature gradient)

Note that for the blind test simulations, there were no calibration errors and no horizontal gradients. Discrepancies in the HITRAN and gaseous continuum parameters between the simulations and the various retrieval forward models are also probably much smaller than represented by the above. For the BT1 retrievals, there were no temperature or pressure errors.
Various error components of $\delta\mathbf{f}$ are extracted from the appropriate subsets of the error spectra associated with the microwindows used for each retrieval. However, rather than attempt to simulate the contribution function matrices $\mathbf{G}$ characteristic of each group's retrieval, we have assumed a single retrieval model (optimal estimation, with loose *a priori* constraints) which differs only in the number of retrieval levels. Effectively this assumes that all retrieval schemes weight the measurements according to measurement noise in a similar fashion (i.e., inversely proportional to the noise covariance), so that the propagation of systematic errors does not depend too much on the details of the retrieval scheme.

Residual and Error Correlation (REC) Analysis: The REC analysis involves fitting the pre–calculated spectral error signatures to retrieval residuals, in order to assess whether any systematic error sources contribute more than expected to the residuals.
If the residuals $\mathbf{r}$ are a combination of the different systematic error components $\delta\mathbf{f_i}$, each multiplied by a coefficient c_i:

$$\mathbf{r} = \sum_i \delta\mathbf{f_i} c_i = \mathbf{K_c c}$$

the error coefficients $\mathbf{c}$ can be obtained using:

$$\mathbf{c} = \mathbf{c_a} + \mathbf{G}(\mathbf{r} - \mathbf{K_c}\mathbf{c_a})$$

where $\mathbf{G}$ is the optimal estimation gain matrix and $\mathbf{c_a}$ is a vector containing the *a priori* values of the error coefficients for each source.
Each error spectrum $\delta\mathbf{f_i}$ is the effect of a 1σ uncertainty, so each error source is given an *a priori* value of 0 and an *a priori* uncertainty of 1.
The following parameters are calculated for each error source:

- an error coefficient, expected to be between -1 and 1 if error assumptions are correct. Values far outside this range indicate a problem. Error sources for which there are known to be deficiencies in the forward model (e.g. **NONLTE**, **CO2MIX**) are expected to show an error coefficient of 1.

- the fit uncertainty (*a priori* uncertainty is 1, so a value smaller than 1 indicates that there is information about this error source in the microwindows used).

GAIN, **SHIFT** and **ILS** errors are assessed at each altitude for each microwindow, while the other error sources are assigned one error coefficient for all altitudes and microwindows.

1.3.4 MIPAS Data Analysis (WP 5000)

This workpackage had to be postponed due to major delay of the launch of Envisat. However, some hurdles on the course towards MIPAS data analysis already have been passed: Envisat has successfully been launched into its orbit. Furthermore now all participating groups' CalVal Announcement of Opportunity proposals have been accepted by ESA, such that data access in the commissioning phase of Envisat is guaranteed.

Bibliography

[1] A. R. Curtis, "A statistical model for water–vapour absorption," *Q. J. R. Meteorol. Soc.* **78**, pp. 638–640, 1952.

[2] W. L. Godson, "The evaluation of infra–red radiative fluxes due to atmospheric water vapour," *Q. J. R. Meteorol. Soc.* **79**, pp. 367–379, 1953.

[3] W. L. Godson, "The computation of infrared transmission by atmospheric water vapour," *J. Meteorol.* **12**, pp. 272–284, 1955.

[4] A. R. Curtis, "The computation of radiative heating rates in the atmosphere," *Proc. R. Soc. London, Ser. A* **236**, pp. 156–159, 1956.

[5] T. von Clarmann et al., "AMIL2DA First Annual Report," tech. rep., 2001. EC Contract EVG1-CT-1999-00015.

[6] J. M. Flaud, "Complementary spectroscopic data," tech. rep., 2001. EC Contract EVG1-CT-1999-00015.

[7] G. P. Stiller, ed., *The Karlsruhe Optimized and Precise Radiative Transfer Algorithm (KOPRA)*, vol. FZKA 6487 of *Wissenschaftliche Berichte*, Forschungszentrum Karlsruhe, 2000.

[8] F. Hase and M. Höpfner, "Atmospheric ray path modeling for radiative transfer algorithms," *Appl. Opt.* **38**(15), pp. 3129–3133, 1999.

[9] M. Kuntz, "A new implementation of the Humlicek algorithm for the calculation of the Voigt profile function," *J. Quant. Spectrosc. Radiat. Transfer* **57**(6), pp. 819–824, 1997.

[10] J. Humlicek, "Optimized computation of the Voigt and complex probability functions," *J. Quant. Spectrosc. Radiat. Transfer* **27**(4), pp. 437–444, 1982.

[11] B. Funke, G. P. Stiller, T. von Clarmann, G. Echle, and H. Fischer, "CO_2 line mixing in MIPAS limb emission spectra and its influence on retrieval of atmospheric parameters," *J. Quant. Spectrosc. Radiat. Transfer* **59**(3–5), pp. 215–230, 1998.

[12] P. Rosenkranz, "Pressure broadening of rotational bands. I. A statistical theory," *J. Chem. Phys.* **83**(12), pp. 6139–6144, 1985.

[13] S. A. Clough, F. X. Kneizys, and R. W. Davies, "Line shape and the water vapor continuum," *Atmospheric Research* **23**, pp. 229–241, 1989.

[14] B. Carli, M. Ridolfi, P. Raspollini, B. M. Dinelli, A. Dudhia, and G. Echle, "Study of the retrieval of atmospheric trace gas profiles from infrared spectra," tech. rep., European Space Agency, 1998. Final Report of ESA Contract 12055/96/NL/CN.

[15] M. Höpfner, H. Oelhaf, G. Wetzel, F. Friedl-Vallon, A. Kleinert, A. Lengel, G. Maucher, H. Nordmeyer, N. Glatthor, G. P. Stiller, T. von Clarmann, H. Fischer, C. Kröger, and T. Deshler, "Evidence of scattering of tropospheric radiation by PSCs in mid-IR limb emission

spectra: MIPAS-B observations and KOPRA simulations." Geophys. Res. Lett., accepted for publication, 2002.

[16] M. Kuntz and M. Höpfner, "Efficient line–by–line calculation of absorption coefficients," *J. Quant. Spectrosc. Radiat. Transfer* **63**(1), pp. 97–114, 1999.

[17] A. Levenberg, "A method for the solution of certain non–linear problems in least squares," *Quart. Appl. Math.* **2**, pp. 164–168, 1944.

[18] D. W. Marquardt, "An algorithm for least–squares estimation of nonlinear parameters," *J. Soc. Indust. Appl. Math.* **11**(2), pp. 431–441, 1963.

[19] W. H. Press, S. A. Teukolsky, W. T. Vetterling, and B. P. Flannery, *Numerical Recipes in FORTRAN 90*, Cambridge University Press, Cambridge, zweite ed., 1996.

[20] T. B. McKee, R. I. Whitman, and J. J. Lambiotte, Jr., "A technique to infer atmospheric water–vapor mixing ratio from measured horizon radiance profiles," Tech. Rep. TN D–5252, NASA, Washington, D.C., 1969.

[21] A. Goldman and R. S. Saunders, "Analysis of atmospheric infrared spectra for altitude distribution of atmospheric trace constituents – I. Method of analysis," *J. Quant. Spectrosc. Radiat. Transfer* **21**, pp. 155–161, 1979.

[22] J. M. Russell III and S. R. Drayson, "The inference of atmospheric ozone using satellite horizon measurements in the 1042 cm^{-1} band," *J. Atmos. Sci.* **29**, pp. 376–390, 1972.

[23] M. Carlotti, "Global–fit approach to the analysis of limb–scanning atmospheric measurements," *Appl. Opt.* **27**(15), pp. 3250–3254, 1988.

[24] D. P. Edwards, "GENLN2: A general line–by–line atmospheric transmittance and radiance model," tech. rep., NCAR, Boulder, Colorado, 1992. Version 3.0, Description and users guide, NCAR/TN–367+STR.

[25] S. A. Clough, F. X. Kneizys, E. P. Shettle, and G. P. Anderson, "Atmospheric radiance and transmittance: FASCOD2," in *Proceedings of the Sixth Conference on Atmospheric Radiation*, pp. 141–146, Am. Meteorol. Soc., Williamsburg, Va., May 1986.

[26] L. S. Rothman, C. P. Rinsland, A. Goldman, T. Massie, D. P. Edwards, J.-M. Flaud, A. Perrin, C. Camy-Peyret, V. Dana, J.-Y. Mandin, J. Schroeder, A. McCann, R. R. Gamache, R. B. Wattson, K. Yoshino, K. V. Chance, K. W. Jucks, L. R. Brown, V. Nemtchinov, and P. Varanasi, "The HITRAN molecular spectroscopic database and HAWKS (HITRAN atmospheric workstation): 1996 edition," *J. Quant. Spectrosc. Radiat. Transfer* **60**(5), pp. 665–710, 1998.

[27] L. L. Strow, H. E. Motteler, R. G. Benson, S. E. Hannon, and S. De Souza-Machado, "Fast computation of monochromatic infrared atmospheric transmittances using compressed look-up tables," *J. Quant. Spectrosc. Radiat. Transfer* **59**(3-5), pp. 481–493, 1998.

[28] R. J. Wells, "Rapid approximation to the Voigt/Faddeeva function and its derivatives," *J. Quant. Spectrosc. Radiat. Transfer* **62**(1), pp. 29–48, 1999.

[29] F. Schreier and B. Schimpf, "A new efficient line-by-line code for high resolution atmospheric radiation computations incl. derivatives," in *IRS 2000: Current Problems in Atmospheric Radiation*, W. L. Smith and Y. Timofeyev, eds., pp. 381–384, A. Deepak Publishing, Hampton, Va, USA, 2001.

[30] B. Schimpf and F. Schreier, "Robust and efficient inversion of vertical sounding atmospheric high-resolution spectra by means of regularization," *J. Geophys. Res.* **102**(D13), pp. 16,037–16,055, 1997.

[31] A. K. Hui, B. H. Armstrong, and A. A. Wray, "Rapid computation of the Voigt and complex error functions," *J. Quant. Spectrosc. Radiat. Transfer* **19**, pp. 509–516, 1978.

[32] F. Schreier, "The Voigt and complex error function: A comparison of computational methods," *J. Quant. Spectrosc. Radiat. Transfer* **48**(5/6), pp. 743–762, 1992.

[33] L. S. Rothman, R. B. Wattson, R. R. Gamache, J. Schroeder, and A. McCann, "HITRAN HAWKS and HITEMP high temperature molecular database," *Proc. SPIE* **2471**, pp. 105–111, 1995.

[34] K. V. Chance, K. W. Jucks, D. G. Johnson, and W. A. Traub, "The Smithsonian Astrophysical Observatory database 1992," *J. Quant. Spectrosc. Radiat. Transfer* **52**, pp. 447–457, 1994.

[35] N. Jacquinet-Husson, E. Arié, J. Ballard, A. Barbe, G. Bjoraker, B. Bonnet, L. R. Brown, C. Camy-Peyret, J. P. Champion, A. Chédin, A. Chursin, C. Clerbaux, G. Duxbury, J.-M. Flaud, N. Fourrié, A. Fayt, G. Graner, R. Gamache, A. Goldman, V. Golovko, G. Guelachvili, J. M. Hartmann, J. C. Hilico, J. Hillman, G. Lefèvre, E. Lellouch, S. N. Mikhaïlenko, O. V. Naumenko, V. Nemtchinov, D. A. Newnham, A. Nikitin, J. Orphal, A. Perrin, D. C. Reuter, C. P. Rinsland, L. Rosenmann, L. S. Rothman, N. A. Scott, J. Selby, L. N. Sinitsa, J. M. Sirota, A. M. Smith, K. M. Smith, V. G. Tyuterev, R. H. Tipping, S. Urban, P. Varanasi, and M. Weber, "The 1997 spectroscopic GEISA databank," *J. Quant. Spectrosc. Radiat. Transfer* **62**(2), pp. 205–254, 1999.

[36] H. M. Pickett, R. L. Poynter, E. A. Cohen, M. L. Delitsky, J. C. Pearson, and H. S. P. Müller, "Submillimeter, millimeter, and microwave spectral line catalog," *J. Quant. Spectrosc. Radiat. Transfer* **60**(5), pp. 883–890, 1998.

[37] R. H. Norton and C. P. Rinsland, "ATMOS data processing and science analysis methods," *Appl. Opt.* **30**(4), pp. 389–400, 1991.

[38] H. J. Liebe, G. A. Hufford, and M. G. Cotton, "Propagation modeling of moist air and suspended water/ice particles at frequencies below 1000 GHz," in *52nd Specialists Meeting of the Electromagnetic Wave Propagation Panel*, AGARD, May 1993.

[39] D. Kahaner, C. Moler, and S. Nash, *Numerical Methods and Software*, Prentice–Hall, Englewood Cliffs, NJ, 1989.

[40] P. Deuflhard, H. W. Engl, and O. Scherzer, "A convergence analysis of iterative methods for the solution of nonlinear ill–posed problems under affinely invariant conditions," *Inverse Problems* **14**, pp. 1081–1106, 1998.

[41] M. Hanke, "A regularizing Levenberg–Marquardt scheme, with applications to inverse groundwater filtration problems," *Inverse Problems* **13**, pp. 79–95, 1997.

[42] U. Tautenhahn, "On a general regularization scheme for nonlinear ill–posed problems," *Inverse Problems* **13**, pp. 1427–1437, 1997.

[43] M. Ridolfi, B. Carli, M. Carlotti, T. von Clarmann, B. Dinelli, A. Dudhia, J.-M. Flaud, M. Höpfner, P. E. Morris, P. Raspollini, G. Stiller, and R. J. Wells, "Optimized forward and retrieval scheme for MIPAS near-real-time data processing," *Appl. Opt.* **39**(8), pp. 1323–1340, 2000.

[44] "Military Standard 2401." Department of Defense World Geodetic System (WGS), 1994.

[45] H. Norton and R. Beer, "New apodizing functions for Fourier spectrometry," *J. Opt. Soc. Am* **66**(3), pp. 259–264, 1976. (Errata J. Opt. Soc. Am., 67, 419,1977).

[46] E. G. Gill, W. Murray, and M. H. Wright, *Practical Optimization*, Academic Press, Inc., New York, 1981.

[47] J.-M. Hartmann, C. Boulet, M. Margottin-Maclou, F. Rachet, B. Khalil, F. Thibault, and J. Boissoles, "Simple modelling of Q-branch absorption – I. Theoretical model and application to CO_2 and N_2O," *J. Quant. Spectrosc. Radiat. Transfer* **54**(4), pp. 705–722, 1995.

[48] A. Dudhia, "A multi-layer technique for microwindow selection PO-TN-OXF-GS-0013," tech. rep., Oxford University, 1999. Deliverable of ESA Contract 11886/96/NL/GS.

[49] W. J. Reburn, R. Siddans, B. J. Kerridge, S. Buehler, A. von Engeln, P. Eriksson, T. Kuhn-Sander, K. Kuenzi, and C. Verdes, "Critical assessments in millimetre-wave atmospheric limb sounding." Final Report, ESA Contract NO.: 13348/98/NL/GD, Part V.

[50] M.-R. De Backer-Barilly and A. Barbe, "Absolute intensities of the 10–μm bands of $^{16}O_3$," *J. Mol. Spectrosc.* **205**(1), pp. 43–53, 2001.

[51] C. Claveau, C. Camy-Peyret, A. Valentin, and J.-M. Flaud, "Absolute intensities of the ν_1 and ν_3 bands of $^{16}O_3$," *J. Mol. Spectrosc.* **206**(2), pp. 115–125, 2001.

[52] T. Wagner, C. Leue, K. Pfeilsticker, and U. Platt, "Monitoring of the stratospheric chlorine activation by Global Ozone Monitoring Experiment (GOME) OClO measurements in the austral and boreal winters 1995 through 1999," *J. Geophys. Res.* **106**(D5), pp. 4971–4986, 2001.

[53] M. A. H. Smith, V. Malathy Devi, D. C. Benner, and C. P. Rinsland, "Absolute intensities of $^{16}O_3$ lines in the 9-11 μm region," *J. Geophys. Res.* **106**(D9), pp. 9909–9921, 2001.

[54] J.-M. Flaud, M. Birk, G. Wagner, J. Orphal, S. Klee, and W. J. Lafferty, "The far infrared spectrum of HOCl: Line positions and intensities," *J. Mol. Spectrosc.* **191**(2), pp. 362–367, 1998.

[55] J. Vander Auwera, J. Kleffmann, J.-M. Flaud, G. Pawelke, H. Bürger, D. Hurtmans, and R. Pétrisse, "Absolute ν_2 line intensities of HOCl by simultaneous measurements in the infrared with a tunable diode laser and far–infrared region using a Fourier transform spectrometer," *J. Mol. Spectrosc.* **204**(1), pp. 36–47, 2000.

[56] A. Perrin, J.-M. Flaud, C. Camy-Peyret, A. M. Vasserot, G. Guelachvili, A. Goldman, F. J. Murcray, and R. D. Blatherwick, "The ν_1, $2\nu_2$ and ν_3 interacting bands of NO_2: line positions and intensities," *J. Mol. Spectrosc.* **154**, pp. 391–406, 1992.

[57] C. Camy-Peyret, J. Flaud, and A. Perrin, "Improved line parameters for the ν_3 and the $\nu_2 + \nu_3 - \nu_2$ bands of NO_2," *J. Mol. Spectrosc.* **95**, pp. 72–79, 1982.

[58] A. Perrin, J.-M. Flaud, C. Camy-Peyret, D. Hurtmans, and G. Guelachvili, "The $\nu_2 + \nu_3$ and $\nu_2 + \nu_3 - \nu_2$ bands of NO_2: line positions and intensities," *J. Mol. Spectrosc.* **168**, pp. 54–66, 1994.

[59] J. Y. Mandin, V. Dana, A. Perrin, J. Flaud, C. Camy-Peyret, L. Régalia, and A. Barbe, "The $\nu_1 + 2\nu_2, \nu_1 + 2\nu_3$ bands of NO_2: line positions and intensities, line intensities in the $\nu_1 + \nu_2 + \nu_3 - \nu_2$ hot band," *J. Mol. Spectrosc.* **181**, pp. 379–388, 1997.

[60] A. Perrin, J.-M. Flaud, C. Camy-Peyret, D. Hurtmans, and M. Herman, "The $2\nu_3$, $4\nu_3$, $2\nu_2$ + ν_3 and $2\nu_3$ - ν_3 bands of NO_2: line positions and intensities," *J. Mol. Spectrosc.* **177**, pp. 58–65, 1996.

[61] T. M. Stephen, A. Goldman, A. Perrin, J.-M. Flaud, F. Keller, and C. P. Rinsland, "New high–resolution analysis of the $3\nu_3$ and $2\nu_1$ + ν_3 bands of nitrogen dioxide (NO_2) by Fourier transform spectroscopy," *J. Mol. Spectrosc.* **201**(1), pp. 134–142, 2000.

[62] P. Varanasi and V. Nemtchinov, "Thermal infrared absorption coefficients of CFC–12 at atmospheric conditions," *J. Quant. Spectrosc. Radiat. Transfer* **51**(5), pp. 679–687, 1994.

[63] M. López-Puertas, G. Zaragoza, M. Á. López-Valverde, F. J. Martín-Torres, G. M. Shved, R. O. Manuilowa, A. A. Kutepov, O. Gusev, T. von Clarmann, A. Linden, G. Stiller, A. Wegner, H. Oelhaf, D. P. Edwards, and J.-M. Flaud, "Non–local thermodynamic equilibrium limb radiances for the MIPAS instrument on ENVISAT–1," *J. Quant. Spectrosc. Radiat. Transfer* **59**(3–5), pp. 377–403, 1998.

[64] T. von Clarmann et al., "Forward model intercomparison report," tech. rep., 2001. EC Contract EVG1-CT-1999-00015.

[65] M. López-Puertas and F. W. Taylor, *Non-LTE radiative transfer in the Atmosphere*, World Scientific Pub., Singapore, 2001.

[66] T. von Clarmann, A. Dudhia, G. Echle, J.-M. Flaud, C. Harrold, B. Kerridge, A. Koutoulaki, A. Linden, M. López-Puertas, M. Á. López-Valverde, F. J. Martín-Torres, J. Reburn, J. Remedios, C. D. Rodgers, R. Siddans, R. J. Wells, and G. Zaragoza, "Study on the simulation of atmospheric infrared spectra," tech. rep., European Space Agency, 1998. Final Report of ESA Contract 12054/96/NL/CN.

[67] J. J. Remedios, "Compilation of reference atmospheres for the MIPAS studies," 2001. (j.remedios1@physics.ox.ac.uk).

[68] J.-C. Gérard and R. G. Roble, "The role of nitric oxide on the zonally averaged structure of the thermosphere: solstice conditions for solar cycle maximum," *Planet. Space Sci.* **36**, pp. 271–279, 1988.

[69] R. R. Garcia and S. Solomon, "A new numerical model for the middle atmosphere 2. Ozone and related species," *J. Geophys. Res.* **99**, pp. 12937–12951, 1994.

[70] A. E. Hedin, "Extension of the MSIS thermosphere model into the middle and lower atmosphere," *J. Geophys. Res.* **96**(A2), pp. 1159–1172, 1991.

[71] R. R. Garcia, F. Stordal, S. Solomon, and J. T. Khiel, "A new numerical model for the middle atmosphere 1. Dynamics and transport of tropospheric source gases," *J. Geophys. Res.* **97**, pp. 12967–12991, 1992.

[72] M. López-Puertas, G. Zaragoza, M. Á. López-Valverde, and F. W. Taylor, "Non local thermodynamic equilibrium (LTE) atmospheric limb emission at 4.6 μm 1. An update of the CO_2 non–LTE radiative transfer model," *J. Geophys. Res.* **103**(D7), pp. 8499–8513, 1998.

[73] M. López-Puertas, G. Zaragoza, M. Á. López-Valverde, and F. W. Taylor, "Non local thermodynamic equilibrium (LTE) atmospheric limb emission at 4.6 μm 2. An analysis of the daytime wideband radiances as measured by UARS improved stratospheric and mesospheric sounder," *J. Geophys. Res.* **103**(D7), pp. 8515–8530, 1998.

[74] M. López-Puertas, M. Á. López-Valverde, R. R. Garcia, and R. G. Roble, "A review of CO_2 and CO abundances in the middle atmosphere," in *Atmospheric Science Across the Stratopause*, D. E. Siskind, S. D. Eckermann, and M. E. Summers, eds., vol. 123 of *Geophysical Monograph Series*, p. 83, American Geophysical Union, 2000.

[75] P. P. Wintersteiner, C. T. Mertens, and M. López-Puertas et al., "Comparison of CO_2 15, 4.3, and 2.7 μm models," 2002. J. Geophys. Res., in preparation.

[76] F. J. Martín-Torres and M. López-Puertas, "A non-LTE model for the O_3 vibrational levels in the middle atmosphere," 2002. J. Geophys. Res., in preparation.

[77] B. Funke and M. López-Puertas, "Nonlocal thermodynamic equilibrium vibrational, rotational, and spin state distribution of NO(ν= 0,1,2) under quiescent atmospheric conditions," *J. Geophys. Res.* **105**(D4), pp. 4409–4426, 2000.

[78] F. Hase, "Transformation of irradiated to measured spectral distribution due to finite spectral resolution and field of view extent of a Fourier transform spectrometer," in *The Karlsruhe Optimized and Precise Radiative transfer Algorithm (KOPRA)*, G. P. Stiller, ed., Wissenschaftliche Berichte FZKA 6487, pp. 119–132, Forschungszentrum Karlsruhe, 2000.

[79] C. Cousin, R. Le Doucen, C. Boulet, and A. Henry, "Temperature dependence of the absorption in the region beyond the 4.3–μm band head of CO_2. 2: N_2 and O_2 broadening," *Appl. Opt.* **24**(22), pp. 3899–3907, 1985.

[80] R. Le Doucen, C. Cousin, C. Boulet, and A. Henry, "Temperature dependence of the absorption in the region beyond the 4.3–μm band head of CO_2. 1: Pure CO_2 case," *Appl. Opt.* **24**(6), pp. 897–906, 1985.

[81] V. Menoux, R. Le Doucen, J. Boissoles, and C. Boulet, "Line shape in the low frequency wing of self– and N_2–broadened ν_3 CO_2 lines: temperature dependence of the asymmetry," *Appl. Opt.* **30**(3), pp. 281–286, 1991.

[82] L. L. Strow, D. C. Tobin, and S. E. Hannon, "A compilation of first–order line–mixing coefficients for CO_2 Q–branches," *J. Quant. Spectrosc. Radiat. Transfer* **52**(3/4), pp. 281–294, 1994.

[83] H. Fischer, G. P. Anderson, T. von Clarmann, S. A. Clough, M. T. Coffey, A. Goldman, and F. X. Kneizys, "Intercomparison of transmittance and radiance algorithms (ITRA), Report of the limb-group of the ITRA-workshop at the University of Maryland, 12–14 March 1986," Wissenschaftliche Berichte KfK 4349, Kernforschungszentrum Karlsruhe, 1988.

[84] T. von Clarmann, A. Dudhia, D. P. Edwards, B. Funke, M. Höpfner, B. Kerridge, V. Kostsov, A. Linden, M. López-Puertas, and Y. Timofeyev, "Intercomparison of non-local thermodynamic equilibrium forward radiance codes." submitted to J. Geophys. Res., 2001.

[85] T. Deshler, "In situ measurements of Pinatubo aerosol over Kiruna on four days between 18 January and 13 February 1992," *Geophys. Res. Lett.* **21**(13), pp. 1323–1326, 1994.

[86] R. T. Tisdale, D. L. Glandorf, M. A. Tolbert, and O. B. Toon, "Infrared optical constants of low–temperature H_2SO_4 solutions representative of stratospheric sulfate aerosols," *J. Geophys. Res.* **103**(D19), pp. 25,353–25,370, 1998.